LONG RANGE MATERIALS RESEARCH

Robert A. Huggins

Stanford University

Prepared for:

Defense Advanced Research Projects Agency

June 1975

CMR-75-13

SEMI-ANNUAL TECHNICAL REPORT

LONG RANGE MATERIALS RESEARCH

Sponsored by

Defense Advanced Research Projects Agency

ARPA Order No. 2470 -- Amendment F

June, 1975

The views and conclusions contained in this document are those of the authors and should not be interpreted as necessarily representing the official policies, either expressed or implied, of the Defense Advanced Research Projects Agency or the U. S. Government.

CENTER FOR MATERIALS RESEARCH

STANFORD UNIVERSITY • STANFORD, CALIFORNIA

198

SEMI-ANNUAL TECHNICAL REPORT

Long Range Materials Research

Sponsored by
Defense Advanced Research Projects Agency
ARPA Order No. 2470 - Amendment F

Program Code Number: 4D10

Contractor: Stanford University

Effective Date of Contract: June 1, 1974

Contract Expiration Date: May 31, 1975

Amount of Grant: $164,000

Grant Number: DAH C15 73 G15 Amendment No. 2

Principal Investigator: Robert A. Huggins
Phone: (415) 497-4118

Short Title: Long Range Materials Research

June, 1975

Center for Materials Research
Stanford University
Stanford, California 94305
(415) 497-4118

TABLE OF CONTENTS

I. GENERAL INTRODUCTION

This semi-annual technical report on the research program entitled "Long Range Materials Research," covers the time until June, 1975. This program is composed of four separate programs as follows:

1. Detection of X-Ray Radiation
2. Superplasticity and Warm Working of Metals and Alloys
3. Synthesis of New Types of Catalyst Materials
4. Development of Elevated Temperature Electrocrystallization Techniques.

Progress in each of the subareas during this report period will be described separately in the succeeding sections of this report.

II. DETECTION OF X-RADIATION

C. W. Bates, Jr.

Associate Professor of Materials Science
and Engineering
and Electrical Engineering

A. Introduction

The work in our laboratory is aimed at determining the physics of the luminescence phenomena associated with activated and unactivated alkali halide crystals which are used as particle detectors in high energy physics[1-9], x-ray sensors in astronomical observations[10] and in the medical field in x-ray image intensifiers used in diagnostic radiology[11]. Our work is currently concentrated on unraveling the luminescent mechanism in CsI(Na), at present the most efficient alkali-halide x-ray converter (x-ray photons to blue light photons). During this year we feel that we have made a significant breakthrough in determining certain aspects of this mechanism.

This report is divided into four sections which represent in addition to four problem areas, the contents of four papers submitted to journals this past year. Two of them have already been accepted for publication. They are the sections entitled "Optical Properties of CsI(Na) and Heat-Treated Pure CsI" (accepted for publication in Physics Letters A) and "Strain-Induced Room Temperature Photoluminescence in CsI and CsI(Na)" (Solid-State Communications). There is every reason to expect that the remaining two sections which have been submitted to the Journal of Luminescence will also be accepted for publication. Because this report is divided in this fashion each section is self-contained, i.e., they each have their own references and figures.

The final phase of this research effort which is presently underway consists in extending the optical studies to liquid helium temperatures, looking at the polarization properties of the various emissions on bulk single crystals, and investigating the magnetic properties of the various centers responsible for the emissions using the technique of electron paramagnetic resonance (EPR). Initial experiments using EPR and discussed briefly in the section on Luminescent Phenomena in CsI have shown that this technique should throw considerable light on the emission process in the systems we are investigating.

REFERENCES

1. R. Hofstadter, Phys. Rev. 74, 100 (1948); 75, 975 (1949).
2. H. Kallmann, Phys. Rev. 75, 623 (1949).
3. E. C. Farmer, H. B. Moore and C. Goodman, Phys. Rev. 76, 454 (1949).
4. C. E. Mandeville and H. O. Albrecht, Phys. Rev. 80, 299 (1950).
5. R. Hofstadter, J. A. McIntyre and H. I. West, Phys. Rev. 82, 749 (1951).
6. M. Furst and H. Kallmann, Phys. Rev. 82, 964 (1951).
7. J. Bonanomi and J. Rossel, Helv. Phys. Acta. 25, 725 (1952).
8. W. Van Sciver and R. Hofstadter, Phys. Rev. 87, 522 (1952).
9. B. Hahn and J. Rossel, Helv. Phys. Acta. 26, 271, 803 (1953).
10. F. S. Mozer, E. Bogott and C. W. Bates, Jr., IEEE Trans. on Nucl. Sci. NS-15, 144 (1968).
11. C. W. Bates, Jr., Adv. in Electronics and Electron Physics, 28A, 545 (1969).

B. Optical Properties of CsI(Na) and Heat-Treated Pure CsI

Information in the literature on the nature of luminescence centers in alkali halide crystals containing nonisomorphic alkali metal impurities is somewhat limited[1-8]. It has been assumed that in this case impurity cations can give rise to complex impurity defects that serve as centers for exciton localization[9]. In this connection investigators have compared the luminescent properties of CsI(Na) crystals with those of unactivated CsI crystals that have been deformed or quenched and CsI containing the divalent impurity cations Ca^{2+}, Sr^{2+}, Ba^{2+} and Mn^{2+} [9-14]. Their luminescent spectra are quite similar. All have large stokes shifts, with emission occuring between 415 and 430 nm and excitation possible in the 220-240 nm region.

It is generally agreed[6,7,12-14] that the blue luminescence of CsI crystals doped with divalent cations is due to annihilation of excitons near the cationic vacancies that compensate the excess charge of the dopant. Electron paramagnetic resonance studies of the Mn^{2+} ion in CsI crystals[15] also indicate that cation vacancy-divalent ion pairs isolated in the lattice rather than impurity aggregates on dislocations are responsible for the emission. Moreover, the chemical nature of the divalent impurity does not affect the luminescence. The blue luminescence of unactivated CsI crystals that have been deformed or quenched is currently attributed to centers associated with unidentified structural defects[16-20]. It is felt however that these defects are cation vacancies. For the above reasons it is commonly believed that the blue luminescences of unactivated CsI that has been deformed or quenched, CsI containing divalent impurities and CsI(Na) to be due to structural vacancy type cation sublattice defects. Because the

temperature dependence of the emission in the 415-430 nm range for CsI containing divalent impurities[14] is opposite to that of CsI(Na)[3] and the work performed on unactivated CsI crystals that had been deformed or quenched occurred during a period when the effects of trace quantities of sodium were not appreciated, a model describing the luminescence in these three systems as due to cation vacancies must be reexamined. In addition quenched CsI crystals normally give other emissions at 300 and 690 nm depending upon treatment[20]. It also has not been reported whether or not these emissions are superpositions of two or more emissions as has been found in the case of CsI(Tl)[21] such that other centers might be involved in the emission process.

To resolve these difficulties we have measured excitation and emission spectra of CsI(Na) crystals with .01-.04 mole percent sodium and heat-treated pure CsI at room and liquid nitrogen temperatures. Both pure and activated crystals were cut and polished to the same dimensions ($\frac{1}{2}$" x $\frac{1}{2}$" x 2mm) and were obtained from the Harshaw Chemical Company. The pure crystals were examined by emission spectroscopy for impurities. None were found by this technique. The heat treatment consisted essentially of heating the crystals slowly to 500°C in air, letting them remain there for 1 hour and then cooling to room temperature in about 4 hours. This work will be reported in detail at a later time[22]. The emission spectra of CsI(Na) crystals at room temperature consists of a single emission centered at 425 nm with a narrow excitation band located at 250 nm, i.e., on the long wavelength tail of the fundamental absorption. At liquid nitrogen temperature the 425 nm emission is most efficiently excited in the 235 nm

region. The emission spectra of the pure CsI is quite similar to that of CsI(Na). At room temperature it has a single emission centered at 430 nm with a narrow excitation band at 255 nm. At liquid nitrogen the 430 nm emission has its excitation peak at 240 nm. The results for emission are shown in figures 1 and 2. The photomultiplier tube voltages and amplifier sensitivities were approximately equal for the same measurement made on the pure CsI and CsI(Na) crystals. Except for a slight peak in the excitation curve at 230 nm for CsI(Na) at liquid nitrogen temperature which does not appear in the corresponding one for pure CsI, the spectra of the two materials are quite close. Since the pure CsI spectra are broader in general than those of CsI(Na) it is possible that this peak might be buried under the corresponding curve for pure CsI. Also the temperature dependences of the emission are in the same direction, i.e., both decrease as the temperature is lowered from room to liquid nitrogen temperature.

As our heat treatment is certainly not an annealing schedule (probably a mild or gentle quenching might be a suitable description) we feel that we have introduced vacancies into our crystal during this process and the emission is in some way associated with them. It should be noted that our treatment does not produce any additional emissions at 300 and 690 nm as in the work by Towyama[20]. In addition to these results, work in a preliminary stage[23] on deformed pure CsI crystals (4-20% deformation) and CsI(Na) crystals with an order of magnitude doping level of sodium less than the optimum of 0.01 mole percent essentially confirm the results of the heat treated crystals. The association of the introduction of sodium with structural defects probably of the vacancy type has now been put on a firmer foundation.

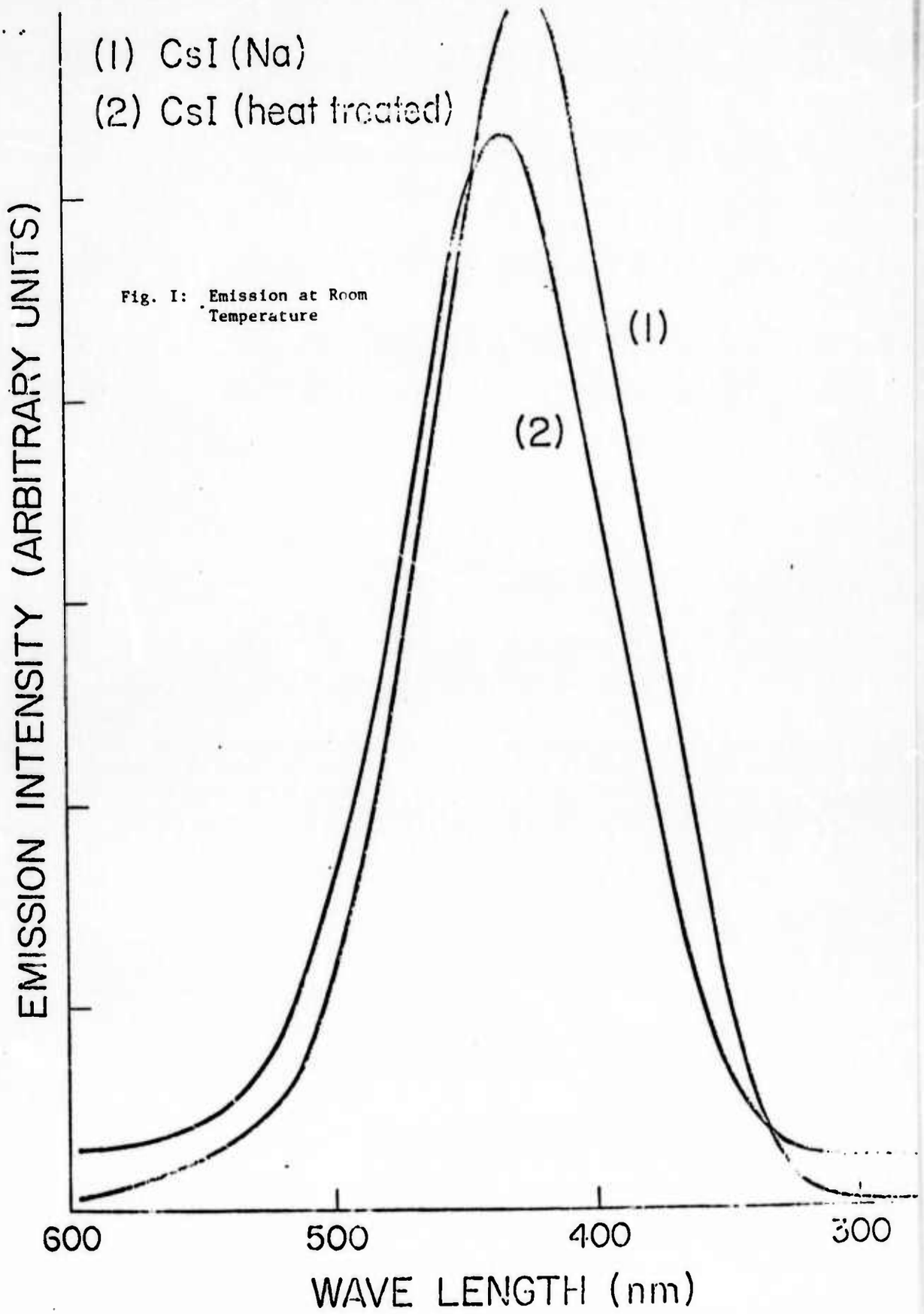

Fig. I: Emission at Room Temperature

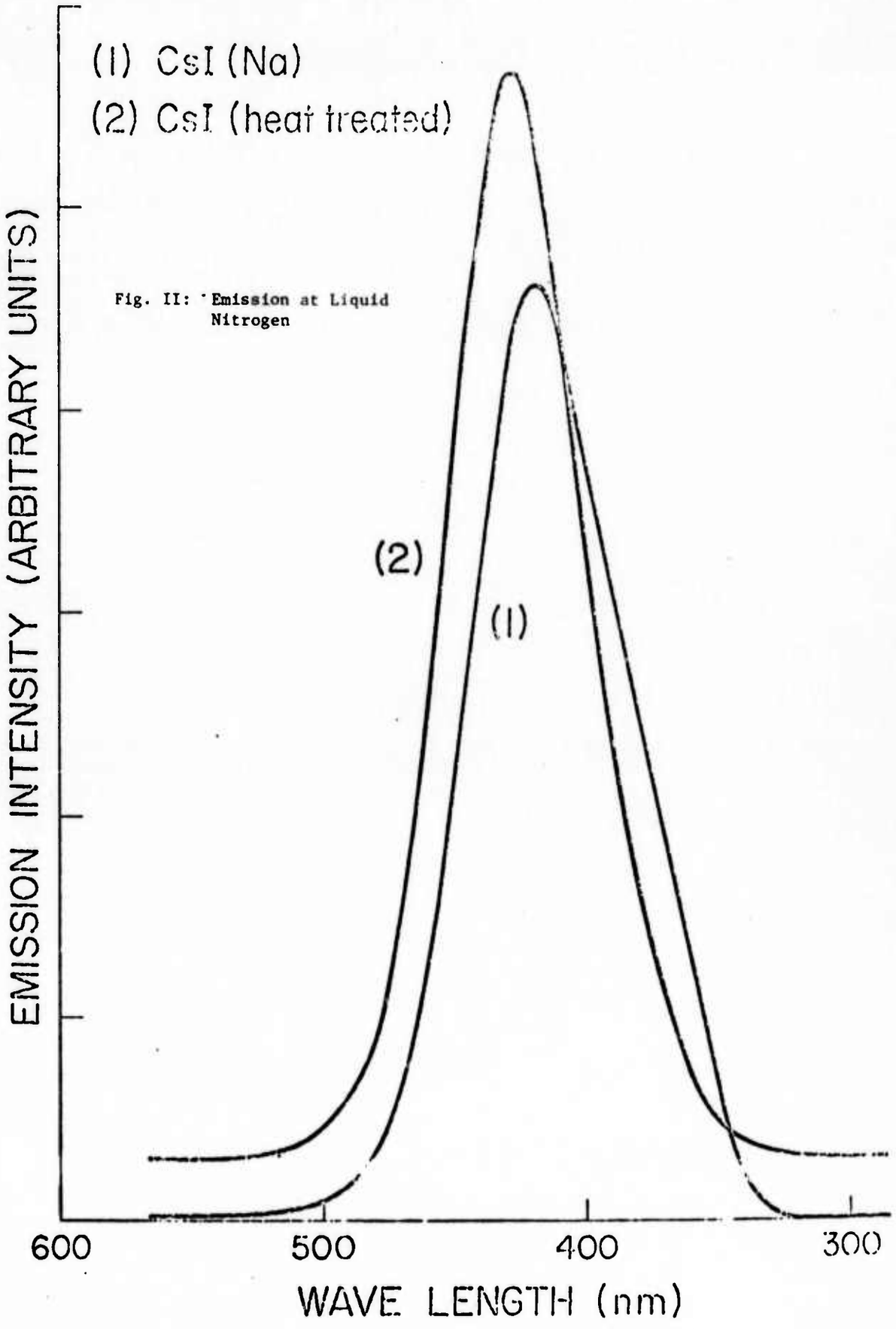

Fig. II: Emission at Liquid Nitrogen

1. References

1. P. Brinckman, Phys. Letters 15, 305 (1965).

2. C. W. Bates, Jr., Varian Associates Central Research Memorandum No. 200, June 1967.

3. J. Menefee, T. Cho and C. Swinehart, IEEE Trans. Nucl. Sci. 14, 464, 1967.

4. F. Mozer, F. Bogott, C. W. Bates, Jr., IEEE Trans. Nucl. Sci. 15, 144 (1968).

5. C. W. Bates, Jr., Adv. Electronics and Electron Physics 28A, 451 (1969).

6. A. Panova and N. Shiran, Opt. Spect. 32, 55 (1972).

7. A. Panova and N. Shiran, Opt. Spect. 32, 108 (1972).

8. C. W. Bates, Jr., Applied Optics 12, 938 (1973).

9. Y. A. Valbis, Opt. Spect. 21, 106 (1966).

10. D. Chauvy and J. Rossel, Helv. Phys. Acta 32, 481 (1959).

11. H. Besson, D. Chauvy and J. Rossel, Helv. Phys. Acta 35, 211 (1962).

12. M. Aegerter, E. Gucker, R. Heubi and J. Rossel, Int. Conf. on Scintillators (München, 1965), p. 292.

13. J. Rossel and M. Aegerter, J. Phys. 28, Suppl. 8-9, C4-140 (1967).

14. H. Lamatsch, J. Rossel and E. Saurer, Phys. Stat. Sol. 41, 605 (1970).

15. F. Porret, E. Saurer and J. Rossel, Helv. Phys. Acta 37, 632 (1964).

16. E. Morgenshtern, Optics and Spectroscopy 7, 231 (1959); ibid 8, 672 (1960).

17. N. Vasil'eva, Trans. Phys. Inst. of USSR Ac. of Sci. 39, 219 (1967).

18. S. Masunaga, J. Morita and M. Ishiguro, J. Phys. Soc. Japan 21, 638 (1966).

19. J. Bonanomie and J. Rossel, Helv. Phys. Acta 24, 310 (1951).

20. T. Towyama, Phys. Letters 31A, 206 (1970).

21. J. Donahue and K. Teegarden, J. Phys. Chem. Solids 29, 2141 (1968).

22. C. W. Bates, Jr. A. Salau, O. Hsu, "Absorption, Excitation and Emission Spectra of CsI and CsI(Na)", (in preparation).

23. C. W. Bates, Jr. and A. Salau; (unpublished results).

C. Strain-Induced Room Temperature Photoluminescence in CsI and CsI(Na)

1. Introduction

In a previous publication[1] henceforth referred to as I we showed that pure crystals of CsI which initially exhibited no emissions at room temperature, luminesced quite efficiently at room temperature after they had been subjected to a heat treatment which consisted essentially of heating slowly to 500°C and then cooling to room temperature in a period of three to four hours. This treatment produced a single emission centered at 430 nm with a narrow excitation band at 255 nm. These were compared with CsI(Na) crystals containing 0.01 mole percent sodium (which is the optimum amount for maximum luminescence efficiency[2]) which give an emission at 425 nm and an excitation peak at 255 nm. This work indicated that the effect of heat treating pure CsI crystals produces localized excitonic luminescence with yields which are comparable to those observed in untreated CsI(Na) crystals. To further corroborate this phenomenon we decided to perform the following experiments:

(1) Observe the emission from mechanically deformed crystals of pure CsI.

(2) Perform the same experiment as (1) on CsI(Na) where the sodium content is well below that for optimum luminescence efficiency (i.e., 1ppm).

(3) Repeat (2) for CsI(Na) where the sodium content is that for optimum luminescence efficiency (i.e., 6ppm).

This communication reports the results of these experiments.

2. Experimental Procedures and Results

All crystals were $\frac{1}{2}$" x $\frac{1}{2}$" x 2mm in size. The pure samples were analyzed to determine that the sodium content was much smaller than 1ppm (normally a few tenths ppm). These crystals as received normally exhibited no

emission at 420 nm when excited at 255 nm, on the long wavelength tail of the fundamental absorption. The crystals with 1ppm of sodium always showed a weak but well defined emission at about 420-430 nm when excited at 255 nm and a much weaker one at 460-470 nm for an excitation centered at 232 nm. The latter emission occurred in most but not all of the 1ppm samples and had an emission intensity which was independent of deformation. The origin of this latter emission is not known at this time and hence will not be discussed further. The CsI(Na) samples with an optimum sodium doping of 6ppm always exhibited an intense emission at 425 nm when excited by a narrow band centered at 250 nm. All crystals used in these experiments were obtained from the Harshaw Chemical Company of Cleveland, Ohio.

The crystals were mechanically deformed (compressed) on an Instron Mechanical Test Machine with deformation of 4% ($\frac{\Delta L}{L}$) being typical. The experimental arrangement for measuring emission and excitation spectra consisted of light from a deuterium light source, passing through a grating monochromator, mechanical chopper, and was incident on the broad ($\frac{1}{2}$" x $\frac{1}{2}$") crystal surface. The CsI samples were mounted in a dewar capable of cycling between liquid nitrogen and room temperatures. Emission was observed from the narrow edge of the crystal ($\frac{1}{2}$" x 2mm) at right angles to the incident radiation passing through a second grating monochromator, photomultiplier tube with an S-20 response and to a Lock-in-amplifier. Our results can be summarized as follows:

The nominally pure crystals of CsI which initially showed no detectable emission at any excitation wavelength showed an intense single emission centered at 425 nm after deformation with an excitation band centered at 255 nm. The samples of CsI(Na) containing 1ppm sodium which had a weak emission at 420-430 nm when excited at 255 nm, exhibited a single

very intense emission centered at 425 nm after deformation, the excitation peak shifting to 245 nm. The crystals of CsI(Na) with 6ppm sodium (optimum amount) showed a single intense emission at 425 nm with a single narrow excitation band centered at 250 nm whose intensity was the same both before and after the 4% deformation. The emission data for these crystals are shown in the Figure. For comparison purposes, the gain settings of the amplifier and photomultiplier tube were approximately the same for all samples during all emission measurements.

3. Discussion of Results

If as in I the heat treatment introduced structural defects which greatly enhanced the localized excitonic emission intensity one would expect that deforming the crystals would produce similar results and indeed this appears to be the case for pure CsI and CsI(Na) where the amount of sodium is below the amount necessary for optimum luminescence efficiency. From the Figure it is apparent that the increase in luminescence occurs where the sodium produces its maximum effect, i.e., at 425 nm. A most interesting and curious result of these experiments has been that CsI(Na) with an optimum concentration of sodium for emission shows no change in emission intensity as a result of the 4% deformation, apparently the result of the fact that 6ppm sodium introduced into the CsI lattice produces structural defects or other changes in an amount which can accommodate the 4% deformation without further affecting the luminescence.

At present these results are not clearly understood. The 425 nm emission strongly resembles the thermoluminescence produced at low temperatures and attributed to the migration of V_k centers followed by the radiative recombination with electrons trapped at sodium sites[3]. However, it is uncertain both why the intensity of the emission at room temperature decreases for Na^+ concentrations in

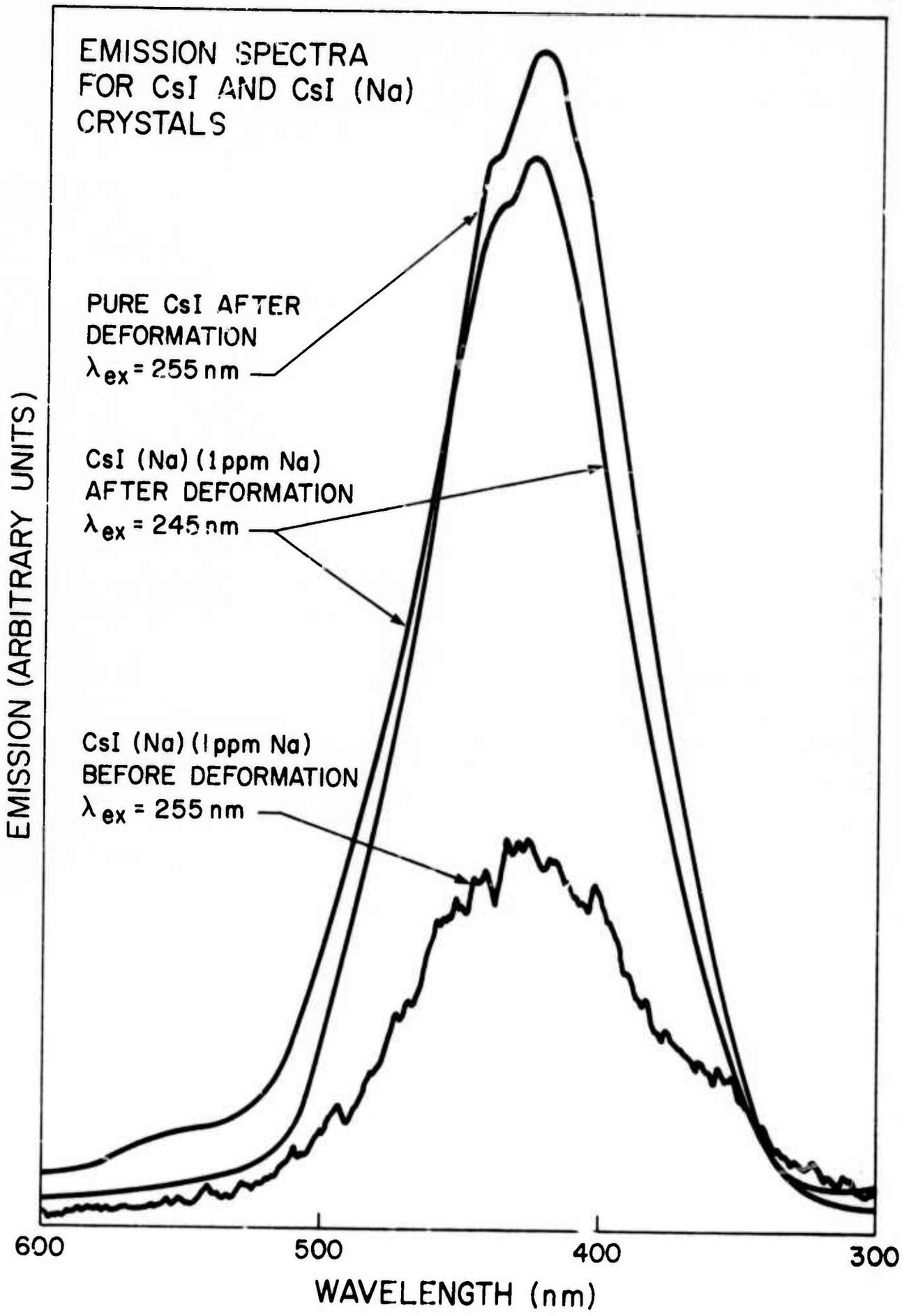
EMISSION SPECTRA
FOR CsI AND CsI (Na)
CRYSTALS
PURE CsI AFTER
DEFORMATION
λ_{ex} = 255 nm
CsI (Na) (1 ppm Na)
AFTER DEFORMATION
λ_{ex} = 245 nm
CsI (Na) (1 ppm Na)
BEFORE DEFORMATION
λ_{ex} = 255 nm
EMISSION (ARBITRARY UNITS)
600
500
400
300
WAVELENGTH (nm)

excess of 6ppm or why deformation (or thermal quenching) has such a pronounced effect on the intensity unless these treatments have a dissolution effect on sodium or other structural clusters already present in the lattice. Yet another possibility is that the deformation (or thermal) treatments may so substantially increase the mobility of the irradiation produced V_k centers that even the trace amounts of Na^+ present in the crystal are now quite effective as recombination sites. It is hoped that a more detailed investigation now underway will shed some light on this matter[4].

4. References

1. C. W. Bates, Jr. et.al., "Optical Properties of CsI(Na) and Heat-Treated Pure CsI", accepted for publication in Physics Letters A.

2. P. Brinckmann, Physics Letters 15, 305 (1965).

3. T. Sidler, J.-P. Pellaux, A. Nouailhat and M. A. Aegerter, Solid State Comm 13, 479 (1973).

4. C. W. Bates, Jr., O. L. Hsu and A. Salau (to be published).

D. Luminescence Phenomena in CsI(Na)

1. Introduction

Sodium-activated cesium iodide CsI(Na) is a very efficient scintillation material. Its large x-ray stopping power and its high conversion efficiency (12%) at its emission maximum of 4200Å make it an ideal x-ray detector[1]. Its narrow spectral output when bombarded by particles in the meV range and its short decay time (0.6μ sec)[2] also make it an excellent particle detector. In spite of its important role in particle applications, little work has been done on determining the luminescent mechanism in this material[2-7]. We report here the experimental procedures and results of our preliminary investigations of photoluminescent phenomena in CsI(Na) at room and liquid nitrogen temperatures, on bulk single crystals as well as polycrystalline films of this material. Other results that we obtained on pure CsI and CsI(Na) may be found elsewhere.[8-11]

2. Review of Previous Work on CsI(Na)

The blue luminescence, peaking at about 4200Å, which had been ascribed by various authors to pure CsI, anion vacancies in the matrix, activation by Si or by various alkaline earth impurities, was first identified as due to the existence of the nonisomorphic impurity Na in CsI by Brinckmann[2]. It has been found that the light output reaches a maximum at 0.01 mole% sodium and decreases at higher sodium concentrations[3]. Panova and Shiran[4,5] compared the luminescence from CsI(Na) and pure CsI crystals that had been doped with divalent cations. Owing to the similarity of luminescence properties from these crystals, they proposed a mechanism concerning the nature of luminescence centers in CsI(Na). Luminescence in this crystal they suggest is due to excitation of iodine ions whose vibronic levels are perturbed by neighboring cationic vacancies. Vacancies in this crystal can exist as a result of the nonisomorphism

of CsI and NaI and the large size difference between Cs^+ and Na^+ ions. Panova and Shiran also observed that the excitation for the blue luminescence from CsI(Na) is not fundamental - the maximum and the half-width are temperature dependent. This indicates that not only cation vacancies, but also other less efficient lattice defects, participate in this process. However, no work has been done on determining this "secondary" defect nor on determining whether the Na^+ ions and the cation vacancies are associated or isolated in the lattice. There is also no published work concerning whether or not this emission is a superposition of several emissions such that other centers might be involved in this luminescence process. Our work in this area is aimed towards answering some of these questions.

3. Experimental Details

The single crystals of CsI(Na) used in this experiment were obtained from The Harshaw Chemical Company of Cleveland, Ohio. The sodium concentration of these crystals is 0.01 mole% (or 6ppm). They were cut from ingots that had been well-annealed and zone-refined. Their dimensions were ½" x ½" x 2mm.

The films were made by vacuum evaporating small fragments of crushed single crystals onto suprasil quartz II substrates which were ½" x ½" x 1mm in dimension. These quartz substrates were mounted on a stainless steel block with heaters and a chrome-alumel thermocouple embedded in it. With the heaters we were able to control the temperature of the substrates during the evaporation process and the annealing of the films after evaporation. Those films from which the spectra reported here were taken were evaporated on substrates that had been heated to temperatures in excess of 400°C for one hour in order to remove any moisture or other possible contamination and then kept at 200°C

during evaporation. These films were then cooled down to 100°C in vacuum within 2 to 4 hours and then down to room temperature by shutting off the power to the heaters.

The thickness of films was read from a Sloan Digital Thickness Monitor (DTM) which was connected to a quartz sensor head in the vacuum system and then checked by optical measurement.

Although the sodium concentration in these films has not been analyzed in these experiments it has been found previously[1] that because the vapor pressures of NaI and CsI are very close the sodium concentration in the films is the same as that in the crushed crystal from which the films were made, i.e., 0.01 mole%.

The films were then transported to the experimental dewar while continuously blowing dry nitrogen gas on them. The dewar was then pumped to vacuum quickly. The pumping system we used consisted of two Varian Vacsorb roughing pumps, a titanium sublimation pump, and a 400 ℓ/s Vacion pump. This pumping system provided fast pumping speed and extremely low contamination which is difficult to achieve with oil diffusion pumps. The pressure during an evaporation was typically about 10-9 torr.

A Cary-14 Spectrophotometer was used to measure the absorption spectra of the specimens. To measure the emission and excitation spectra, we used a conventional arrangement as shown in Fig. 1. The light source was a Bausch & Lomb deuterium lamp which had a fairly flat spectrum from 2000Å to 4000Å without any sharp lines. The light went through a grating monochromator, which had a small driving motor to provide steady scanning speed, and then through a mechanical light chopper. The chopped monochromatic light was incident upon the large face (½" x ½") of the samples, which were mounted in a small dewar capable of going to liquid nitrogen temperatures. The emission was measured

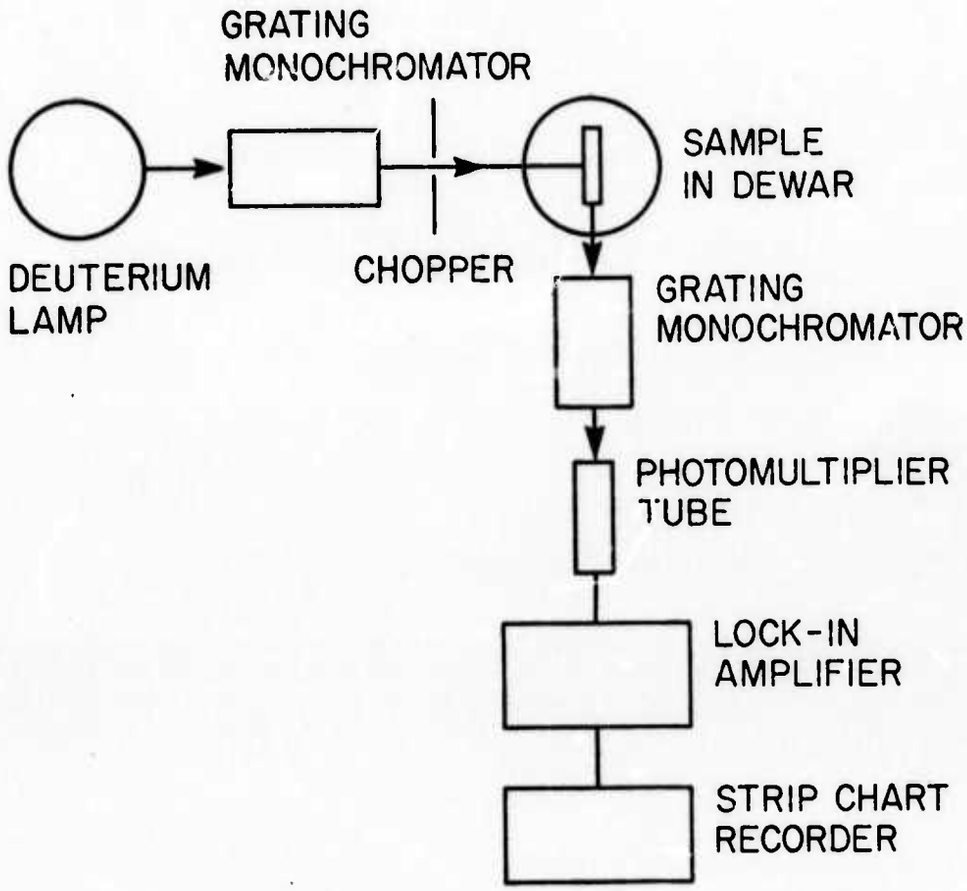

Fig. (1) Experimental arrangement used to measure emission and excitation spectra.

at right angles to the exciting light in order to avoid the interference from the transmitted and reflected light. Passing through another grating monochromator, the emission was detected by an RCA 8645 photomultiplier tube with an S-20 spectral response. The detected signal was fed into a lock-in amplifier, which picked up the reference frequency from the chopper, and then recorded by a strip chart recorder.

Measurements were made on each specimen at room temperature. Complete data of absorption, emission, and excitation spectra were taken. The specimen was then cooled to liquid nitrogen temperature and the whole experiment was repeated. A measurement was also made after the specimen had warmed back to room temperature.

4. Experimental Results

The results we obtained can be summarized as follows:

(1) Absorption spectrum

(a) Figure 2 (a) shows the absorption spectrum measured at room temperature. The absorption edge starts at about 2550Å and reached a maximum at 2250Å for the 2mm-thick single crystal. For thin films, two sharp exciton peaks were located at 2225Å and 2085Å which we were unable to resolve in the bulk crystal due to the high optical density caused by the thickness. However, the exact position of the peaks varied from film to film within a 50Å range. From the work of Lynch and Brothers[12] this result is not unexpected.

(b) Figure 2(b) is the absorption spectrum measured at liquid nitrogen temperature. At this temperature, the absorption edge of the bulk crystal was shifted to 2450Å. Three well-

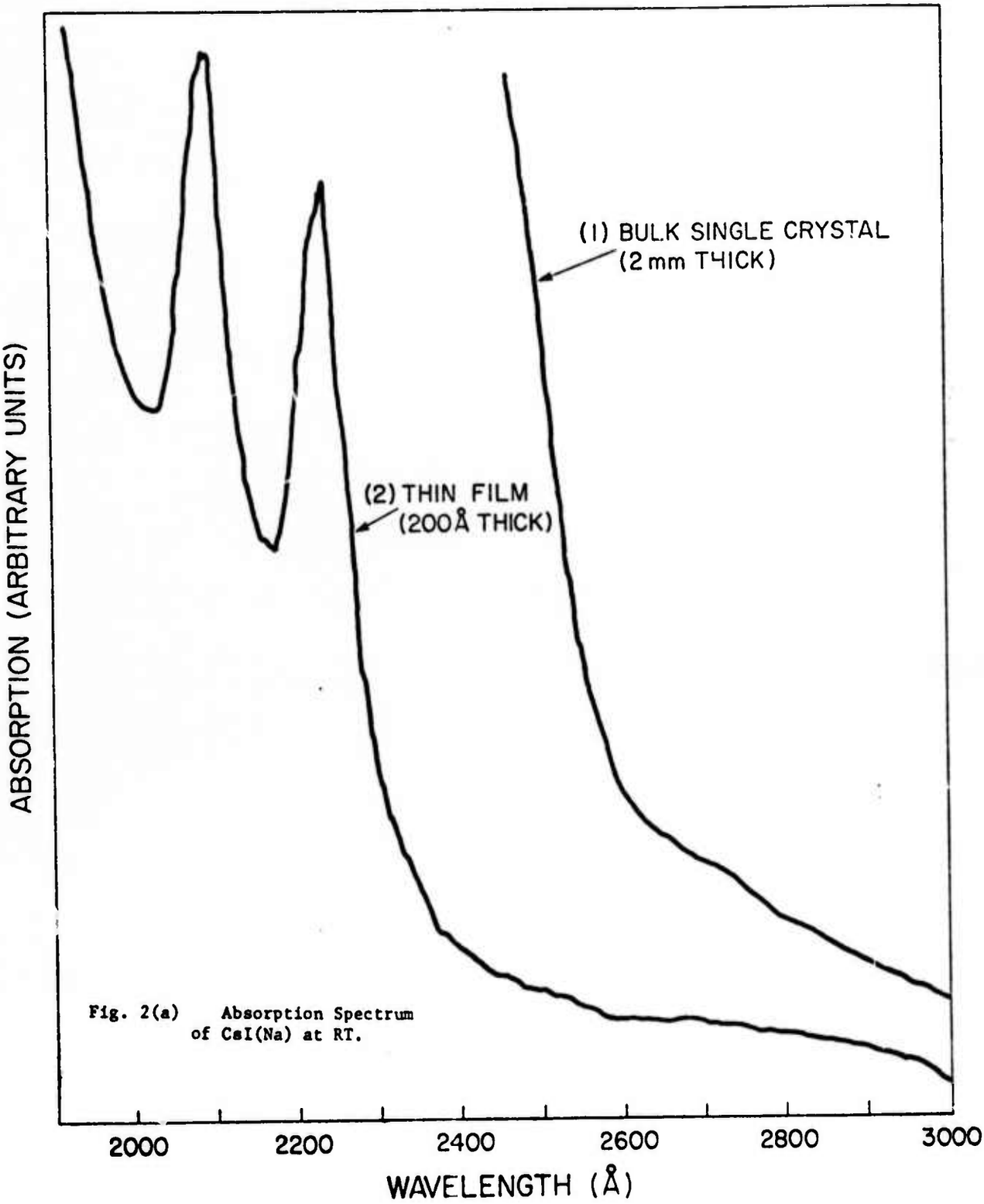

Fig. 2(a) Absorption Spectrum of CsI(Na) at RT.

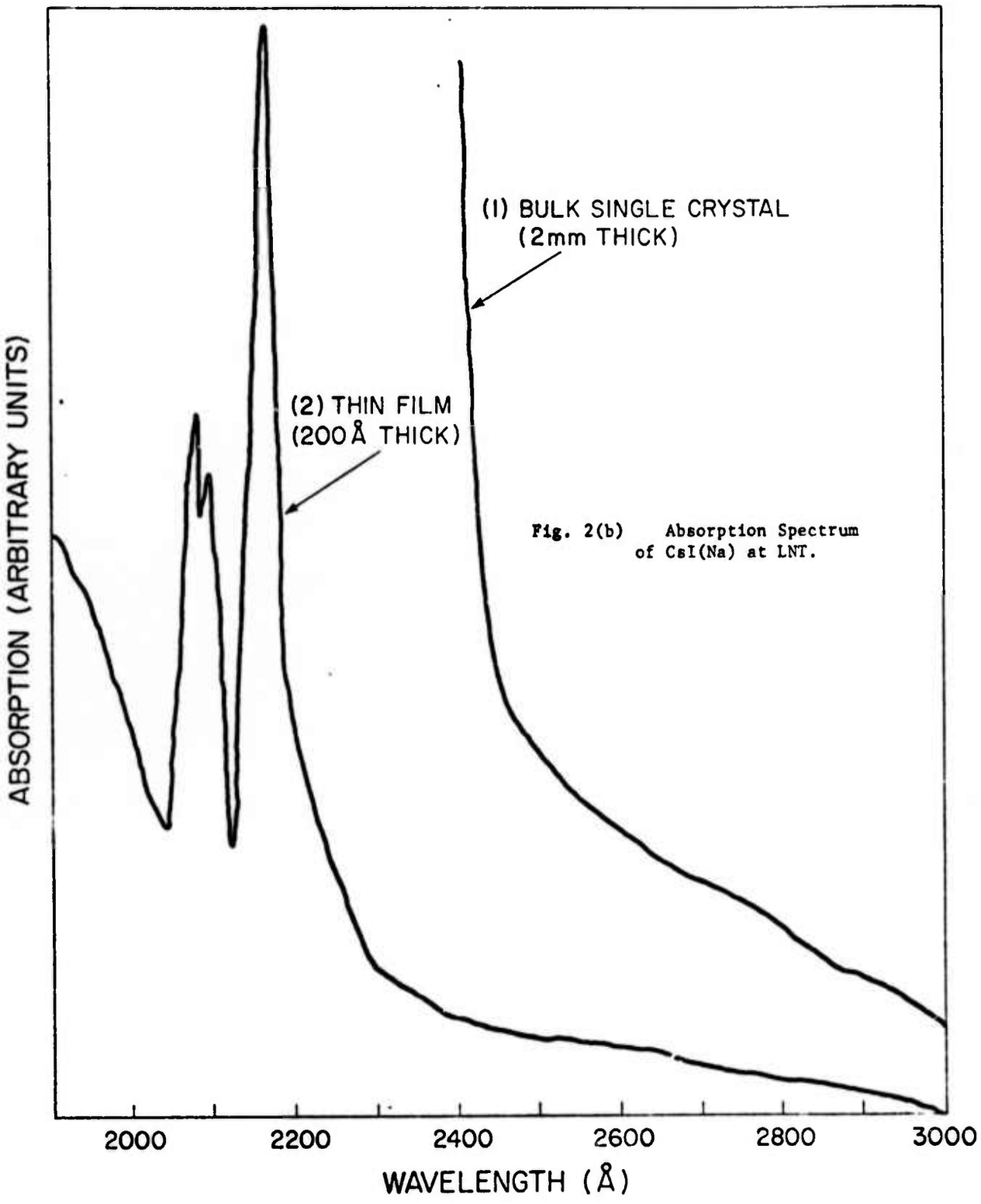

Fig. 2(b) Absorption Spectrum of CsI(Na) at LNT.

resolved exciton peaks were found at 2175Å, 2095Å, and 2080Å. The lower energy peak shifted from 2225Å at RT to 2175Å at LNT, while the higher energy one at 2085Å at RT did not shift position but split into two peaks at 2095Å and 2080Å, respectively.

(c) The absorption spectrum for bulk single crystals as well as films have a tail extended into the long wavelength region up to 2900Å.

(2) Emission and Excitation Spectra of Single Crystals

To describe the emission and excitation spectra of bulk single crystals, it is convenient for us to divide the crystals into two types, I and II: type I crystals did not give a UV emission at 3400Å at RT; type II crystals did give this emission at RT.

(a) All single crystals gave a very strong emission at 4250A with a half-width of 900Å at RT and 600Å at LNT. At RT, the corresponding excitation spectrum (fig. 3(a)) had a single peak at 2500Å with a half-width of 150Å. At LNT, the excitation spectrum varied for different crystals. For type I crystals the excitation spectrum consisted of a peak at 2400Å and a shoulder between 2300Å and 2250Å (fig. 4(a)). For type II crystals the excitation peak shifted toward 2350Å and the shoulder disappeared (fig. 4(b)). The stronger the 3400Å emission at RT was, the more the peak shifted and the more symmetrical the peak.

(b) Type II crystals gave a weak emission at 3400Å at RT when excited at 2850Å. The intensity was about $\frac{1}{20}$ to $\frac{1}{200}$ of that

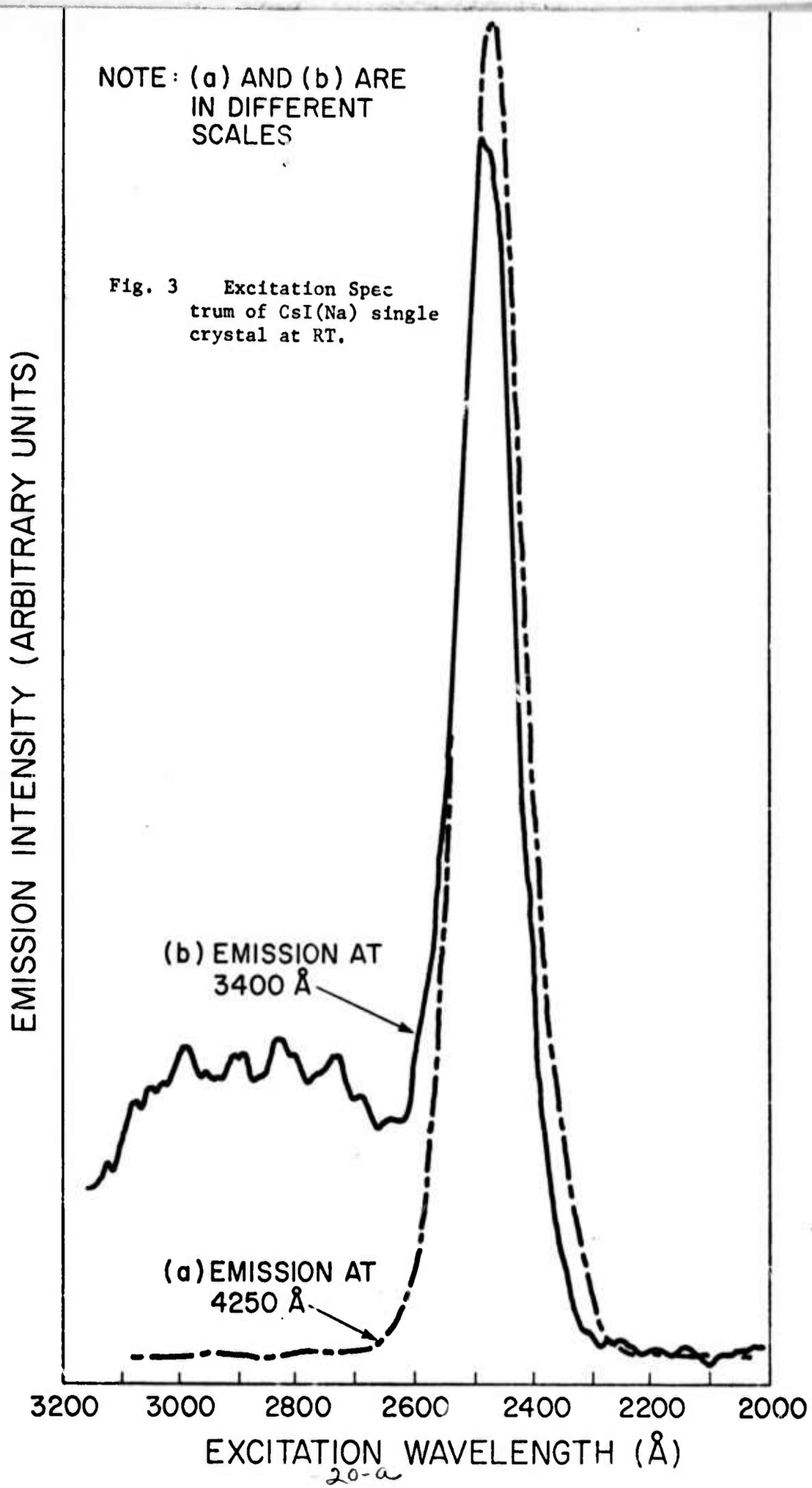

Fig. 3 Excitation Spectrum of CsI(Na) single crystal at RT.

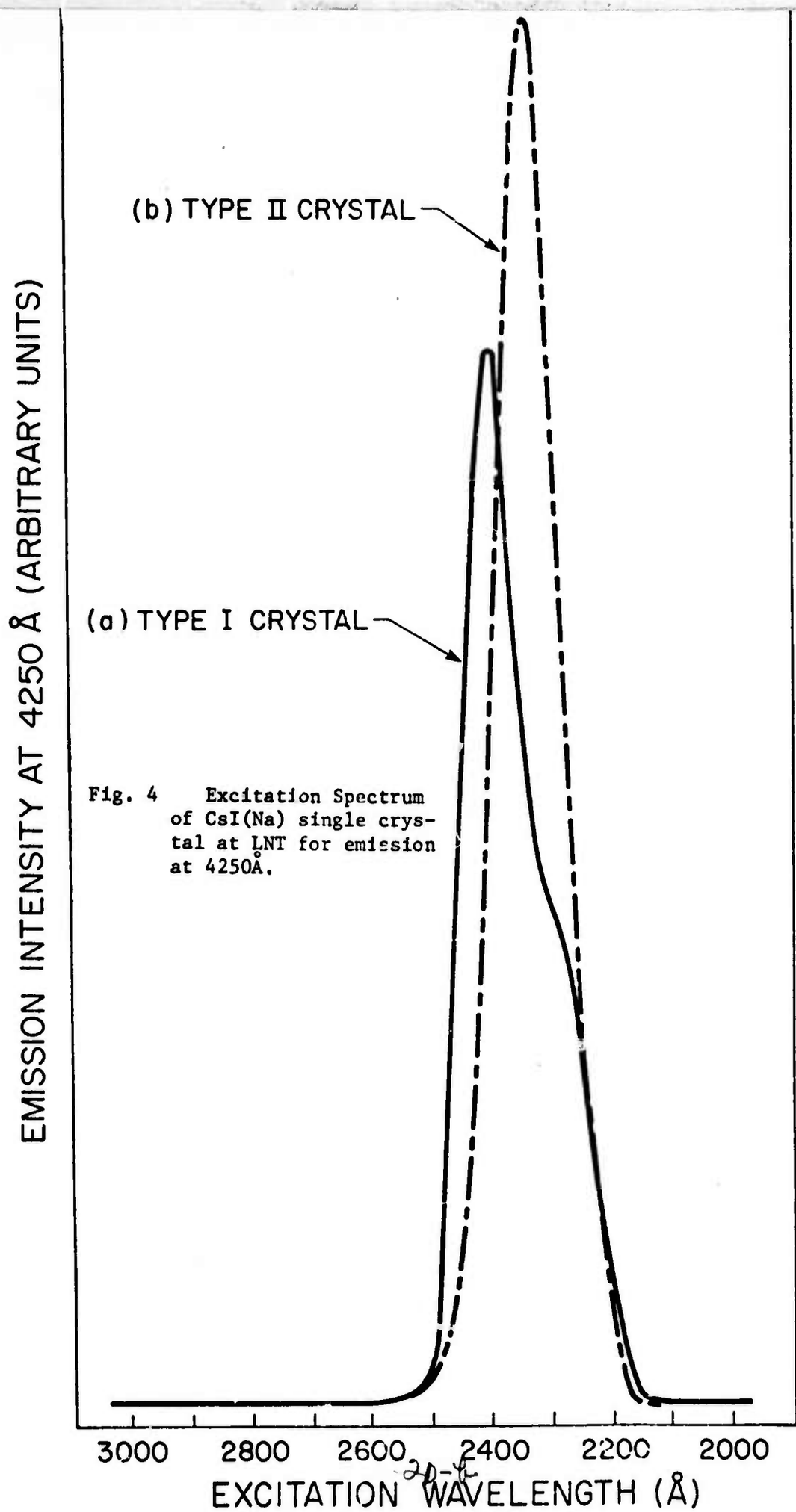

Fig. 4 Excitation Spectrum of CsI(Na) single crystal at LNT for emission at 4250Å.

of the 4200Å emission excited by 2500Å light. The excitation spectrum for this UV emission at RT is shown in fig. 3(b). (Note the hump around 2700Å ~ 3100Å.)

(c) At LNT, every crystal gave emission at 3450Å as well as one at 4250Å. A very effective excitation showed up at 2200Å. When the excitation spectra for this emission were taken, they consisted of two peaks - one at 2350Å and the other at 2200Å. The relative heights of these two peaks are different for the two types of crystals. For type I crystals, the 2350Å band was the major excitation whose height was about 10 to 20 times that of the 2200Å band (fig. 5(a)). While for type II crystals, the effectiveness of the 2200Å band increased relative to the 2350Å band. For the crystal that gave the most intense 3400Å emission measured at RT, the 2200Å band is about 4 times stronger than the 2350Å band (fig. 5(b)).

(3) Emission and Excitation of Films

There are two major emissions centered at 3500Å and 4350Å, respectively. The relative intensity of these two emissions when properly excited strongly depended on the film thickness and cooling process after evaporation.

(a) The intensity of the 4350Å emission increased relative to that of the 3500Å emission as the film thickness increased.

(b) The 3500Å emission disappeared at RT for films of thickness from 200Å to 2000Å that had been cooled extremely slowly after evaporation in order to produce strain-free films. However, this emission showed up at RT after the films had been cooled to LNT. This temperature-cycle effect was more

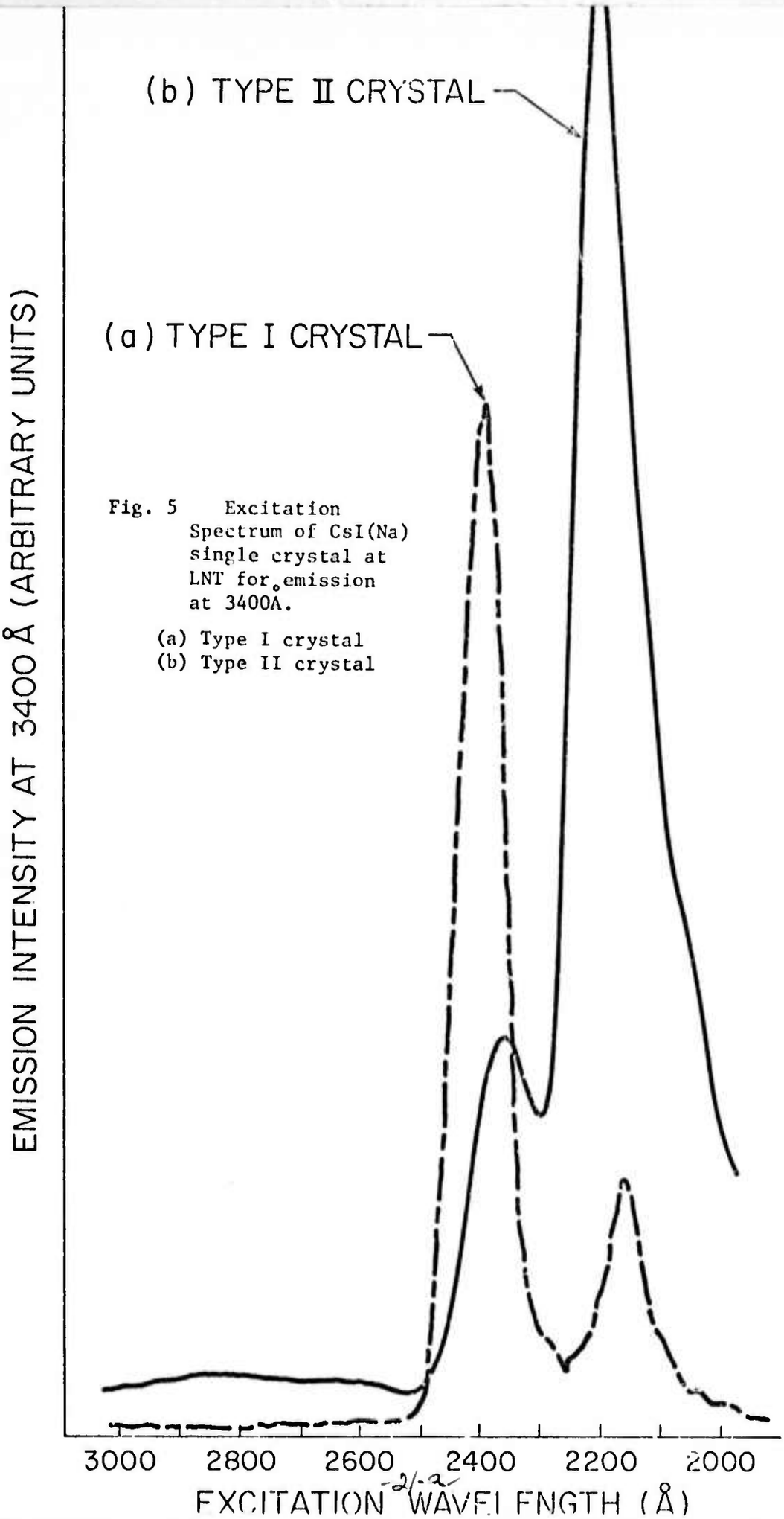

Fig. 5 Excitation Spectrum of CsI(Na) single crystal at LNT for emission at 3400Å.

(a) Type I crystal
(b) Type II crystal

important for thin films (200Å) than for the thicker ones (2000Å).

(c) Both of these emissions increased in intensity as the temperature decreased. However, the 3500Å emission increased more drastically than the 4350Å emission. For a 6000Å-thick film, which gave the same emission intensity at these two bands when properly excited, the 3500Å emission was about 10 times stronger than the 4350Å emission.

(d) The excitation spectrum corresponding to the 3500Å emission when detected at RT had a narrow peak at 2370Å and a broad hump from 2600Å to 2950Å (fig. 6(a)). At LNT, for all films, the excitation consisted of two peaks centered at 2175Å (high) and 2350Å (low), a shoulder at 2050Å and a broad band from 2600Å to 2950Å (fig. 6(b)).

(e) The excitation spectrum (fig. 7) corresponding to the 4350Å emission behaved in a rather peculiar way. At RT before cooling down to LNT, this emission was appreciable only for thick films (about 6000Å) and the excitation consisted of two broad bands centered at 2700Å and 3750Å with half-widths of about 400Å. The latter band which was not observed from other thinner films did not change its absolute (not relative) height at LNT and disappeared when the film was warmed back to RT. Since the origin of this band is not clear at this time, we will not discuss it further. At LNT, the excitation spectrum consisted of two peaks of the same height centered at 2350Å and 2700Å. When the films were warmed back to RT, these two excitation bands were preserved although the emission

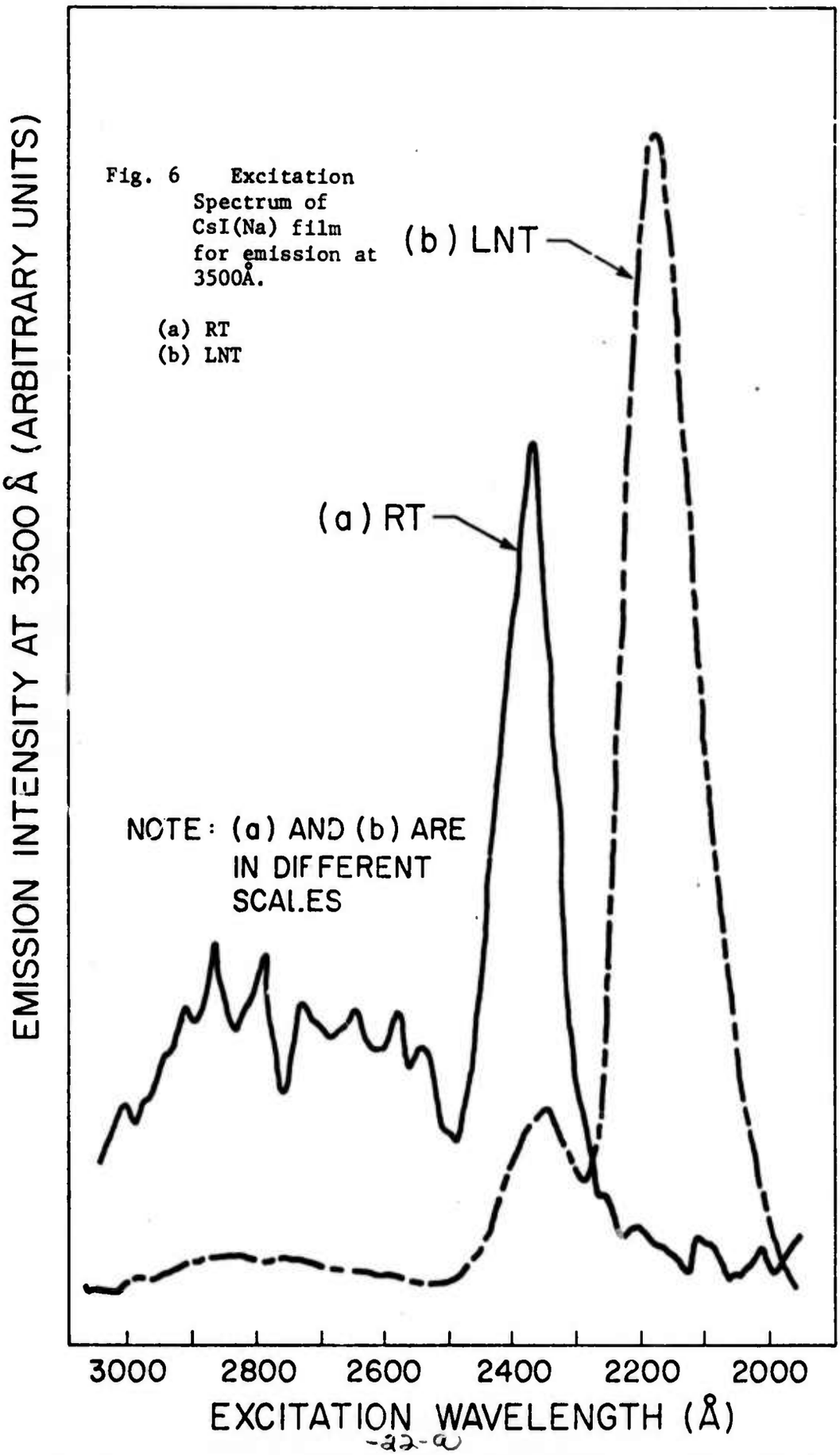

Fig. 6 Excitation Spectrum of CsI(Na) film for emission at 3500Å.

(a) RT
(b) LNT

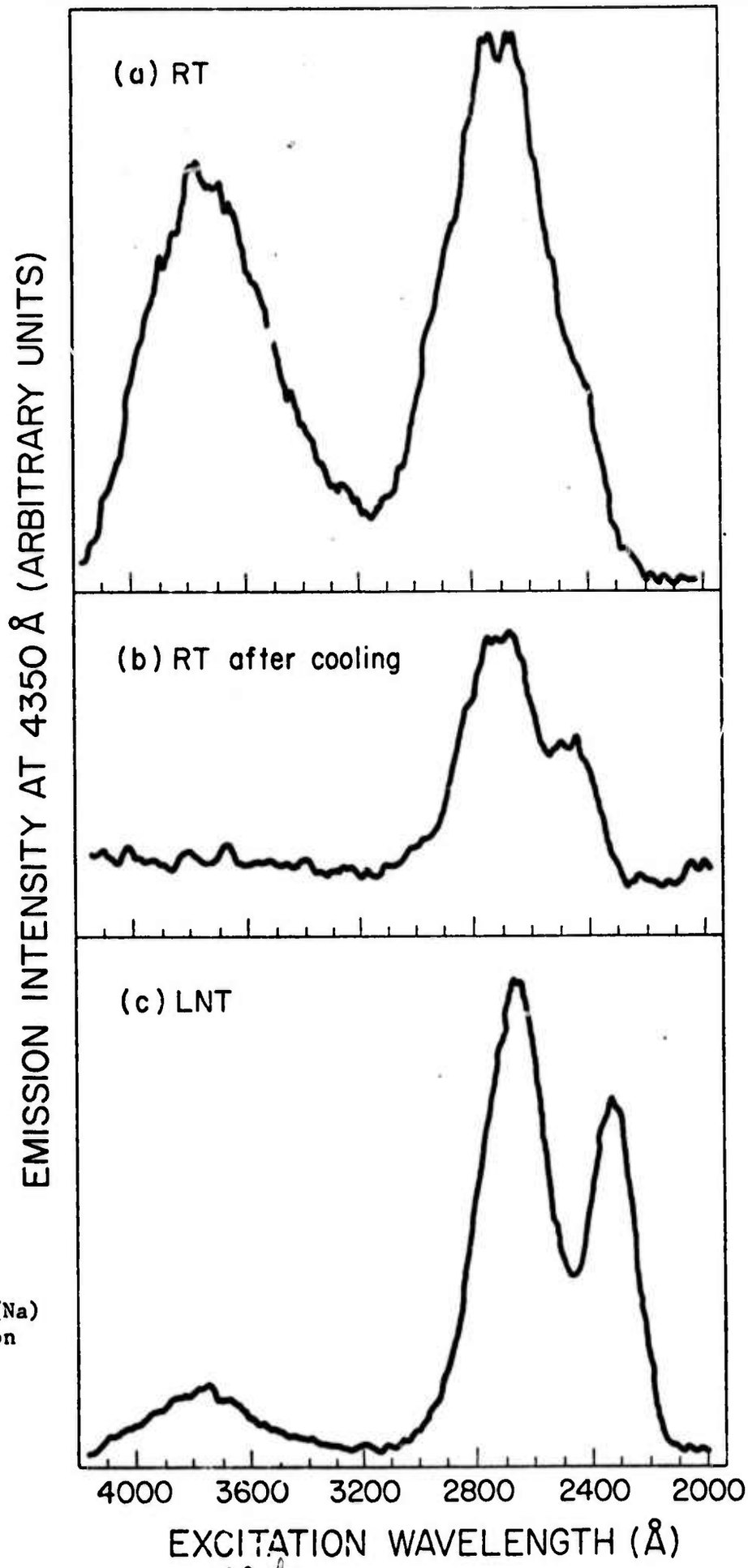

Fig. 7 Excitation Spectrum of CsI(Na) film for emission at 4350Å.

(a) RT
(b) RT after LNT
(c) LNT

intensity decreased drastically.

5. Discussion of Results

The absorption spectra are in good agreement with the work by Eby, et.al.[13] and Lamatsch, et.al.[14]. The peak at 2225Å at RT, which shifts to 2175Å at LNT, is the lower energy component of the normal spin-orbital doublet of the p^5s configuration, while the one at 2085Å at RT, which split into two closely separated peaks at LNT, arises from the p^5d configuration[15]. From the theoretical work of Phillips[16], the peaks at 2175Å and 2095Å (at LNT) are identified as the Γ exciton and the last one at 2080Å is an X exciton of the host CsI lattice. The thickness dependence of the position of the lowest energy peak is not clear at this time. The absorption in the long wave-length tail of the fundamental absorption is an important effect because it was not observed in pure CsI[10] and it is in this region where the emission at 4250Å is most effectively excited. Absorption in this region might be due to perturbed exciton states by defects introduced by sodium ions. More work will be done at lower temperatures to further elucidate this phenomena.

The blue emission at 4250Å, which is the character of sodium-activated cesium iodide, was well defined in the measurements done on single crystals. It is not surprising that this emission is extremely weak in the thin film samples. If we consider that the sodium concentration in the films is 0.01 mole%, the distance between two sodium ions is about 120Å. For a 200Å-thick film, there are only about two sodium ions in a row and the emission from two centers is too weak to be detected with our set-up. As a matter of fact, this emission increased relative to the 3500Å emission as the thickness of film increased, i.e., as the number of sodium ions in the film increased.

The shift of wavelength of the emission from 4250Å for bulk crystals to 4350Å for thin films and the change of the corresponding excitation spectrum

is a thickness effect that is unknown at this time. In fact, due to the low emission intensity from the films, the detected spectrum was noisy, and an accurate position of the peak was somewhat difficult to determine. More work will be done to systematize this thickness effect and its association with the UV emission.

The emission at 3500Å, which is excitonic emission, was also found in pure CsI and CsI doped with divalent impurities such as Ca^{++}, Sr^{++}, Mg^{++}[10,14,17]. What makes our result interesting is that our emission was measured at RT as well as at LNT. It was found that this emission was closely related to the heat treatment process that the specimen received. Carefully annealed thin films (cooling rate about 0.3°C/min) did not give this UV emission at RT before cooling to LNT. Films which were evaporated on substrates held a 200°C during evaporation and then cooled fairly rapidly (about 1°C/min) to room temperature and those evaporated on substrates held at RT during evaporation showed a very strong emission at 3500Å at RT. One of the measured type II crystals that gave the most intense 3500Å emission at RT and most effective excitation at 2200Å at LNT had been heated to 500°C, kept at that temperature for about one hour, and cooled to RT within 4 to 5 hours before measurement. This room temperature UV emission might suggest a stable exciton configuration at RT. Details about this proposed hypothesis will be reported at a later date[11].

Work is presently underway to extend our measurements from above room temperature (70°C) continuously down to liquid helium temperature. In this manner we will be able to study the temperature dependence of all quantities measured previously, i.e., emission, excitation and absorption, over a wide temperature range. These studies will be particularly important for revealing the character of the absorption in the long wavelength tail of the fundamental absorption which is not present in pure CsI. In addition to these measurements, polarization studies will also be made to determine, if possible, the symmetry of the luminescent centers and the association of the sodium ions with these centers.

6. References

1. C. W. Bates, Jr., Appl. Opt. 12, 938 (1973).

2. P. Brinckmann, Phys. Letters, 15, 4, 305 (1965).

3. G. Breiter and G. Schultz, Phys. Letters 24A, 6, 331 (1967).

4. A. Panova and N. Shiran, Bull. Acad. Sci. USSR Phys. Ser. (USA) a translation from Izv. Akad. Nauk. SSSR Ser. Fiz. 35, 7, 1348-51 (1971).

5. A. Panova and N. Shiran, Opt. Spect. 32, 55 (1972).

6. A. Panova and N. Shiran, Opt. Spect. 32, 108 (1972).

7. T. Sidler, J. P. Pellaux, A. Nouaidhat and M. A. Aegerter, Solid State Comm. 13, 479-482 (1973).

8. C. W. Bates, Jr., et. al., "Optical Properties of CsI(Na) and Heat-Treated Pure CsI", accepted for publication in Physics Letters A.

9. C. W. Bates, Jr., et. al., "Strain-Induced Room Temperature Photoluminescence in CsI and CsI(Na)", (accepted for publication in Solid-State Communications).

10. A. Salau and C. W. Bates, Jr., "Luminescence Phenomena in Pure CsI" (submitted to Journal of Luminescence).

11. C. W. Bates, Jr., "Room Temperature Bound Excitons in Pure CsI" (to be submitted for publication).

12. D. W. Lynch and A. D. Brothers, Phys. Rev. Letters 21, 689 (1968).

13. J. E. Eby, K. J. Teegarden, and D. B. Dutton, Phys. Rev. 116, 5, 1099-1105 (1959).

14. H. Lamatsch, J. Rossel and E. Saucer, Phys. Stat. Sol. 41, 605 (1970); 46, 687 (1971), 48, 311 (1971).

15. K. Teegarden and G. Baldini, Phys. Rev. 155, 896 (1967).

16. J. C. Phillips, Phys. Rev. 136, A 1721 (1964).

17. M. Aegerter et. al., Proceedings of the International Symposium on Luminescence, Munich, 1965, pg. 283.

E. Luminescence Phenomena in CsI

1. Introduction

The study of the optical properties of thin films and bulk single crystals of pure CsI was undertaken because relatively little work has been done on the optical properties of alkali halide crystals (AHC) with the CsCl structure and it is one of the most sensitive detectors of ultra-violet radiation[1-6].

In this paper, the optical properties of CsI were studied by measuring the emission, excitation and ultra-violet absorption spectra of these specimens as the temperature was cycled from room temperature to liquid nitrogen and back to room temperature. We denote this cycling by RTBC (room temperature before cooling) → LNT (liquid nitrogen temperature) → RTC (room temperature after cooling). Photoexcitation was limited to the fundamental absorption edge and the excitonic region which in CsI is 235 and 205-220nm respectively.

Of particular interest in this work is the RTAC luminescence observed for excitation at the fundamental absorption edge (235nm) which has never been reported before. This RTAC luminescence peaked at 350 and 450nm for thin films and bulk single crystals respectively.

The mechanism responsible for this RTAC luminescence was probed in the light of recent experiments on photoluminescence of (i) samples that had been not only temperature cycled (RTBC → LNT → RTAC) but also irradiated at LNT and then re-annealed and (ii) temperature cycled samples which had not been irradiated at LNT. Measurements at RTBC and RTAC were taken for (i) and (ii) respectively.

2. Review of Previous Work

In an attempt to understand the centre responsible for the observed luminescence in AHC[7-10], most of these crystals were doped with monovalent or divalent impurities[11-15] like Na^{+}, Tl^{+}, Li^{+}, Sr^{++}, Ms^{++} which introduced electron

traps in the case of the monovalent impurities and cation vacancies in the divalent impurities case; while others were irradiated with high energy particles such as x-rays or γ-rays to create colour centres[16-20]. Recent studies showed that energies of the order of 5ev is enough to create F-centres in AHC[21-22].

The intrinsic luminescence which occurs at LNT in AHC has been explained by Kabler and also Murray and Keller[23] to be from the excited state of the system of a V_k centre (self-trapped hole) plus an electron, this configuration being denoted by $(V_k + e)^*$. This model has been used extensively to explain the intrinsic luminescence of AHC excited with either ultra-violet light or with x-rays at low temperatures. There is limited literature on the optical properties of pure and relatively strain free CsI as with other AHC with simple cubic structures[24-26]. The present work is on relatively strain free or defect free pure CsI. Some authors have studied the optical properties of deformed bulk single crystals of CsI[27-31]. One of these authors[27] observed an emission that peaked within the range 415-430nm - the so-called blue luminescence (BL) at RTBC in their deformed specimens (that is specimens in which structural lattice defects or strain have been introduced). At LNT, these authors observed besides the BL, an ultra-violet luminescence (UVL) peaking within the range 330-360nm for both excitonic and fundamental edge excitations.

In the present work no RTBC emission is observed while at LNT both UVL (345-360nm) and BL (410-470nm) are observed for both excitonic and fundamental edge excitations. The UVL is much more intense than the BL in thin films for both excitations while in bulk single crystals UVL is more intense for excitonic excitation and BL is more intense than UVL for edge excitations.

3. Experimental Procedures and Results

The suprapure powder of pure CsI used for the evaporation of the thin

films was obtained from the Merck Company while the Harsaw Chemical Company provided the bulk single crystals of pure CsI with sodium content less than a part per million. These bulk single crystals measured 1.27 x 1.27 x 0.2cm in size.

The vapour deposition technique was used to evaporate our films[32]. These films were either evaporated on cold (300°K) or hot (400°K) suprasil quartz substrates (1.27 x 1.27 x 0.1) cm in size and then annealed over a period of 12 hours (~8.3°K/hr) to produce relatively strain or defect free films. A more rapid cooling gave strained films that luminesced at RTBC[33]. The thickness of the films deposited were measured by a Sloan DTM guage connected to a sensor head in the Vacuum Chamber.

A Carry 14 spectrophotometer was used to measure the ultra-violet absorption spectra of all samples while the experimental set-up for the emission and excitation spectra is as shown in Fig. (1).

The emission, excitation and ultra-violet absorption spectra for all samples were taken in the sequence RTBC → LNT → RTAC.

4. Results

The ultra-violet absorption spectra of the thin films (600Å) and bulk single crystals of pure CsI are shown in Figs. (2) and (3) respectively.

At room temperature (both before and after cooling) absorption peaks occurred at 220 (1st exciton band) and 205nm, while these peaks sharpened and the 220nm band shifted to 215nm at LNT as shown in Fig. (2). From Fig. (3) for the bulk single crystals we see that the absorption peaked at 220nm while the second band (205nm) flattens out at RTBC and RTAC. That the exciton peaks are not well resolved in this thick sample is due to the high absorption of the thicker sample. At LNT, the 220nm band sharpens and splits into two bands at 218 and 215nm while the 205nm band narrowed and sharpened though did not change position.

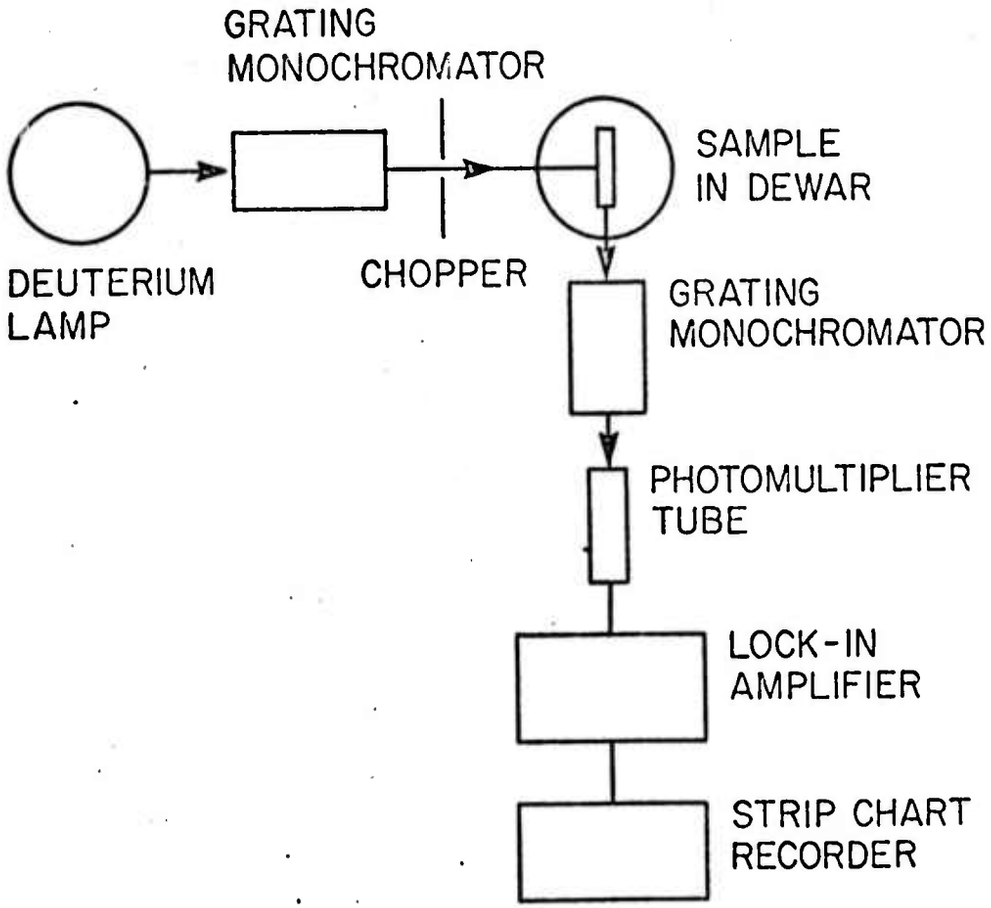

Fig. (1) Experimental arrangement used to measure emission and excitation spectra.

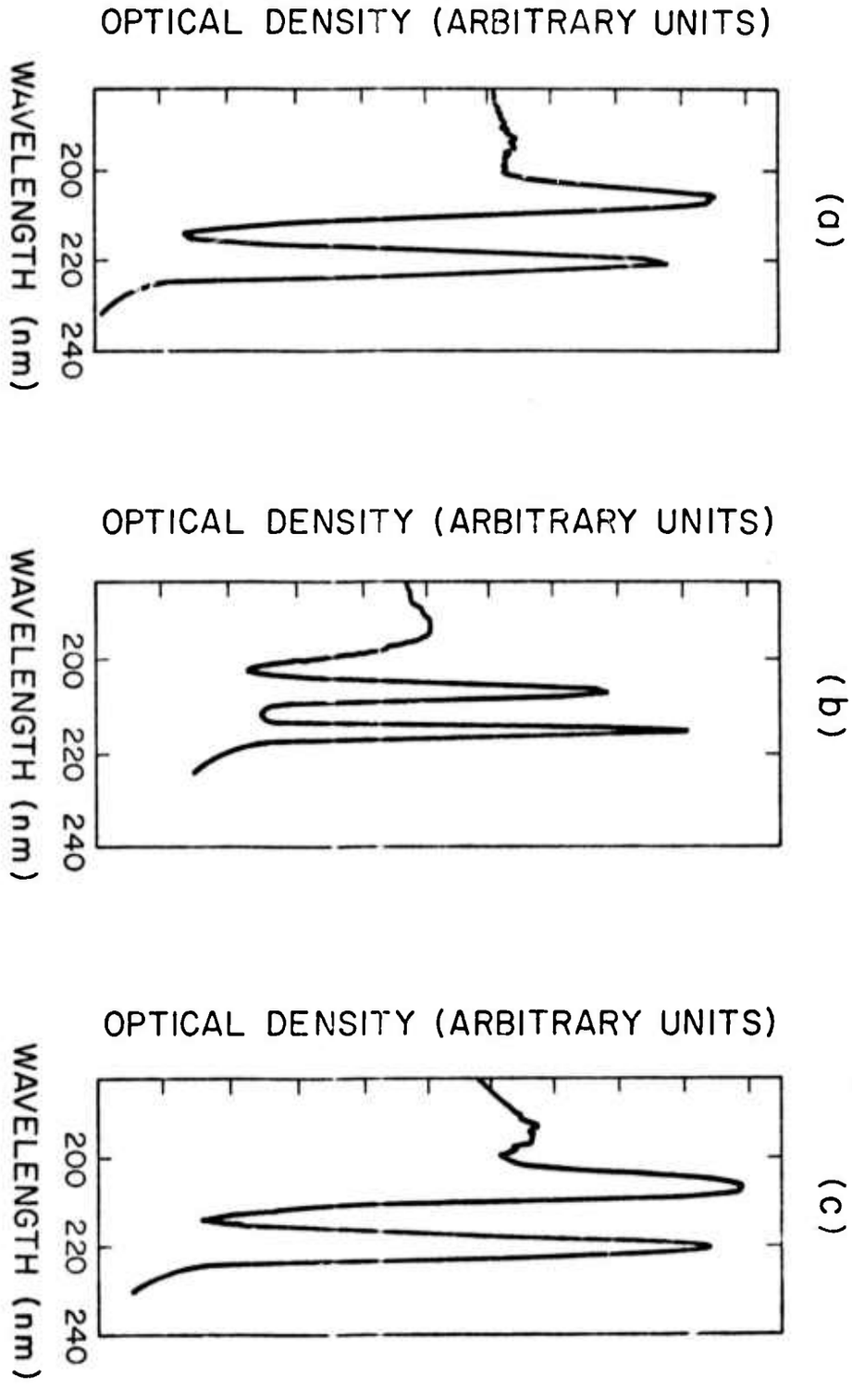

Fig. 2 Absorption spectra of thin film at (a) RTBC, (b) LNT and (c) RTAC.

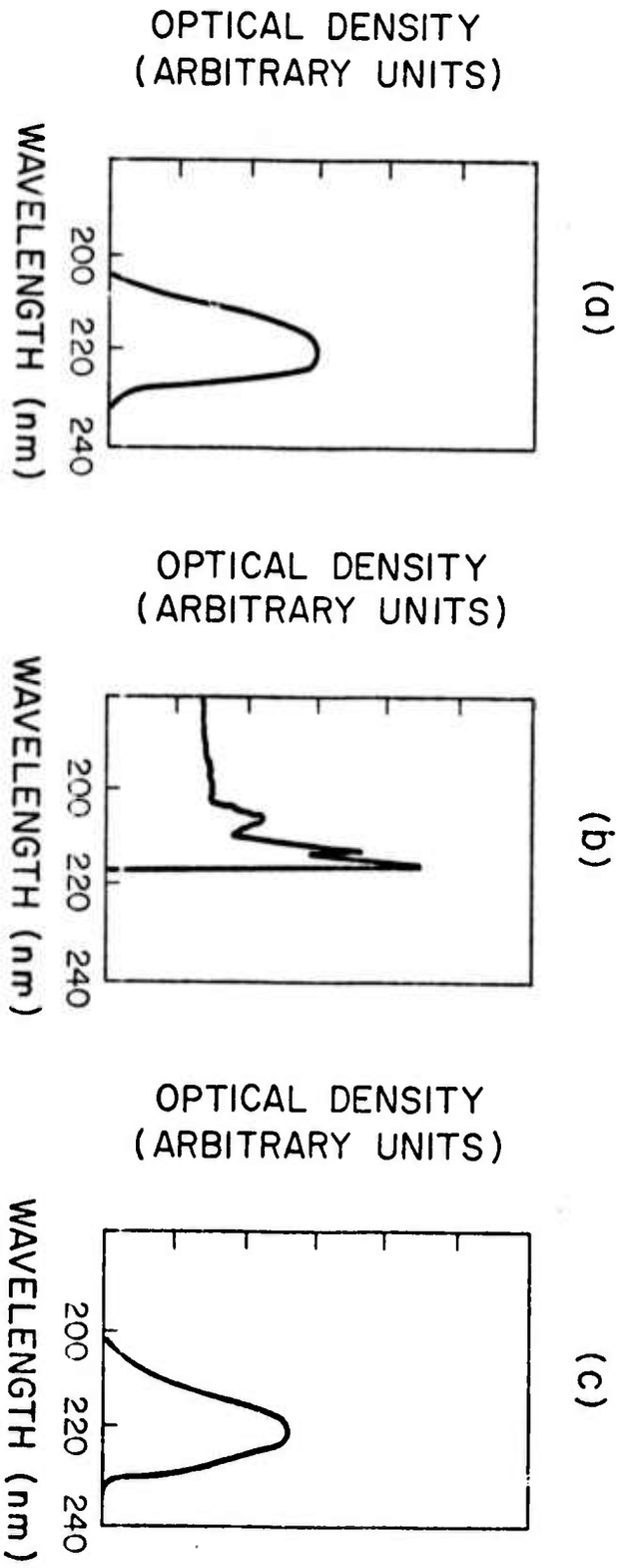

Fig. 3 Absorption spectra of bulk single crystal at (a) RTBC, (b) LNT, and (c) RTAC.

Figure (4) shows the emission spectra which were measured for the thin (600Å) films of pure CsI. At RTBC, there was no emission for excitations at the edge (235nm) or the excitonic (205-220nm) region. As we go down to LNT, excitation in the excitonic region gave emission that peaked at 350nm while the fundamental absorption edge excitation gave besides the 350nm emission a very small hump at 430nm. When the sample warmed back to room temperature, RTAC measurements showed emission which peaked at 350nm. This RTAC emission is reported here for the first time.

In Fig. (5) is shown the excitation spectra for the ultra-violet emission at 350nm at LNT and RTAC for the thin films. At LNT, the excitation spectra peaked sharply at 217nm with a smaller one at 235nm while at RTAC, a large peak occurred at 235nm with a small one at 280nm.

The bulk single crystals of pure CsI gave no emission at RTBC while at LNT, (Fig. 6a) we observed both the ultra-violet (350nm) and blue (420-430nm) emissions for excitonic and fundamental absorption edge excitations. RTAC measurements showed emission that peaked at 470nm and 540nm for edge (235nm) excitation as shown in Fig. 6b. Excitation spectra (Fig. 7a) of the UV-emission at 350nm peaked at 220nm with a small hump at 235nm while those of blue (420-430 nm) emission peaked at 240-250nm or the long wavelength tail of the fundamental absorption. In Fig. 7b is shown the RTAC excitation spectra for emissions at 470 and 540nm. Both emissions have their excitation peak at ~237nm.

In an attempt to understand the RTAC emission we observed, we performed photoluminescence measurements on two samples treated differently: (1) a sample which did not luminescence at RTBC but was cooled to LNT (without irradiation at this temperature) and allowed to warm up to room temperature (RTAC). RTAC measurements showed emission at 350nm for edge excitation as shown in Fig. 8a (2) One of the samples which showed RTAC emission was annealed at 420°K for about

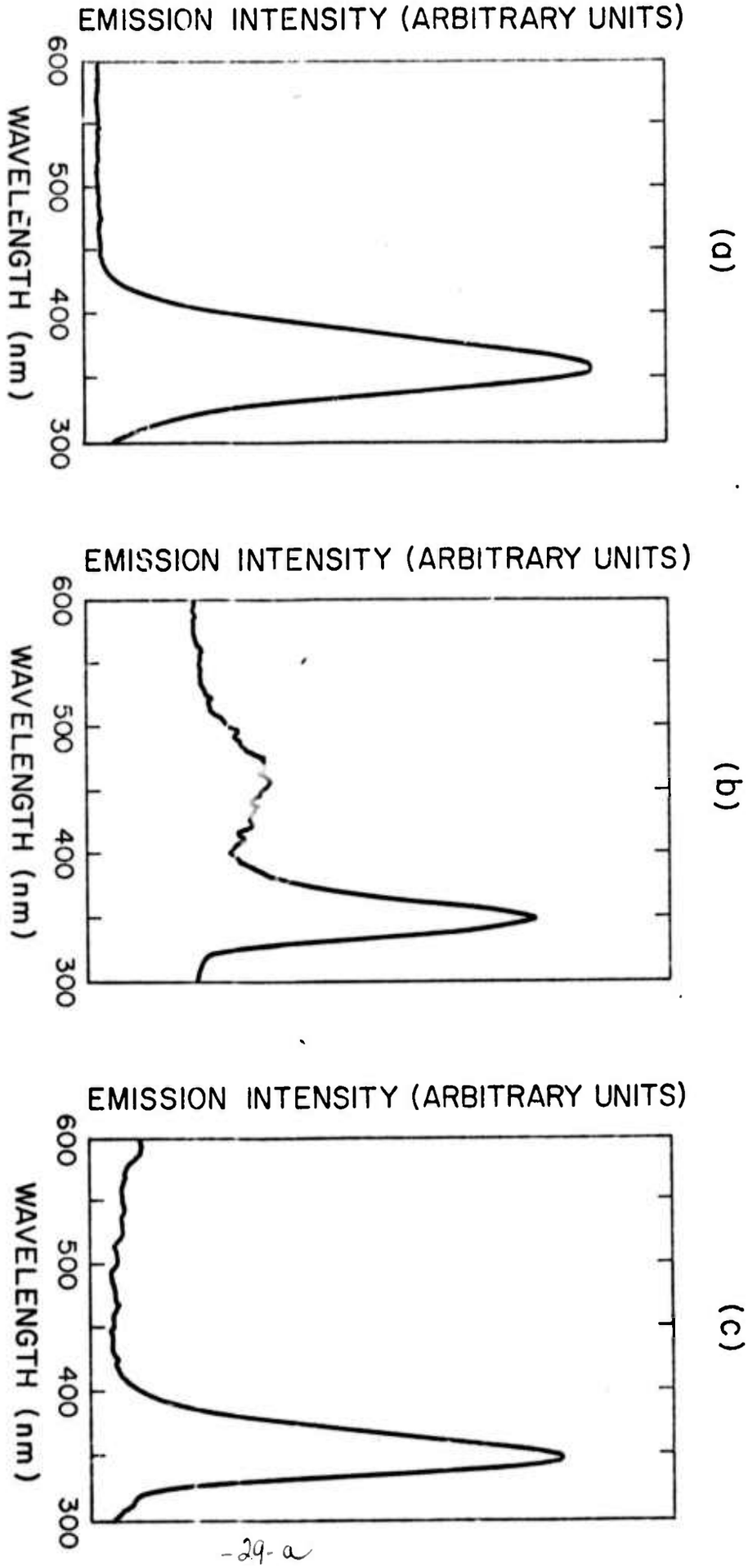

Fig. 4 Emission spectra of thin film of CsI at
(a) LNT for λ_{ex}=215nm
(b) LNT for λ_{ex}=235nm
(c) RTAC for λ_{ex}=235nm

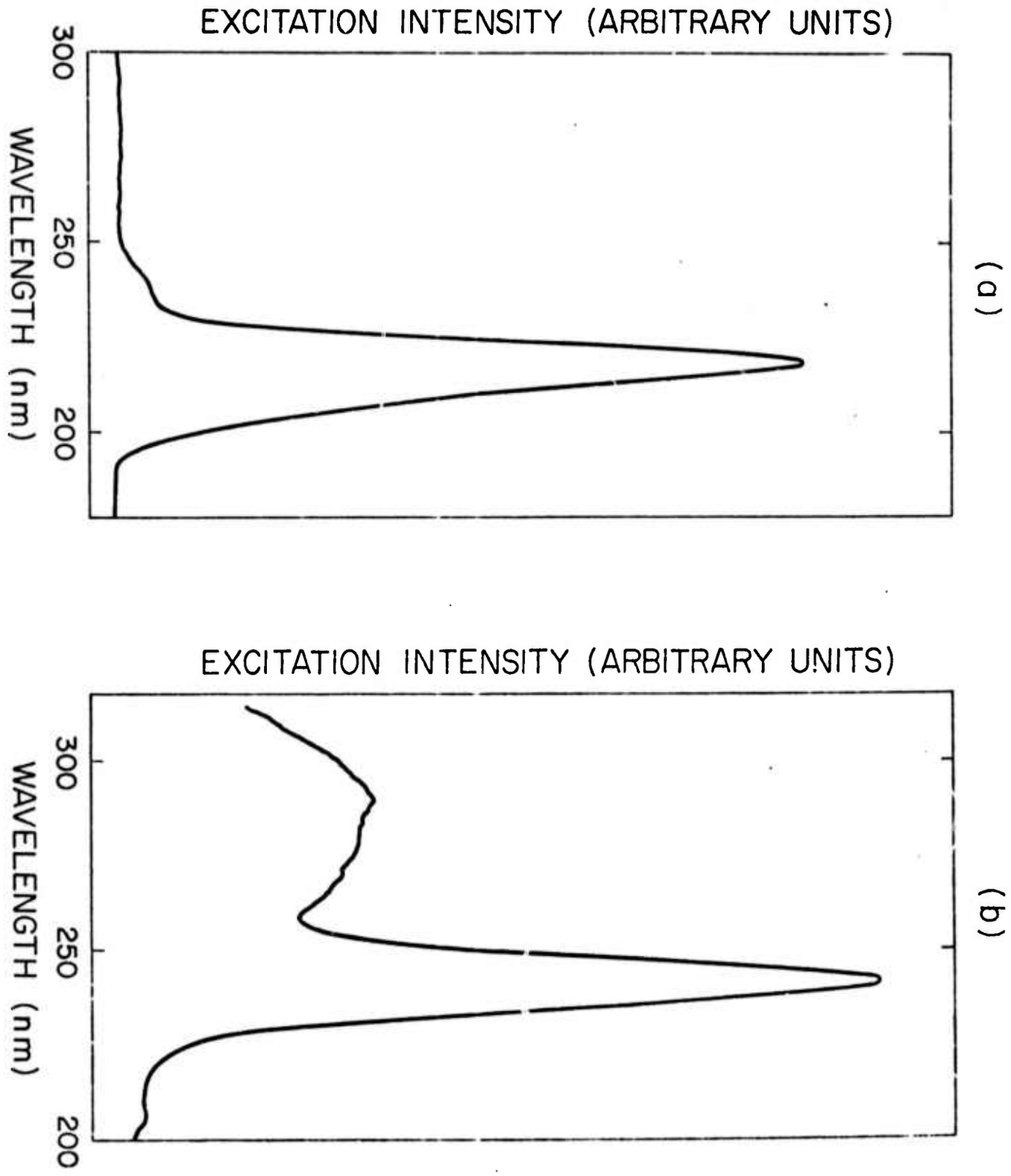

Fig. 5 Excitation spectra of thin film of CsI at
(a) LNT for emission at 350nm
(b) RTAC for emission at 350nm

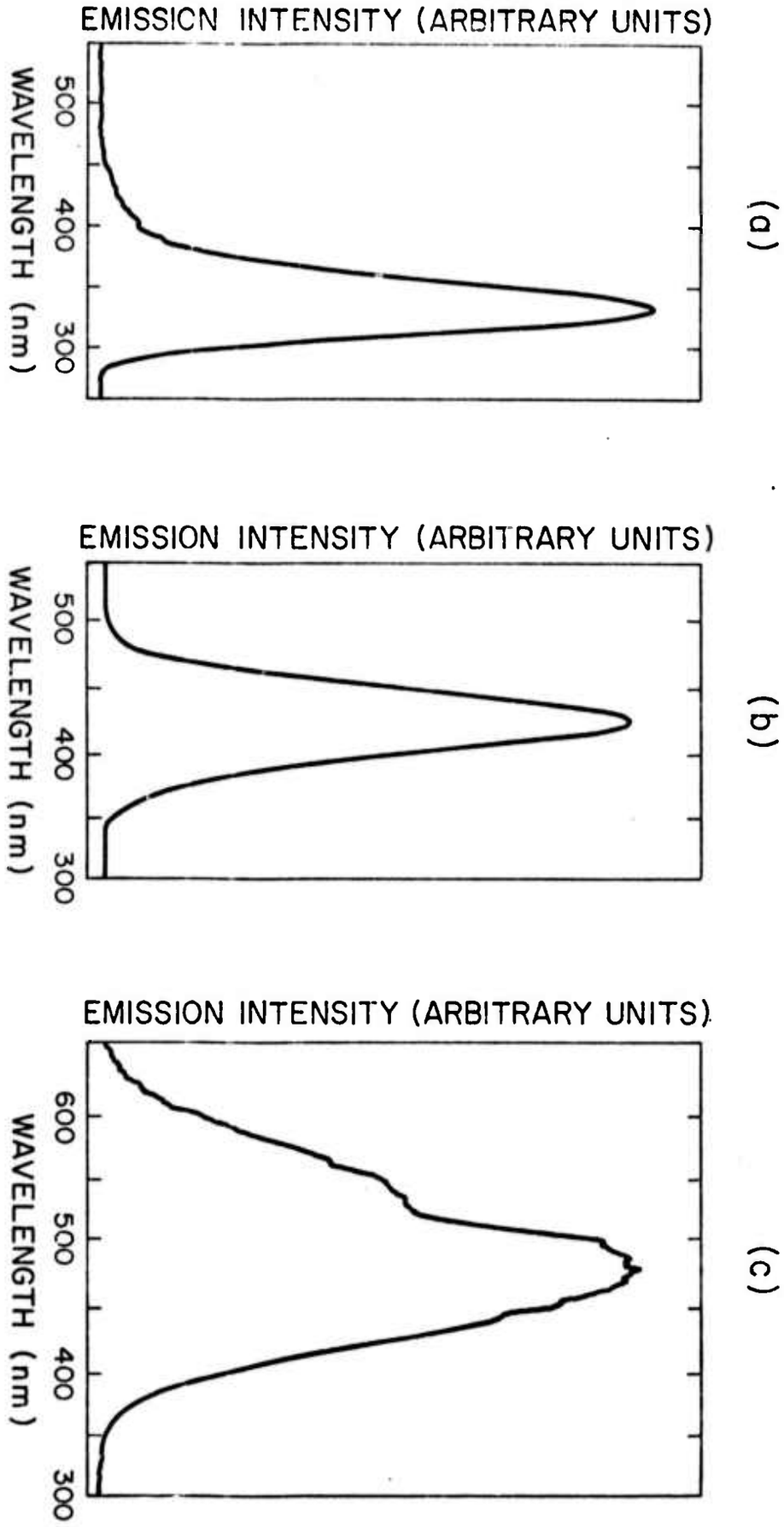

Fig. 6 Emission spectra of bulk single crystal of CsI at
(a) LNT for excitation at 215nm
(b) LNT for escitation at 235nm
(c) RTAC for excitation at 235nm

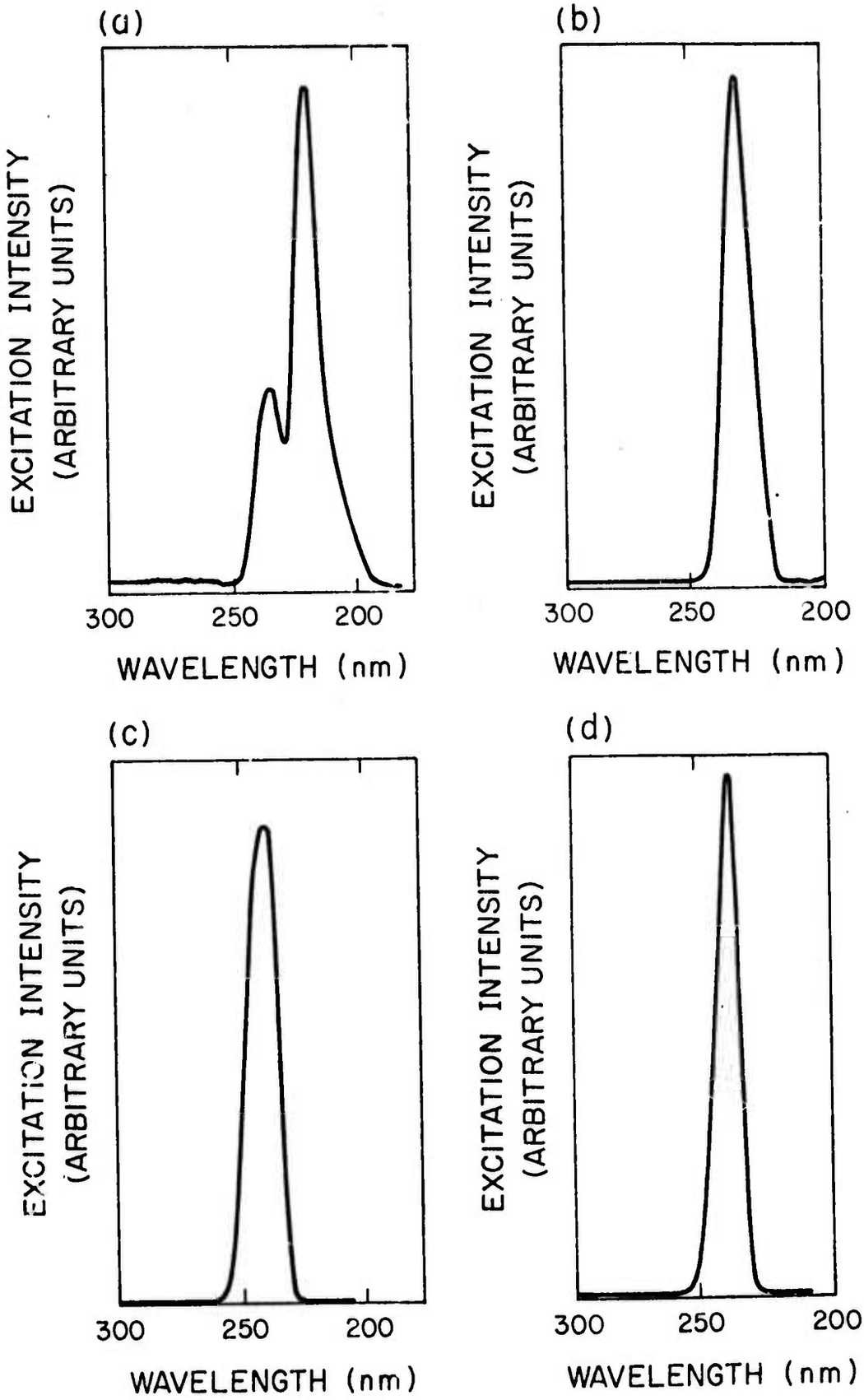

Fig. 7 Excitation spectra of bulk single crystal of CsI at
(a) LNT for emission at 350nm
(b) LNT for emission at 425nm
(c) RTAC for emission at 470nm
(d) RTAC for emission at 540nm

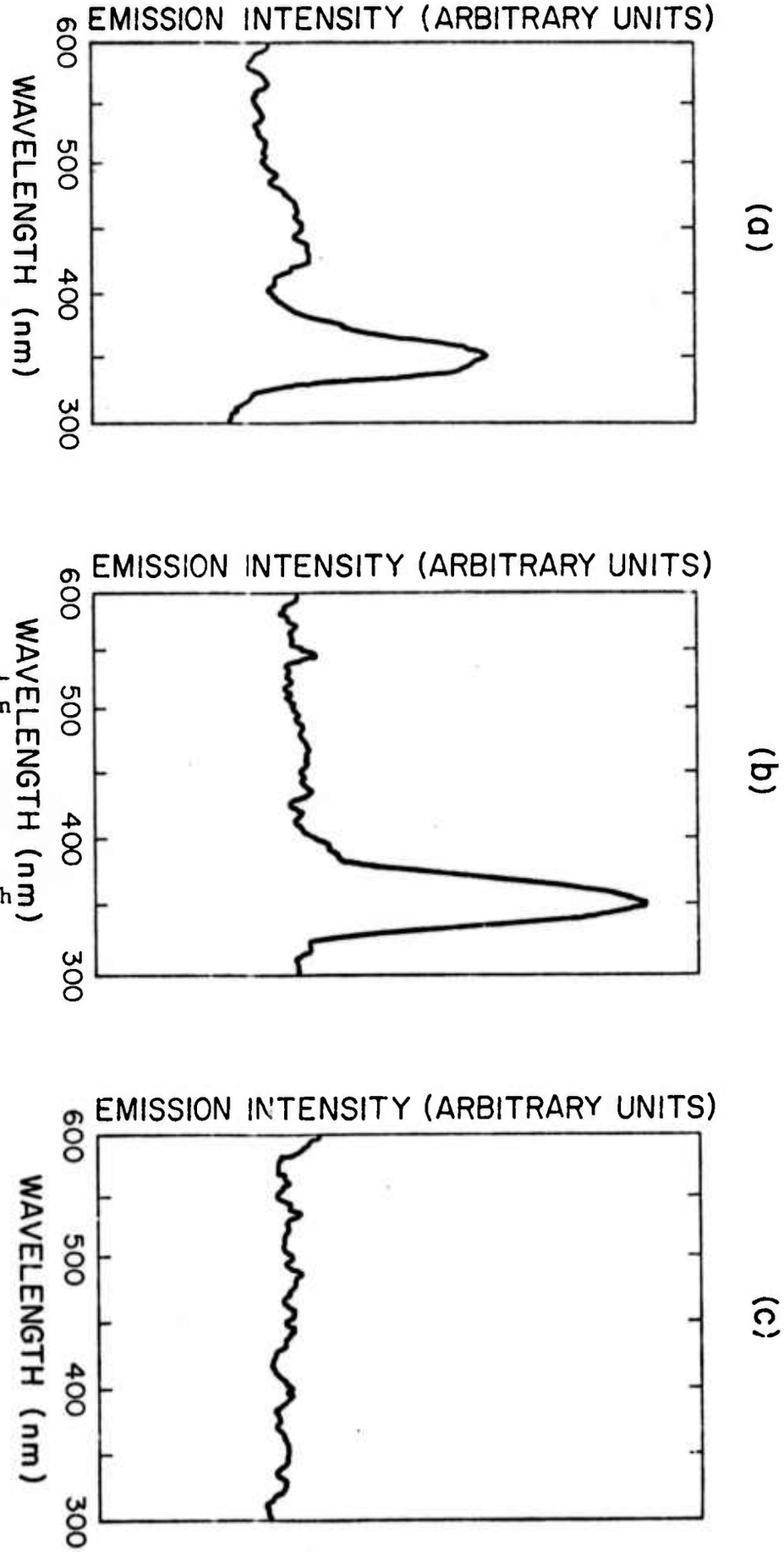

Fig. 8 Emission spectra of thin films of CsI under different thermal treatments
(a) RTAC emission of sample without irradiation at LNT
(b) RTAC emission of sample with irradiation at LNT
(c) RTBC emission of sample which previously showed RTAC luminescence and then annealed again.
All excitations at 235nm.

a day. Measurements at room temperature after annealing showed no emission as shown in Rig. 8c for all excitations either in the excitonic or fundamental absorption edge.

5. Discussion

The two exciton peaks at 220nm and 205nm are well resolved at RTBC and RTAC for the thin films of CsI while at LNT the 1st exciton band (220nm) sharpens and shifts to shorter wavelength 215nm. The fact that this 220nm band did not split into two bands at LNT for all thin samples as observed by others is undoubtedly due to sample preparation. The 205nm band though sharpened at LNT but did not change position. This agrees with what other authors[24,25,34] have observed for thin films of CsI.

Only the first exciton band (220nm) was resolvable at RTBC and RTAC in the bulk single crystals of CsI because of its high absorption. At LNT, the 220nm band splits into two bands peaking at 218 and 215nm while the second exciton band now appears at 205nm. The observed splitting is less than the predicted halogen atom minimum doublet splitting of 0.99ev for the iodides[35]. The difference between the calculated and observed splitting of the halogen atom doublet is probably due to configuration interaction[34,35].

The position of the first exciton band (216 $\pm$ 2nm) in CsI agreed with that calculated by Martienssen[36] at liquid nitrogen temperatures (LNT).

At RTBC there was no emission from all the samples for all excitations either in the excitonic region of the fundamental absorption edge. This result does not agree with Morgenshtern's results[28] since he observed emission at RTBC from his measurements on monocrystal of "pure" CsI. They probably contained trace impurities whose importance as a source of luminescence was not appreciated at the time. Other authors[27,29,30] observed RTBC emission in pure CsI which had been either plastically deformed or thermally quenched (heat-treated).

The ultra-violet luminescence at 350nm observed at LNT in both thin films and bulk single crystals of pure CsI for excitonic excitations agreed with other authors results[24,28]. That the corresponding excitation spectra peaked at (217-220nm) in the excitonic region (with humps at 235-237nm) supports the contention that this luminescence is due to electron-hole radiative recombinations at some centres created by cooling and irradiation with nonionizing ultra-violet light[21,22]. Edge excitations (235nm) at LNT gave a sharp BL at 425nm for the bulk single crystals while for the thin films excitation at 235nm gave besides a weak BL at 430nm a sharp ultra-violet luminescence at 350nm. Measurements at LNT for excitations at 235nm on thin films (500-2000Å) of pure CsI showed a dependence of the 430nm emission on thickness and thermal treatment. We observed that the 430nm emission becomes more intense the thicker the sample and the more rapid the cooling process from 450°K → 300°K. The origin of the yellow luminescence at 540nm is not understood at this time.

When the sample warms back to room temperature (RTAC), we observed ultra-violet luminescence in the thin films while the bulk single crystal gave both blue (470nm) and yellow (540nm) luminescence for excitation at 235nm. This was not observed at RTBC. This effect might be tentatively explained as a contribution from two centres created by (1) temperature cycling and (2) irradiation at LNT with nonionizing ultra-violet light. Fig. (8) shows that the intensity of the RTAC emission for a sample which had not been irradiated at LNT is less than that of a sample which had been irradiated at LNT. This thus suggests that the center responsible for the RTAC emission is created by temperature cycling (cooling) which is enhanced by irradiation with non-ionizing ultra-violet light at liquid nitrogen temperatures. Also because there is no room temperature emission from a sample which previously showed RTAC emission after it had been annealed for about a day, suggests the association of the

centre responsible for the RTAC emission with structural lattice defects probably of the vacancy type.

In addition to these results, work in a preliminary stage[37] on the EPR of bulk single crystals of pure CsI confirmed the existence of this RTAC luminescence to be due to centres created by temperature cycling (cooling) and irradiation with nonionizing ultra-violet light at LNT.

6. Conclusions

Since the ultra-violet absorption spectra of both thin films and bulk single crystals of pure CsI changes little in intensity and position, we suspected that temperature cycling has little effect on the absorption spectra of our samples.

Also because the excitation spectra of the RTAC emission in both thin films and bulk single crystals of CsI peaked at 235-237nm on the long wavelength side of the first exciton absorption band (220nm) suggests the association of this effect (RTAC emission) with the radiative recombination of holes and electrons at some imperfections or traps created in the sample by cooling and irradiation with nonionizing ultra-violet radiation at low temperatures, liquid nitrogen in this case.

ACKNOWLEDGEMENTS

The authors would like to express their appreciation to Dr. Irwin Schneider and Professor W. A. Harrison for their extremely helpful conversations concerning this work.

7. References

1. C. W. Bates, Jr., Varian Associates Central Research Member #200, (June 1967).
2. R. B. Murray, Int. Symposium on Lumin., Munich (1965).
3. W. S. Rodney, J. Opt. Soc. of America 45, #11, 987, (1955).
4. N. Acquista et al., J. Opt. Soc. of America 43, #11, 977 (1953).
5. C. W. Bates, Jr., Adv. Electronics and Electron Physics 28A, 451 (1969).
6. M. Aegerter et al., Int. Conf. on Scintillators (Munchen, 1965) p.292.
7. K. J. Teegarden, Phys. Rev., 105, #4, 1222 (1957).
8. V. I. Vaidanich, UDC 535 • 34, 459 (Nov. 1964).
9. T. Kamejima et al., J. Phys. Soc. Japan, 32, #3, (March 1972).
10. J. Michael Donahue and K. Teegarden, J. Phys. Chem. Solids 29, 2141 (1968).
11. N. I. Ivanova et al., Opt. and Spectros. 12, 56 (1962).
12. Panova and Shiran, Opt. and Spectros. 32, 55 (1972); 32, 108 (1972).
13. H. Lamatsch et al., Phys. Stat. Solidi (b) 46, 687 (1971).
14. P. N. Ram et al., J. Phys. Chem. Solids 33, p.957 (1972).
15. Ya. A. Valbis, Opt. and Spectros. 21, 106, 957 (1972); I. Parfianovich et al., J. Lumin. 1,2, 657 (1970).
16. J. Pellaux et al., Solid State Comm. 13, p.979 (1973).
17. Yu I Bolko et al., Soviet Phys. Solid State 13, #10 (1971).
18. Irwin Schneider, Physical Review Letters 32, #8 (1974).
19. P. R. Moran, Phys. Rev. 137, #3A, A1016 (1965).
20. F. Seitz, Rev. Mod. Phys. 26, 7 (1954).
21. D. Pooley, Solid State Comm. 3, p.241 (1965); Proc. Phys. Soc. (GB) 87, p.245-262 (1966).
22. H. N. Hersh, J. Phys. Chem. Solids 27, 771 (1966); J. Electrochem. Society 144C, (1971).
23. M. N. Kabler, Phys. Rev. 136, A1296 (1964); R. B. Murray and F. J. Keller, Ibid 137, A942 (1965).

24. H. Lamatsch et al., Phys. Stat. Solidi (b) 48, 311 (1971).

25. D. W. Lynch and A. D. Brothers, Phys. Rev. Letters 21, #10 (1968).

26. H. Lamatsch et al., Phys. Stat. Solidi (b) 49, 311 (1972).

27. C. W. Bates, Jr. et al., Physics Letters A (1975)(to be published); Solid State Comm. (1975)(to be published).

28. Z. L. Morgenshtern, Optics and Spectros. 7, #2, 231 (1959); 8, 5, 672 (1960).

29. S. Masunaga et al., J. Phys. Soc. Japan 21, 4, 638 (1966).

30. T. Towyama et al., J. Phys. Soc. Japan 25, 4, 1133 (1968); Physics Letters 31A, 4, 206 (1970).

31. L. D. Johnson and J. A. Pask, J. Amer. Ceramic Soc. 47, #9, 437 (1964); A. A. Urusovskaya et al., Soviet Phys. Cryst. (USA) 11, #2, 245 (1966).

32. A. L. N. Sterels et al., Philips Res. Repts. 29, 340 (1974); L. Holland, "Vacuum Deposition of Thin Films" Wiley N. Y. (1956).

33. Akinola Salau and C. W. Bates, Jr., (unpublished results).

34. K. Teegarden and G. Baldini, Phys. Rev. 155, #3, 896 (1967); Eby et al., Phys. Rev. 116, #5, 1099 (1959).

35. Knox and Inchauspe, Phys. Rev. 116, #5, 1093 (1959); R. S. Knox, Phys. Rev. 115, 1095 (1959); Mott and Gurney, Ionic Processes in Solids, Dover Publications Inc., N. Y. (1964).

36. W. Martienssen et al., J. Phys. Chem. Solids 2, 257 (1957); Nachr. Akad. Wiss. Gottingen 2a, #11, 257 (1955).

37. C. W. Bates, Jr., D. Leniart, and A. Salau, (unpublished results).

III. SUPERPLASTICITY AND WARM WORKING OF PLAIN HIGH CARBON STEELS

O. D. Sherby

Professor of Materials Science
and Engineering

B. Walser

Research Associate, Department
of Materials Science and Engineering

and

J. C. Shyne

Professor of Materials Science
and Engineering

A. Warm Working and Superplasticity in Ultra High Carbon Steels

Bruno Walser and Oleg D. Sherby

1. Introduction and Summary

Our research has centered on plain carbon steels containing 1.3 to 2.3% carbon (twenty to thirty-five volume percent cementite respectively). These steels would be classified between what is known as high carbon steels (0.8 - 1.1%C) and cast iron (> 1.7%C). Such steels have rarely, if ever, been considered for broad industrial applications. Much of our basic studies at Stanford (on strain-enhanced spheroidization, warm working, strain created vacancies and superplasticity) led us to consider the development of unusual structures in such ultra high carbon steels. During the past year we have developed various TMP (thermal mechanical processing) procedures for developing particulate composites of cementite in ferrite containing ferrite grains finer than one micron in size and cementite particles finer than one tenth of a micron in size. These processing treatments were described in our semi-annual progress report[1]. We have shown that such high carbon steels are superplastic at warm temperatures (over 700% elongation has been achieved)[1,2]. Furthermore, they can be made strong and ductile at room temperature. These results suggest exciting possibilities in the application of inexpensive steels for many new structural applications.

This report describes the results of our work during the past year with special emphasis on the work accomplished since the last progress report. A major portion of our work was centered on obtaining and interpreting the mechanical properties of the steels at elevated temperature (600 - 850°C). Tests were performed in tension as well as in compression. Some metallographic studies were also performed. In addition, the room temperature properties of the ultra high carbon steels were studied and assessed. We present below an outline of our report. This is then followed by a summary of our findings

In the first portion of our report we illustrate the problems associated with determining strain rate sensitivity exponents for our superplastic materials. Since grain size is an important factor in determining the flow stress of superplastic materials ($\sigma \propto L^{1.25}$), the grain growth that occurs during plastic flow needs to be taken into account. We developed a scheme (Figure 2) wherein the material is deformed first to a large strain to obtain a steady state structure. Change-in-strain-rate tests were then performed over small strain increments with the assumption that little grain growth occurred during the multiple strain-rate-change tests. Such tests lead to stress-strain rate relations of the type given in Figure 4 revealing the high strain rate sensitivity observed at low strain rates ($m \simeq 0.5$).

Strain rate-stress relations for the ultra high carbon steels were determined over the temperature range 600 to 850°C. Typical behavior is shown for a 1.6%C steel at 700°C (α+Fe_3C) and 770°C (γ + Fe_3C) in Figure 8. The steel exhibits superplastic characteristics at low strain rates in both the ferrite and austenite range of temperatures. The strain rate range of superplastic behavior is wider in the (α + Fe_3C) range than in the (γ + Fe_3C) range. We attribute this to the presence of strong cementite in the alpha range which makes plastic flow by normal slip processes more difficult thus extending the range of superplastic behavior. This new information suggests the importance of controlling the relative strength of phases in two phase superplastic alloys as a means of optimizing the range of high strain rate sensitivity.

The influence of carbon content on the strengths of the ultra high carbon steels is shown in Figure 11. The superplastic steels are shown to have about the strength of pure iron at 700°C and low strain rates. A high purity carbon alloy is shown for comparison in the same figure. We made the unexpected discovery that high purity Fe-C alloys cannot be made superplastic. As shown in Figure 11, the m values for the pure 1.6%C alloy is low ($m \simeq 0.15$) and the accompanying ductility was normal (50-100% elongation); electron and optical microscopy revealed that the pure ultra high carbon iron alloys could not be made fine grained. These results indicate the importance of impurities in retarding and controlling grain

size and grain growth (manganese and silicon are the principal impurities in our ultra high carbon steels).

We performed tensile tests on the ultra high carbon steels in the as-cast state. Such tests revealed, as expected, high strength at warm temperatures (Figure 13). A remarkable feature was that the as-cast material exhibited reasonable tensile ductility (40-50% elongation to fracture). This result indicates that cast ultra high carbon steels are forgiving materials at warm and high temperatures; that is, they can be deformed extensively with little fear of premature cracking or failure especially when deformed in a non-tensile mode. These results are in agreement with the ease of forming (over a wide range of temperatures) we have experienced in making wrought products from our original castings.

The ductility of our fine grained ultra high carbon steels is high at high temperature. Using a new tensile test setup (Figure 1) we were able to deform a 1.6%C steel to 750% elongation at 650°C. High tensile ductility is even obtainable at high strain rates in the gamma plus cementite range. Figure 15 illustrates a sample of 1.6%C steel deformed to 165% elongation at 800°C and $\dot{\varepsilon}$ = 100% per minute. This result, together with other data (Figure 16), indicates the wide range of temperatures and strain rates over which superplastic-like behavior is observed.

The true stress-true strain curves obtained at high temperature exhibit a high degree of strain hardening. Typical curves are shown in Figure 17. On the same graph we illustrate the stress-strain curves expected if no strain hardening occurred, given as dotted lines; the flow stress is shown to decrease with strain because the strain rate decreases in a constant crosshead speed tensile test. We have attributed the strain hardening observed to grain growth. As a thinking exercise we have estimated the amount of grain growth expected based on the increase in flow stress with straining using the phenomenological equation for superplastic flow, $\dot{\varepsilon} = K\sigma^2 L^{-p}$ where p is the grain size exponent. Taking p as 2.5 (typical of that observed for most superplastic alloys) we predict that the grain size will increase by a factor of about five after 300% elongation (Figure 18). Metallographic studies indicate that grain growth of this order is observed (Figure 20).

Compression tests were performed at elevated temperature. Such tests have the advantage that small samples can be used and furthermore they are relatively easy to perform. Tests were done both in the ferrite and in the austenite range. Activation energies for plastic flow were calculated (Table 3). In general, the

activation energies obtained were as expected. At low stresses, in the superplastic range, Q was found about equal to the value for grain boundary diffusion (Q_{gb} = 40 kcal per mole). At high stresses, in the slip creep range, Q was found equal to the value for lattice diffusion (Q_L = 65 kcal per mole).

Mechanical property studies were made on the three ultra high carbon steels at room temperature. Three types of measurements were used to characterize the steels, namely, tensile, hardness and bend tests. The tensile tests revealed that it was possible to obtain strong and ductile material with the 1.3%C steel when in fine spheroidized form (Table 4-1). With increasing carbon additions the yield strength was not increased, however, and the ductility decreased. Much more work is needed to understand the factors influencing the low temperature tensile properties of ultra high carbon steels. We have shown that heat treatment of the fine spheroidized steels can lead to wide variation in hardness. Figure 28 illustrates that hardnesses greater than Rc = 65 are readily achieved by heating a warm-rolled sample to 750°C followed by quenching. Annealing after quenching leads to a gradual decrease in hardness with increasing annealing temperature. As part of our study of the room temperature properties we built a special setup for testing the ultra high carbon steel sheet by bend tests. The objective here was to accomplish tests, east to perform, for evaluation of ductility and strength on simple configuration samples. This approach was especially useful for our studies because of the difficulty of machining the ultrahigh carbon steels especially when in the very hard state.

To summarize, our research in the past six months has centered on identifying the important variables influencing superplastic flow of our ultrahigh carbon steels. In addition, some preliminary studies were made on the strength and ductility of our steels at room temperature as influenced by processing history and heat treatment. The results obtained indicate many exciting possibilities in the development of unusual microstructures and in the utilization of such materials for high strength structural applications. Considerable additional work is needed, however, to assess the importance of composition and processing variables in optimizing the properties of the ultrahigh carbon steels for room temperature applications.

2. High Temperature Properties

(1) High Temperature Tests: Tension

a) Experimental Procedure (description and critical evaluation)

The high temperature tests were done in two different experimental set-ups attached to an Instron machine. The first consisted mainly of a Marshall-furnace and a sealed steel tube that permitted testing in a protective atmosphere. The constant temperature zone was about 1.5 inches and due to the relative non-uniform temperature distribution the maximum elongations achievable were never more than 500% for a 1/2" gage length sample. The elongations to fracture are therefore not absolute values but do give a relative measure of ductility. The results, however, can be used to obtain information about the influence of different warm working conditions on the elongation to fracture at warm temperatures. The need for a new testing apparatus led to the development of the following design. We chose a dual-elliptical reflector infrared furnace as the heating element. The advantage of such a furnace is: 1) High specimen heating rates can be accomplished. 2) Specimen temperature may be accurately controlled or programmed with proportional power temperature controller. 3) External thermal radiation minimized the internal cooling problems; that is, one can work closely with equipment without discomfort. 4) The furnace is very compact, lightweight and therefore easy to attach to the Instron. 5) The heating elements are inexpensive and can be easily replaced.

In order to maintain an inert or reducing atmosphere during the test a quartz tube was used as the containment for the specimen. The upper part was sealed with a stationary O-ring, whereas the lower moving part was sealed by an elastic rubber tube. All metallic parts exposed to high temperature were machined either from inconel or stainless steel. The upper seal was cooled in order to protect the load cell. Figure 1 shows the test apparatus.

A good temperature distribution along the sample length was achieved, by trial and error, using shields (Ni-foil) on the quartz tube. It is possible to reduce the temperature gradient to within ± 0.5% of the desired temperature over a length of more than 3 inches. The available Instron machine allowed only constant crosshead speed tests. Two different testing schemes were developed: i) change-in-strain-rate tests and ii) constant crosshead speed (decreasing true strain rate) tests to fracture.

i) Change-in-strain-rate tests

The tests were usually performed on a one inch gage length sample (described in section on room temperature testing). Prior to testing the sample was soaked

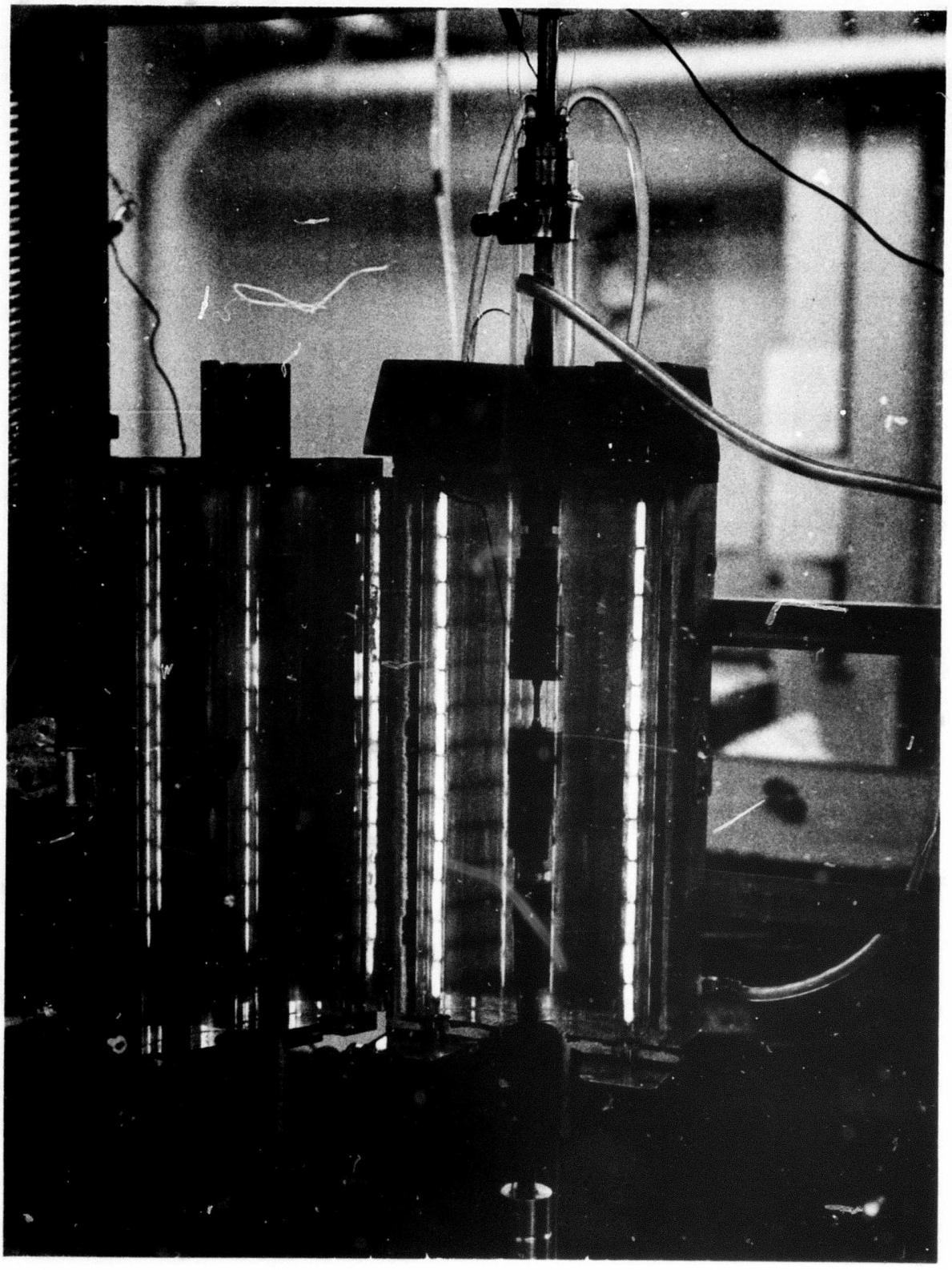

Figure 1. Photograph of the new tension test setup for study of warm temperature properties of ultra high carbon steels. Heating is done with a dual elliptical furnace and the sample is contained in a protective atmosphere within the quartz tube. 41-a

at the test temperature for about 45 minutes. There exists considerable controversy on the usefulness and interpretation of change-in-strain-rate tests in the literature[3]. We used therefore two different approaches in our testing scheme to obtain some insight on possible differences in the measured results.

The first approach was the following: The sample is run at a constant crosshead speed to a strain of about 0.2. The crosshead speed is then either decreased or increased and run at this rate to an additional large strain of 0.1. Again, the crosshead speed is changed and the test continued to an additional strain of 0.1. In order to obtain the true stress-true strain behavior and the corresponding strain rate sensitivity exponents (in the eq. $\sigma = k \cdot \dot{\varepsilon}^m$) either the maximum of the observed stresses or (if the stress was still increasing as in the case of slow crosshead speeds) the final stress was determined. The corresponding true strain rates were calculated. This scheme works only when a constant structure is maintained. In the case of a superplastic behaving material this assumption is not generally true. It is a fact[3-4] that during deformation of superplastic materials grain growth occurs. This leads to strain hardening since the flow stress is proportional to the grain size L ($\sigma \propto L^{1 \text{ or } 1.5}$)[5]. The shape of the stress-strain curve is more strongly influenced by grain growth at low strain rates (long times) than at high strain rates (short times). Consequently, when the strain rate is suddenly decreased to a low rate it is difficult to determine the proper choice of flow stress at the new rate for determination of the m value (the new instantaneous flow stress is difficult to determine and the steady state flow stress is achieved only after large strains by which point grain growth has occurred). Tension tests at elevated temperature show that maximum flow stresses are not achieved until about 20-30% deformation (depends on the crosshead speed).

The experimental results produced by a relatively simple scheme of change-in-strain-rate tests have to be considered with caution, especially if they were measured in the early stages of deformation. These considerations led to the development of a second approach for change-in-strain-rate testing. After reaching the test temperature, a sample is pulled at a low strain rate to about 20-30% deformation to establish a more or less constant structure. Then the crosshead speed is changed repeatedly with only a small increment of strain at each change. Figure 2 represents a typical curve for this type of change-in-strain-rate test. An expanded portion of Figure 2 is shown in Figure 3 and illustrates how the m values depend on the way they are determined. One can assume that the structure will be constant after

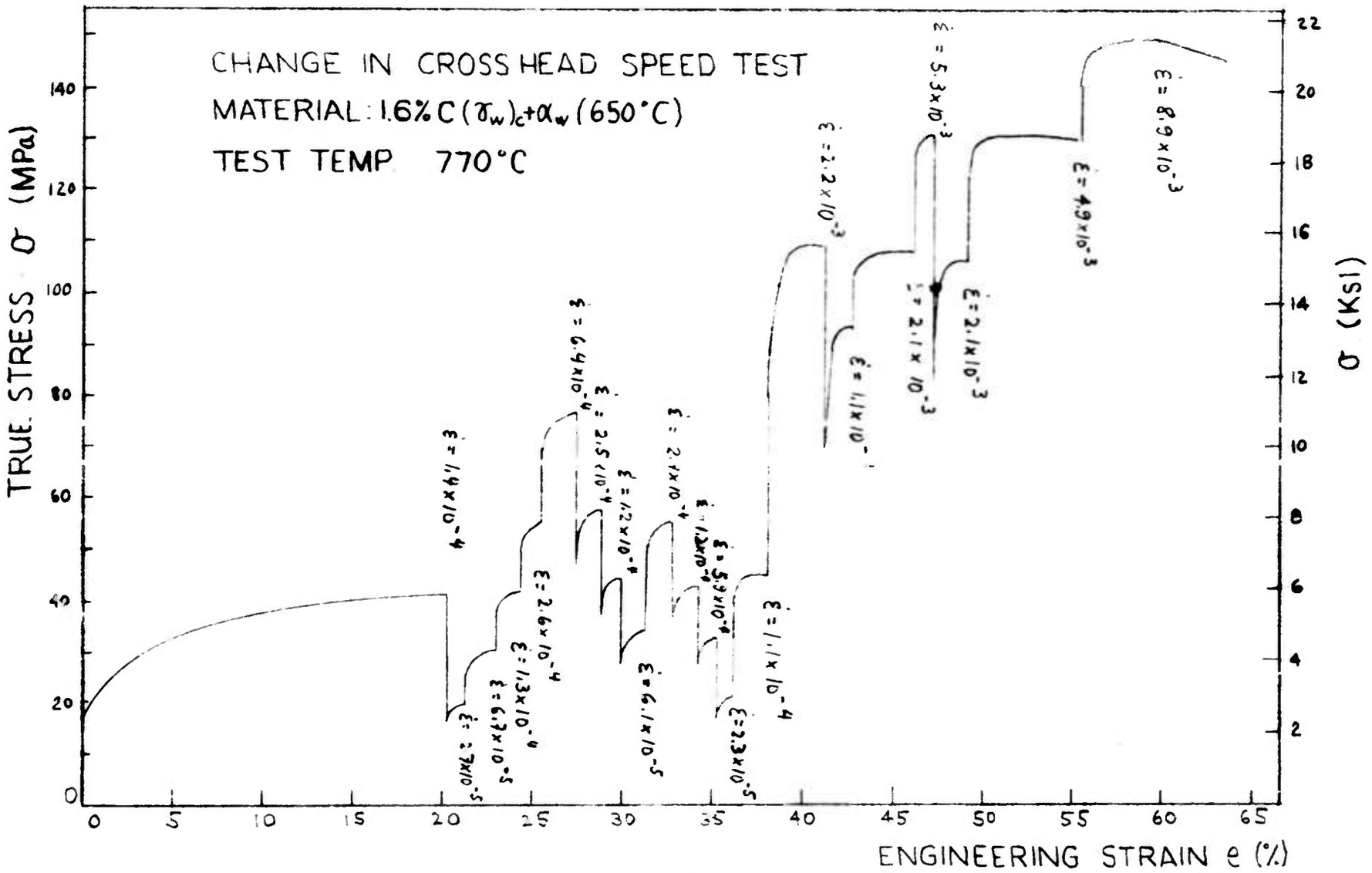

Figure 2. Change-in-strain-rate tests performed on a 1.6%C steel in tension at 770°C. The material was prepared in a fine spheroidized state by rolling during gamma cooling and additional rolling at 650°C. Such tests on a single sample permit plotting the flow stress as a function of the strain rate as shown in Figure 4.

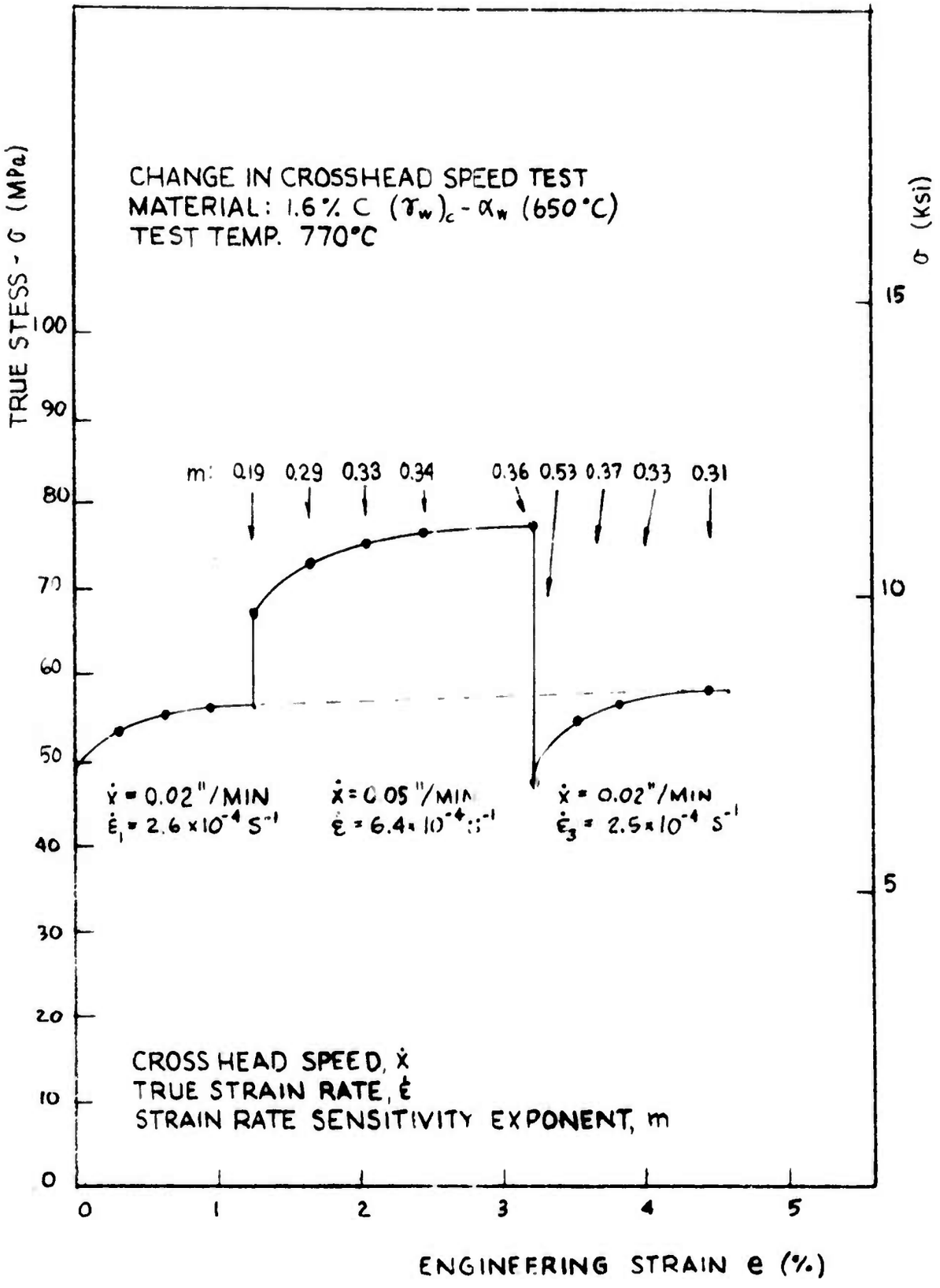

Figure 3. Change-in-strain-rate tests indicating the transients observed during deformation of the 1.6%C steel at 770°C. It is not certain whether the transients are due to unusual sample behavior or due to unusual machine stiffness response.

a change from a low to a high strain rate (Figure 3, $\dot{\varepsilon}_1 = 2 \times 10^{-4}\ s^{-1} \rightarrow \dot{\varepsilon}_2 = 6.4 \times 10^{-4}\ s^{-1}$). But if the instantaneous yield stress is used to evaluate m ($m = \frac{\log \sigma_2/\sigma_1}{\log \dot{\varepsilon}_2/\dot{\varepsilon}_1}$), too low values of m are observed. On the other hand, upon a decrease in strain rate too high values of m will be observed (Figure 3). It is not at all clear, however, if the transient after a change in strain rate is a real phenomenon. The gradual change may be due to the stiffness response of the testing machine. It is therefore uncertain if the observed behavior is a true material phenomenon or only a characteristic of the set-up used. In order to get statistically reliable values for m the test should include several increasing and decreasing changes in strain rate. The mean value of the measured stresses and strain rates at the end of each change probably yields the most reliable value for m. Grain growth will occur during the strain rate change tests even after the sample is first deformed to 20% strain. We will shortly show, however, that the increase in grain size will not be significant. There is general agreement that the flow stress is proportional to the grain size in the following way: $\sigma\big|_{\dot{\varepsilon}} \propto L^{1 \text{ or } 1.5}$ or, equivalently $\dot{\varepsilon}\big|_{\sigma} \propto L^{-2 \text{ or } -3}$. This permits us to calculate the expected increase in grain size from the increase in flow stress that occurs with plastic straining. Equation (1a) describes the relation for superplastic flow and equation (1b) is the resulting relation which predicts the grain size changes from the change in flow stress.

$$\dot{\varepsilon}_1 = k\, \sigma_1^2\, L_1^p$$
$$\dot{\varepsilon}_2 = k\, \sigma_2^2\, L_2^p \qquad \text{(1a)}$$

or

$$\frac{L_2}{L_1} = \left(\frac{\dot{\varepsilon}_1 \cdot \sigma_2^2}{\dot{\varepsilon}_2 \cdot \sigma_1^2} \right)^{1/p} \qquad \text{(1b)}$$

The actual calculation, choosing the grain size exponent p = 2.5, shows that the grain size increases only 17% for a strain of $\varepsilon = 0.20$ during the change-in-strain-rate tests shown in Figure 2. A similar calculation shows, however, that the grain size from the beginning of the test to the start of the change in strain rate ($\varepsilon = .20$) increased 115%. The example in Figures 2 and 3 yields the true stress-true strain rate behavior shown in Figure 4. The m values are continuously increasing with decreasing strain rate. At low strain rates m exhibits values nearly equal to 0.5.

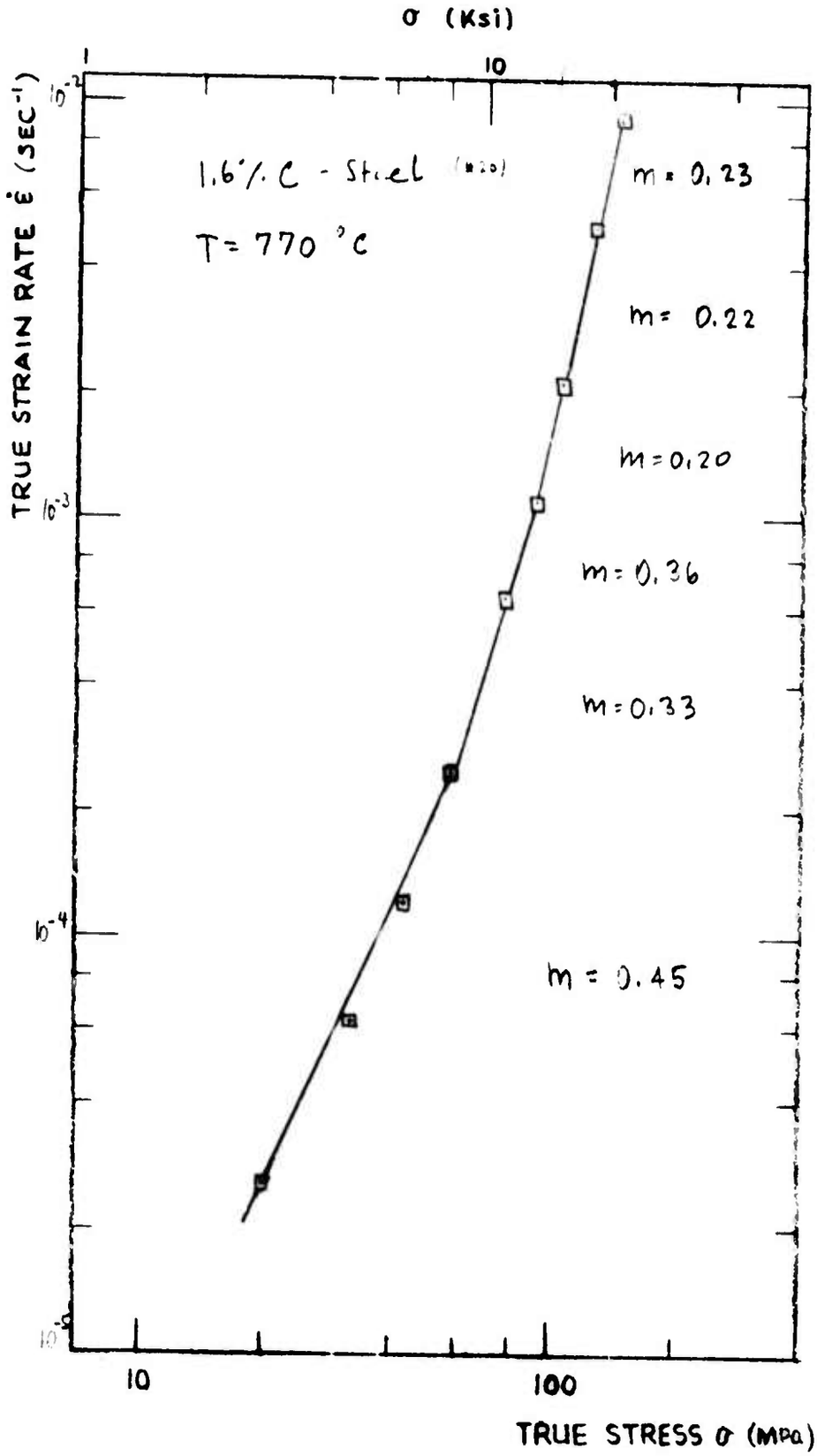

Figure 4. Flow stress-strain rate relationship for a 1.6%C steel tested at 770°C. A high strain-rate sensitivity exponent of 0.45 is observed at strain rates below 2 x 10^{-4}sec^{-1}.

ii) Constant Crosshead Speed Tests to Fracture

The main purpose for this type of test was the measure of the ultimate ductility of our ultra-high carbon steels. The tests were done on samples with 0.5 or 0.25 inch gage length to get maximum elongations in the flat temperature zone. Because of constant crosshead speed the true strain rate was continuously decreasing during the test. Due to grain growth and decreasing strain rate (two competing effects) the interpretation of the true-stress-true strain curve is difficult.

b) Results and Discussion

i) Influence of temperature on change-in-strain-rate tests

We only investigated the 1.6%C steel systematically. The material was warm worked as follows: heated to 1100°C for 60 minutes, continuously rolled during cooling [$(\gamma w)_c$] to a strain of $\varepsilon = 1.4$ then isothermally rolled at 650°C to a additional strain of $\varepsilon = 1.4$. The steel proved to be superplastic and Figure 5 represents the true strain rate-true stress behavior at different temperatures. An obvious difference exists between the tests conducted above and below the A_1 temperature. Steel containing ferrite and cementite (below A_1) is more strain rate sensitive than steel containing austenite plus cementite. From other superplastic systems there is experimental evidence that the strain rate follows qualitatively the relation[6-7]

$$\dot{\varepsilon} = k \cdot \sigma^n \frac{D}{L^p} \qquad (1)$$

where $\dot{\varepsilon}$ = strain rate
σ = flow stress
D = atom mobility
L = grain size
n = stress exponent ($= \frac{1}{m}$)
k,p = material constant

In the slow strain rate region (10^{-5} ~ 10^{-4} s^{-1}) the observed stress exponent for the steel in the austenite plus cementite range is about 2.25, for the steel in the ferrite range about 2. It is interesting to note that the ferritic alloy has low stress exponents up to rather high strain rates (~10^3 sec^{-1}) while the austenitic alloy deviates toward high exponents at relatively low strain rates. On the other hand, the stress exponents are lower in the high strain rate range (10^{-3} - 10^{-2} s^{-1}) for the tests conducted in $\gamma + Fe_3C$ compared to tests conducted in $\alpha + Fe_3C$. Our observations also indicate that forming processes at high deformation rates would require less energy in the $\gamma + Fe_3C$ region than in the

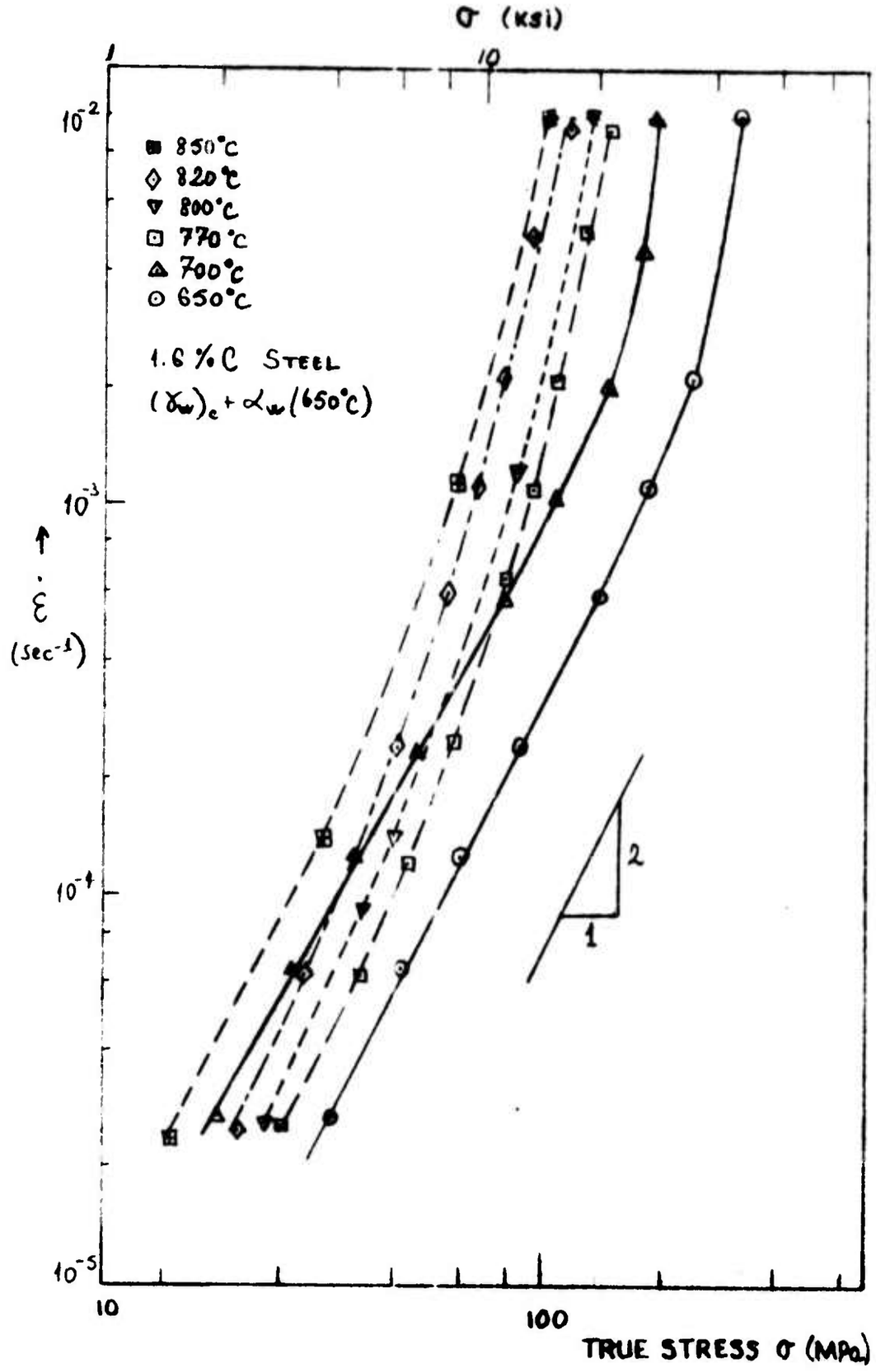

Figure 5. Comparison of the behavior of the 1.6%C steel in the alpha plus cementite range (650-700°C) and the gamma plus cementite range (770-850°C

$\alpha + Fe_3C$ region. At low strain rates, however, steel deformed in the $\alpha + Fe_3C$ range should prove to be more ductile.

Figure 6 shows the measured flow stresses as a function of the test temperature. It is well known that the diffusivity in γ is lower than in α-iron. Therefore at the same stress the strain rate will be lower for the 1.6%C steel in the austenite range than in the ferrite range; in other words, for the same strain rate on should observe a discontinuity at the transformation temperature. This is indeed the case for the 1.6%C steel (Figure 6). Atom mobility is by far the most important factor governing the strength. But it seems that the hardness of the cementite could be an important factor influencing the deformation behavior. Gove and Charles[8] reported hardness values for ferrite, austenite and cementite as a function of temperature. Figure 7 represents a summary of their work. The strength of cementite shows a very strong temperature dependence above about 600°C. At 800°C the hardness values are the same for austenite and cementite. But in the temperature range where α-iron is stable cementite is about 5 to 10 times harder than ferrite. Figure 8 illustrates a plot taken from Figure 5 which permits one to make the following interpretations. At a strain rate of about 5×10^{-3} sec^{-1} the carbide phase plays an important role in determining the strength. Steel in the alpha range is stronger than steel in the gamma range because the ferritic steel contains more cementite and the cementite is harder. Below a strain rate of about 5×10^{-3} sec^{-1} grain boundary sliding becomes more and more the predominant deformation mechanism. At slow strain rates there is enough time available to accommodate the shearing process by either diffusion or dislocation motion. The difference in hardness between matrix and second phase becomes less important. The amount of available interphase and grain boundaries becomes the most important factor. Steel in the austenite range contains more carbon in solid solution and therefore less carbide phase is available. This has two consequences; the amount of interphase boundary and the grain size stabilization effect of the second phase will be reduced. The combination of a decrease in diffusivity and in the amount of second phase yields a lower strain rate sensitivity exponent and a stronger material at low strain rates.

To illustrate the point more clearly Figure 9 represents a schematic sketch showing how two different deformation processes could lead to the observed behavior. In region A a creep mechanism based on dislocation motion (slip creep) will be rate controlling ($n = 5$), whereas in region C grain boundary sliding is the dominant deformation process ($n = 2$). It seems to be true that the difference in hardness

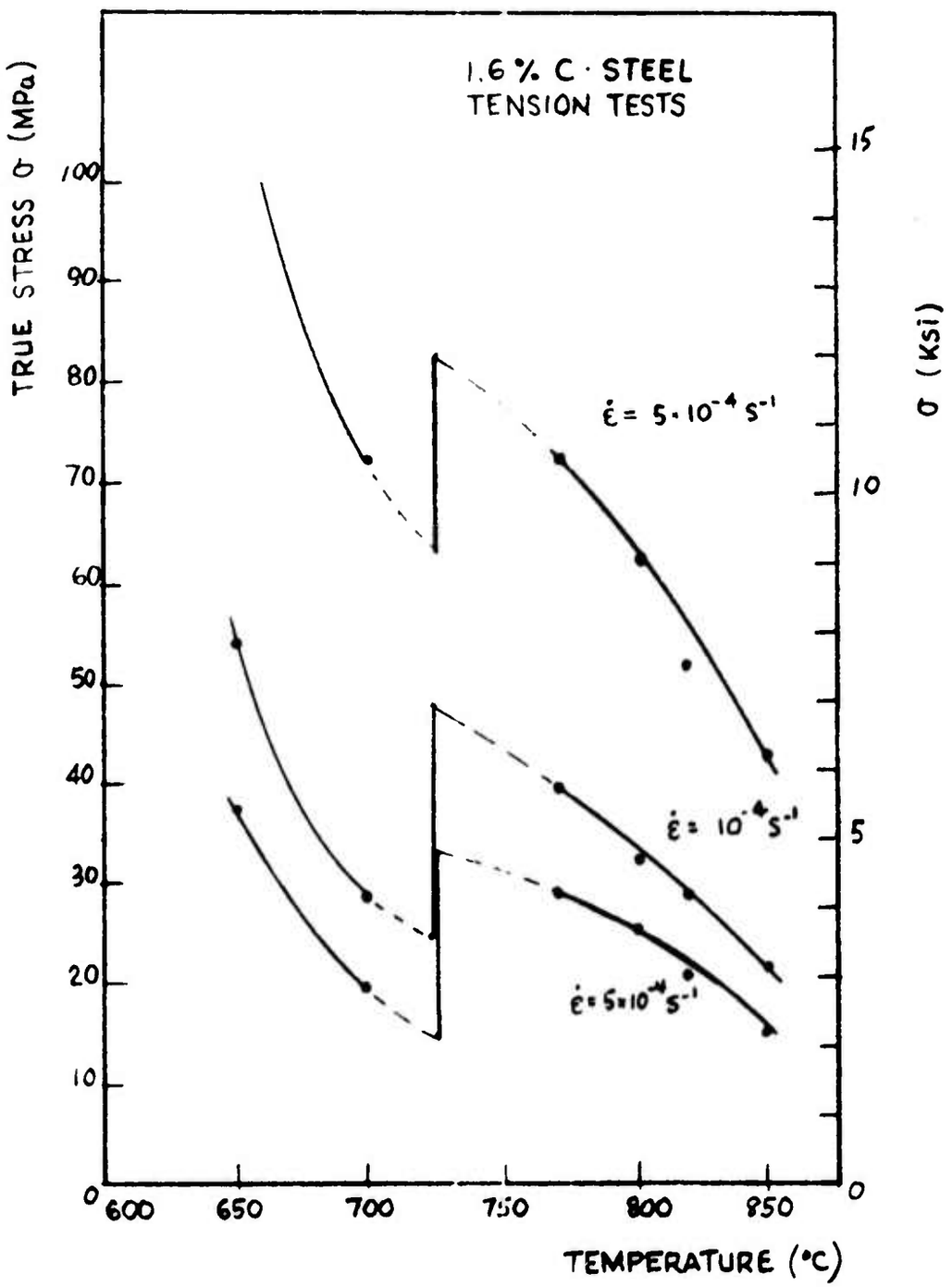

Figure 6. The flow stress of the 1.6%C steel as influenced by temperature in the vicinity of the transformation temperature ($\alpha \rightleftarrows \gamma$).

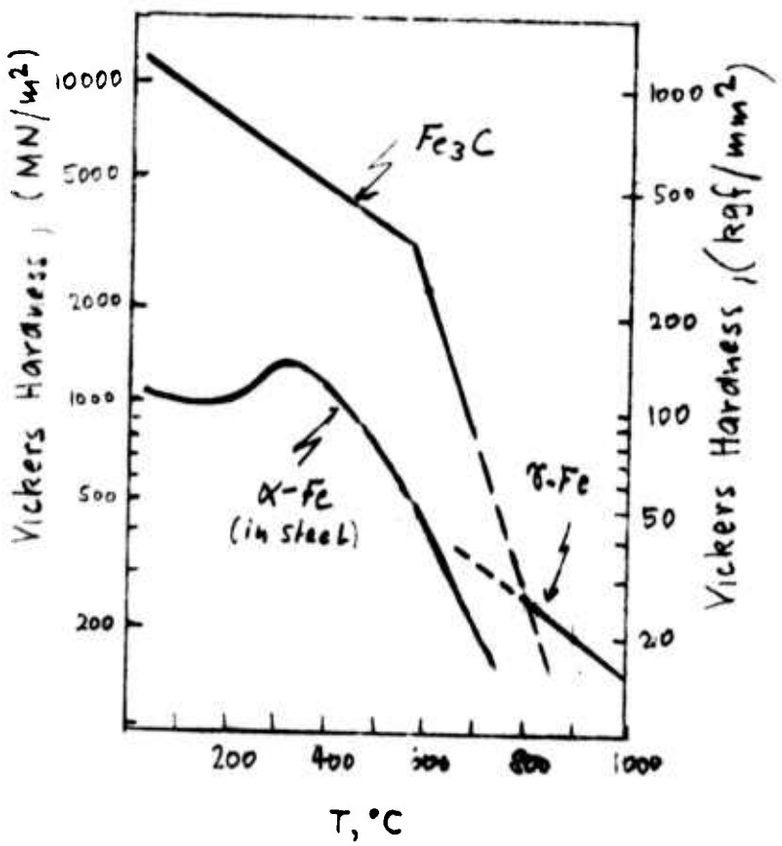

Figure 7. Influence of temperature on the hardness of cementite, ferrite and austenite (after Gove and Charles [8]).

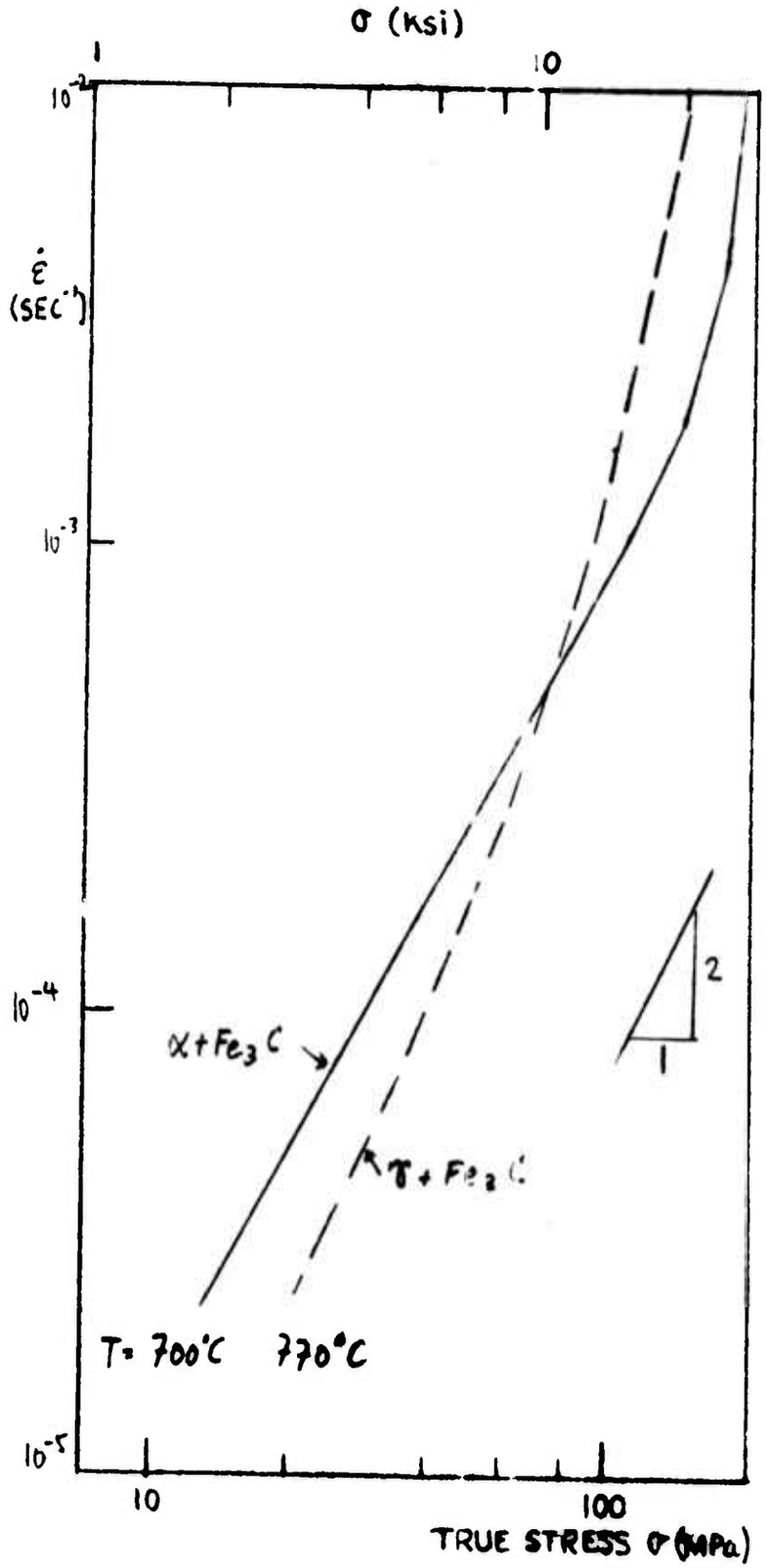

Figure 8. The 1.6%C steel is shown to have a wider range of superplastic behavior in the alpha plus cementite range (700°C) than in the gamma plus cementite range (770°C).

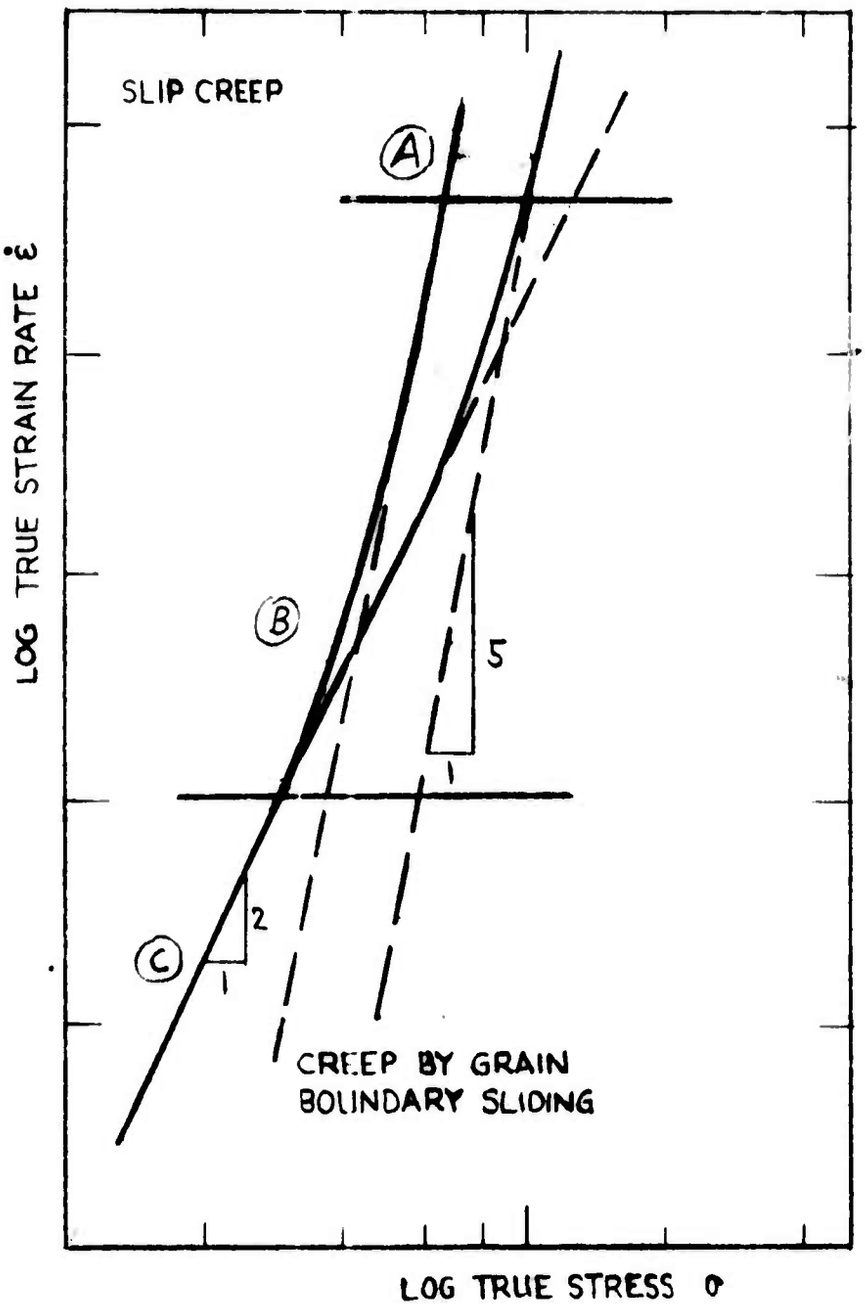

Figure 9. Schematic Diagram illustrating how an increase in the strength of the second phase can lead to increasing the strain rate over which superplastic flow will occur.

of the two phases is not very important in the truly superplastic range (e.g. Ni-based alloys with γ' phase are superplastic). In the slip creep region an increase in strength of the second phase would be expected to shift the stress-strain rate curve markedly towards high flow stresses. Region B represents the change from one rate controlling mechanism to another and the stress exponent should gradually increase from 2 at low strain rates to 5 or 8 at high strain rates (a stress exponent of 8 is observed if the structure remains constant with stress in the slip creep region; also a value of 8 is observed typically in the power law breakdown range). This gradual change in deformation mechanism extends over a range of strain rates and it would seem that in the case of the austenitic steel the material is still in this transition regime. This interpretation of the deformation behavior leads to the following conclusion: more strain rate sensitive material (i.e. to higher strain rates) can be obtained by addition of second phase which is harder than the matrix phase. There will certainly be limits to this idea (for example, a non-deforming second phase) and the experimental confirmation has to be more abundant than presently represented.

It is well known that the diffusivity D and Young's modulus E are two important factors influencing the high temperature deformation behavior of metals[9]. One can compensate for the change in diffusivity and elastic moduli with temperature by dividing the measured strain rates and stresses by the appropriate D and E values. Figure 10 represents the master graph of all the tests done on the 1.6%C steel in tension. As mentioned earlier, carbon addition to austenite increases the atom mobility of iron and the diffusivity is corrected for this fact. The elastic constants for austenite are somewhat uncertain because they are extrapolations of Koster's data for pure iron[10].

The observed scatter in Figure 10 comes from uncertainties in testing and reported values of diffusivity and modulus. Another factor is that the grain boundary diffusion coefficient should be used in the superplastic region. Nevertheless one can conclude that the data shown in Figure 10 correlates quite well giving strong evidence to the importance of introducting the two factor modulus and diffusivity. The largest deviations from a common line are observed in the low strain rate range and it seems that the diffusivity correction for the influence of carbon in austenite is less effective than given in the figure noted in Sherby and Burke[9]. One could speculate that the atom mobility of both iron and carbon in cementite need be considered in the superplastic range of low strain

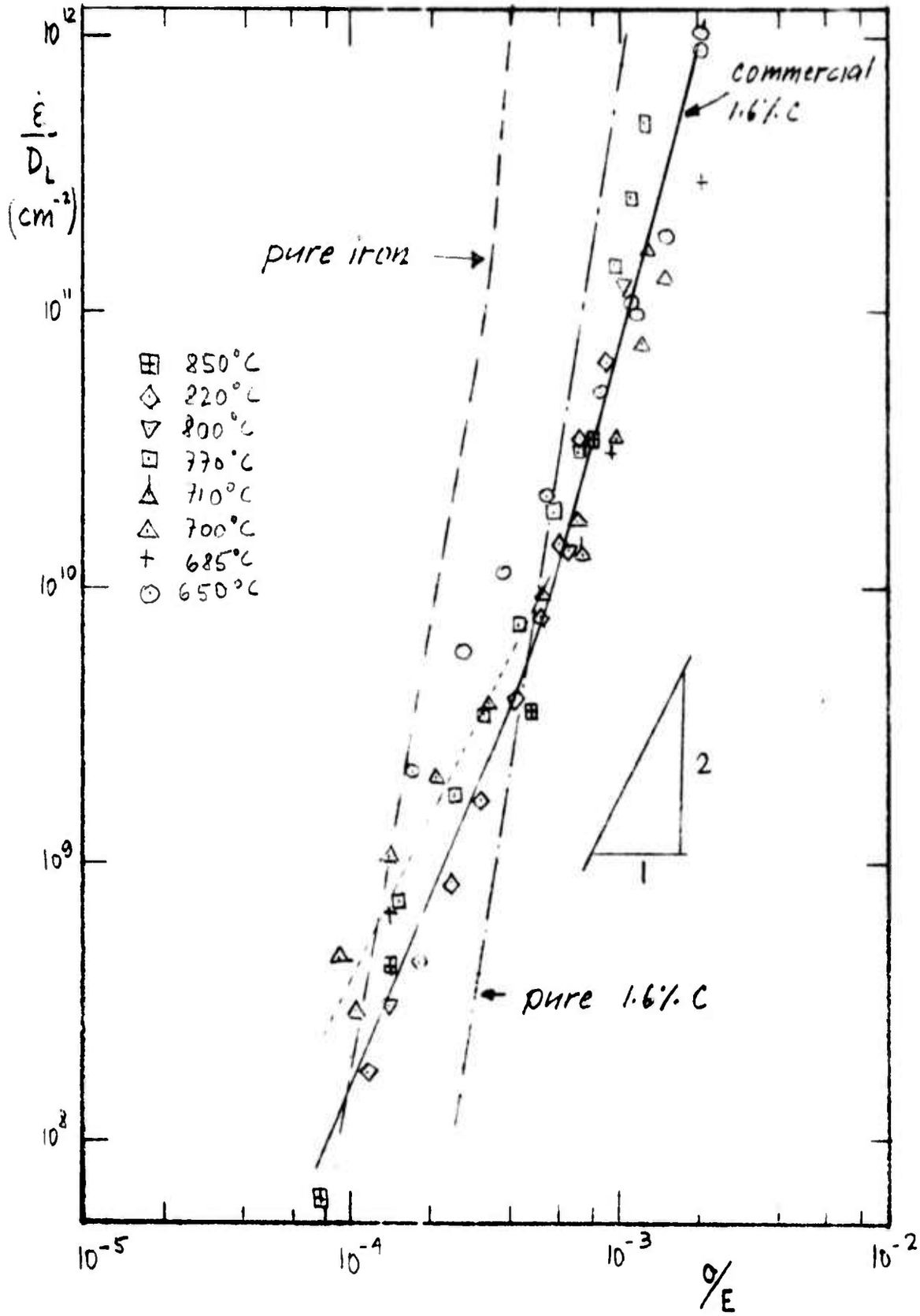

Figure 10. The data given in Figure 5 are replotted as diffusion compensated flow rate as a function of modulus compensated flow stress. Curves for pure alpha iron and for a pure 1.6%C in iron alloy are shown for comparison.

rates.

For comparison Figure 10 also shows the $\frac{\dot{\varepsilon}}{D} - \frac{\sigma}{E}$ curves for pure iron and a high purity 1.6%C steel[11-12]. It is interesting to note that pure iron is weaker than the ultra high carbon steels down to $\frac{\dot{\varepsilon}}{D}$ of about 10^8 cm^{-2} (corresponds to $\dot{\varepsilon} \simeq 5 \times 10^{-5}$ at 700°C). From extrapolation of the available data the ultra high carbon steel will become weaker than pure iron below $\frac{\dot{\varepsilon}}{D} \simeq 10^8$ cm^{-2}. High purity 1.6%C steel behaves quite differently from the commercial alloy and shows a stress exponent n of about 7-8. There are probably several reasons for this behavior. The most important one is the difference in grain size. The Fe-C alloy shows a 5-10 times coarser grain structure than the corresponding carbon steel. It seems that the addition of manganese to the commercial alloy is very beneficial in terms of grain size stabilization during and after rolling and also prevents excessive grain growth during high temperature deformation compared to the iron-carbon alloy. Due to the strengthening effect of the second phase the $\dot{\varepsilon}/D - \sigma/E$ curve for the pure 1.6%C steel is shifted towards high flow stresses. At $\frac{\dot{\varepsilon}}{D} \simeq 10^{10}$ cm^{-2} the curves of the commercial and high purity alloy cross each other: at high strain rates the commercial steel is stronger. There are at least two possible explanations for this observation. One would be based on the difference in grain size: at high strain rates the grain boundaries act as an obstacle for dislocation motion (in the same way as do subgrain boundaries) and the applied flow stress as a function of grain size should follow a relation of the type $\sigma \propto L^{-p}$ (i.e. a Hall-Petch type relation). Another possible explanation for the observed behavior is that solute atoms may play an important role in increasing the strength of the fine grained commercial material at high deformation rates. The movement of dislocations would be made difficult by the presence of solute atmospheres. In this way, then, the commercial grade steel (which contains manganese and silicon as solute additions) may be stronger than the iron-carbon alloy.

We thus see that solute atoms are directly or indirectly responsible for much of the described behavior. Apparently, without any impurities it would not be possible to produce the fine grain size required for superplastic behavior and therefore the observed high m values.

ii) Influence of Carbon Content on High Temperature Behavior

It is well established that an increase in the amount of carbon leads to a change in deformation behavior[13]. We did a preliminary study at 700°C for

the 1.3%C, 1.6%C and 1.9%C steel. Figure 11 represents the true strain rate-true stress behavior of the three steels and includes also tests done on pure iron[11]. The three ultra high carbon steels were produced in the following way:

1.3%C $(\gamma w)_c$ - αw (650°C); $\varepsilon\gamma_c = 1.2$, $\varepsilon\alpha = 1.25$

1.6%C $(\gamma w)_c$ - αw (650°C); $\varepsilon\gamma_c = 1.4$, $\varepsilon\alpha = 1.4$

1.9%C $(\gamma w)_c$ - αs (650°C); $\varepsilon\gamma_c = 2.3$, $\varepsilon\alpha = 1.1$

All three materials saw a final working temperature of 650°C but somewhat different strains in the isothermal α-working step.

At a true strain rate of about 5×10^{-5} sec^{-1} the highest strain rate sensitivity is observed for the 1.6%C steel (1.3%C, m = 0.44, 1.6%C, m = 0.55 and 1.9%C, m = 0.46). At the same strain rate the 1.6%C steel also exhibits the lowest flow stress. The difference in flow stress between the 1.3 and 1.6%C steel can be explained by the difference in carbon content: the 1.6%C steel contains about 25 volume percent cementite against 20 volume percent for the 1.3%C steel. There are less ferrite-cementite boundaries available for interphase shearing in 1.3%C steel and furthermore the reduced amount of second phase can lead to more grain growth. This combination could yield a less ductile material and the difference of about 0.1 in the m value would corroborate this observation. The 1.9%C steel shows a slightly higher m value than the 1.3%C steel but a significantly lower m value than the 1.6%C steel. The measured flow stresses are also higher than for the 1.9%C steel than for the other two materials. This observation could be due to two reasons: first, that the 1.9%C material is not as well spheroidized as the 1.6 and 1.3%C steels because it experienced somewhat less strain during the isothermal α-working step; in addition, investigation of the microstructure of the warm worked steels revealed that the 1.9%C steel in general is more difficult to spheroidize fully. The other reason could be that the optimum amount of carbon for superplastic flow in the measured strain rate range considered lies below 1.9%C. Further studies are needed to clarify this point.

In spite of the various complicating factors that may come into play in explaining our results (Figure 11) it is clear that the amount of carbon, and therefore cementite, influences the flow stress at constant temperature and strain rate. Figure 12 summarizes our results together with results from different investigations[12,13]. Again, the addition of impurities changes the dependency of the flow stress (at 700°C and $\dot{\varepsilon} = 10^{-4}$ $secs^{-1}$) on the carbon content significantly. In the high purity iron-carbon system the increase in cementite phase leads first to an increase and then to a decrease and finally again to an increase in strength.

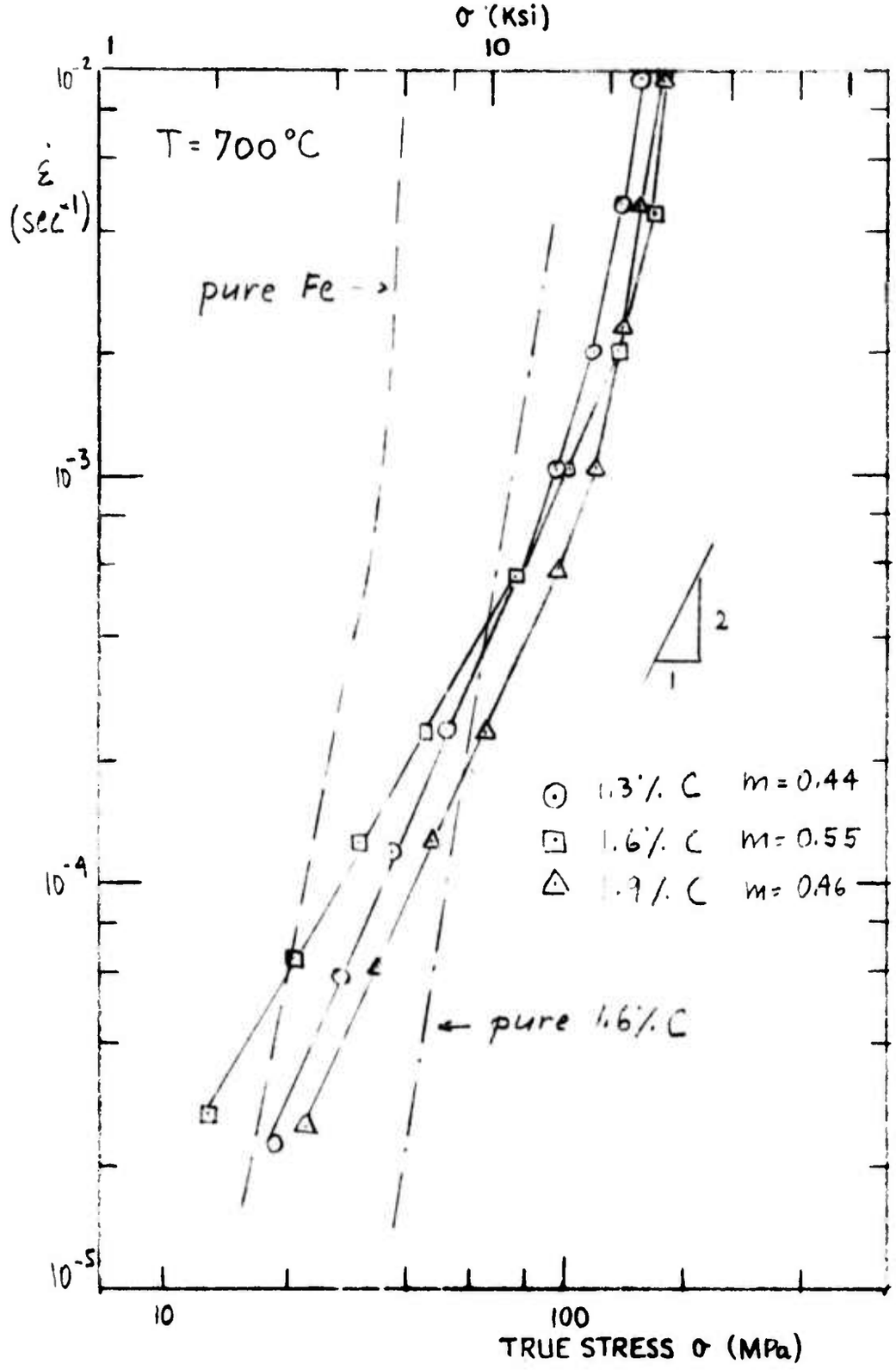

Figure 11. Influence of carbon content on the flow stress-strain rate relation for fine-grained ultrahigh carbon steels. Curves for pure alpha iron and for a pure 1.6%C in iron alloy are shown for comparison. Grain size: 1 to 3μm.

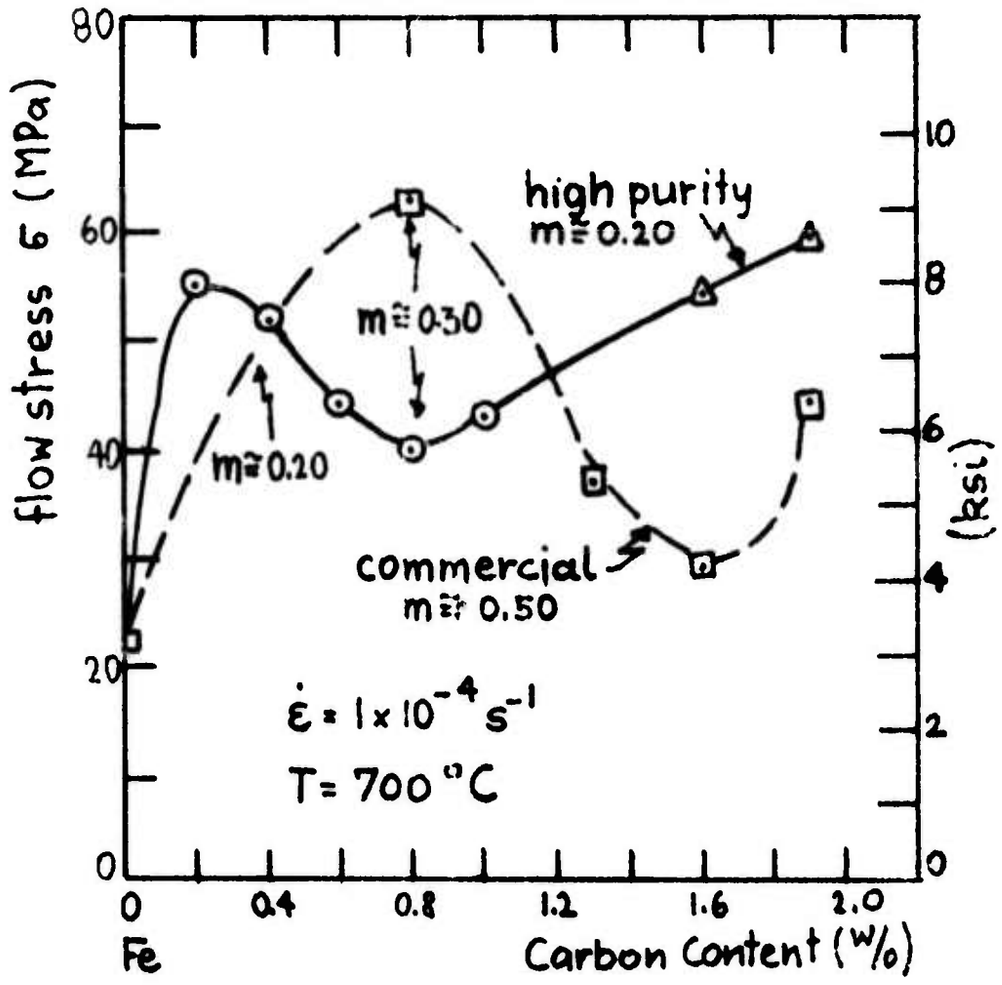

Figure 12. Influence of carbon content on the flow strength of Fe-C steel and Fe-C alloys at 700°C and $\dot{\varepsilon} \simeq 10^{-4}$secs^{-1}.

The minimum occurs at the eutectoid composition where one also measures the highest strain rate sensitivity exponent. This would fit into the accepted view that eutectoid or eutectic systems should show superplastic behavior if fine grained[14]. But more second phase leads surprisingly enough to a decrease in m and therefore to a decrease in superplastic like deformation. The reasons for this behavior are not yet clear and will be explored elsewhere[12].

The iron-carbon-system containing impurities like manganese, silicon, sulfur, phosphorus, behaves quite differently from the pure iron-carbon alloys. The eutectoid composition exhibits the highest flow stress (Figure 12). Nevertheless the measured strain rate sensitivity exponent of 0.3 for the eutectoid composition steel points towards a possible superplastic state. Above 0.8% the increase in second phase by addition of more carbon leads to truly superplastic behavior at low strain rates.

iii) Constant Crosshead Speed Tests to Fracture

The main objective of the tests to fracture was to establish the influence of strain rate, temperature, carbon content and warm working conditions on the high temperature ductility of ultra high carbon steels. The first part describes the results obtained with the first set-up (Marshall furnace) although the testing apparatus did not allow us to achieve the best possible elongations to fracture. All tests were done under the same conditions and give therefore useful comparative information. That is, the data presented do not represent absolute values but allow a relative comparison and give therefore useful information on the behavior one can expect under ideal test conditions. Most of the results were obtained for the 1.6%C steel and the description of the results is concentrated mainly on this material.

To get comparative information a sample of the as-cast material was tested at 650°C at a strain rate of 1% per minute. Figure 13 shows the resulting stress-strain curve together with a stress-strain curve for a fully spheroidized 1.6%C steel. The decrease of about 12 ksi (83 MPa) in flow stress due to a fine spheroidized structure is indeed remarkable and points out the important influence of microstructure on the deformation behavior. The ductility is 10 times higher for the warm worked material than for the as-cast steel. Nevertheless the 43% elongation to fracture for the as-cast steel is quite remarkable and surprising and shows that ultra high carbon steels are inherently ductile (i.e. they are forgiving materials).

The ductility at high temperatures is a strong function of the degree of

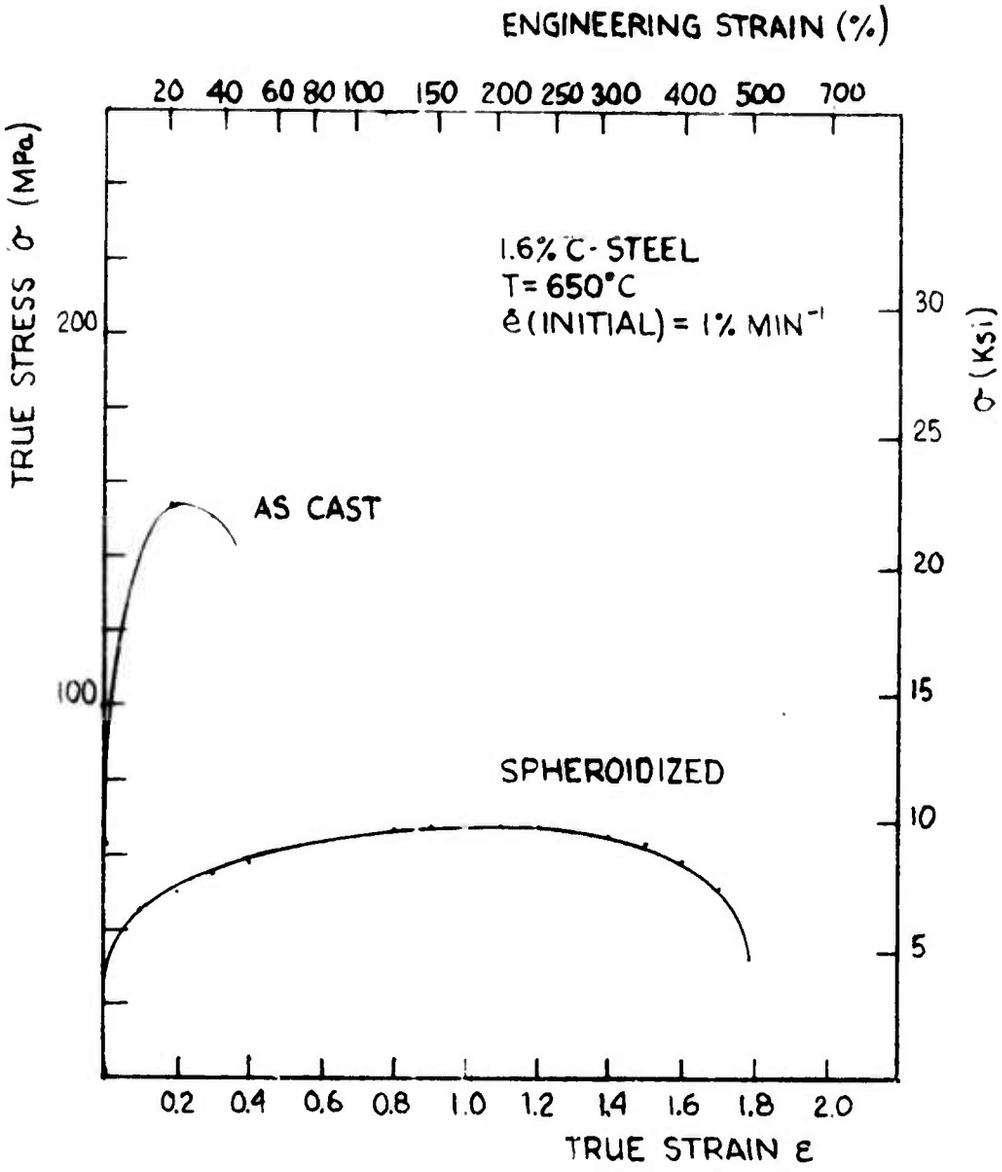

Figure 13. Ture stress-true strain curves for as-cast and finely spheroidized 1.6%C steel at 650°C and $\dot{e}$ = 1% per minute.

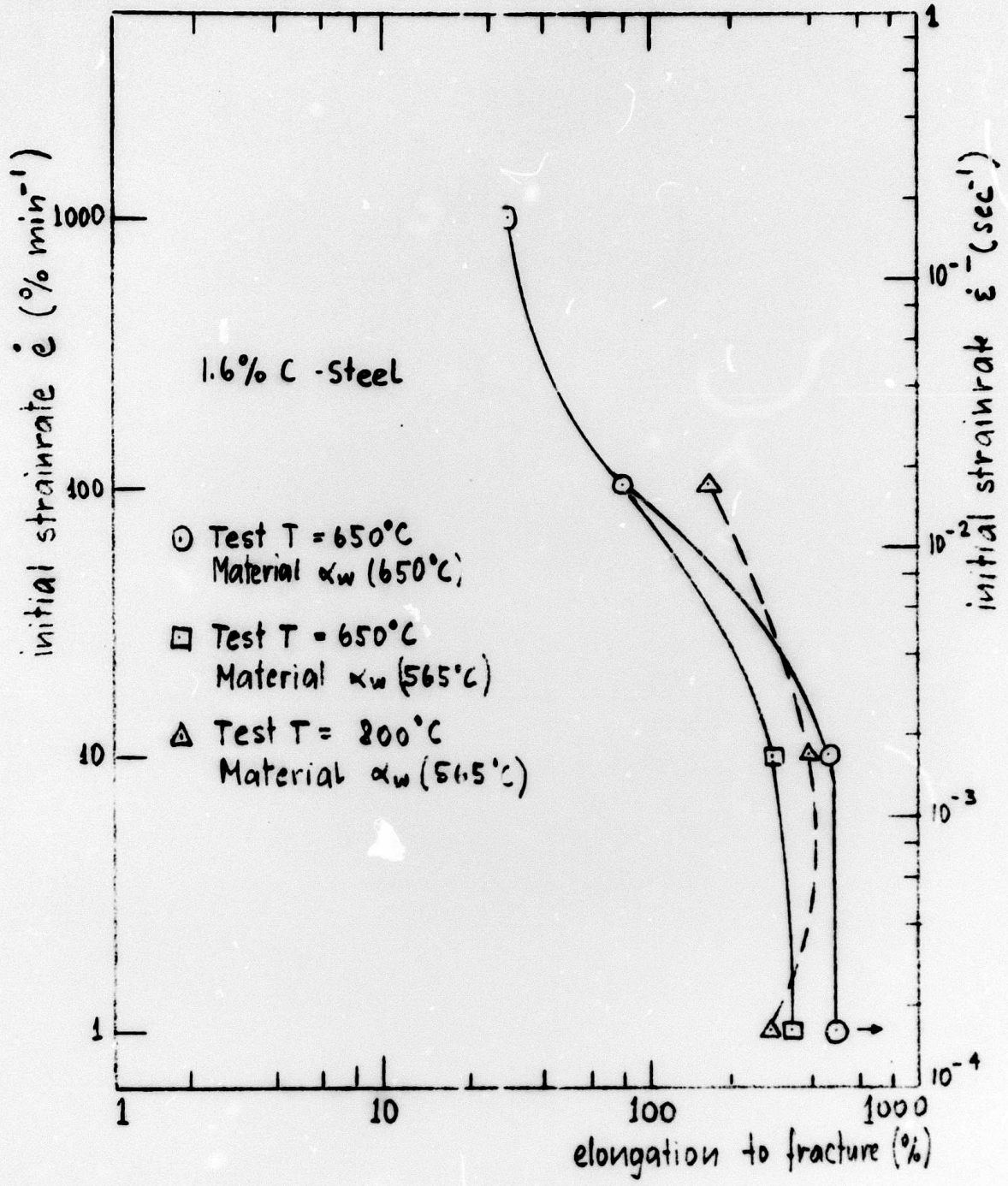

Figure 14. Influence of strain rate on the tensile ductility of a 1.6%C steel at 650 and 800°C.

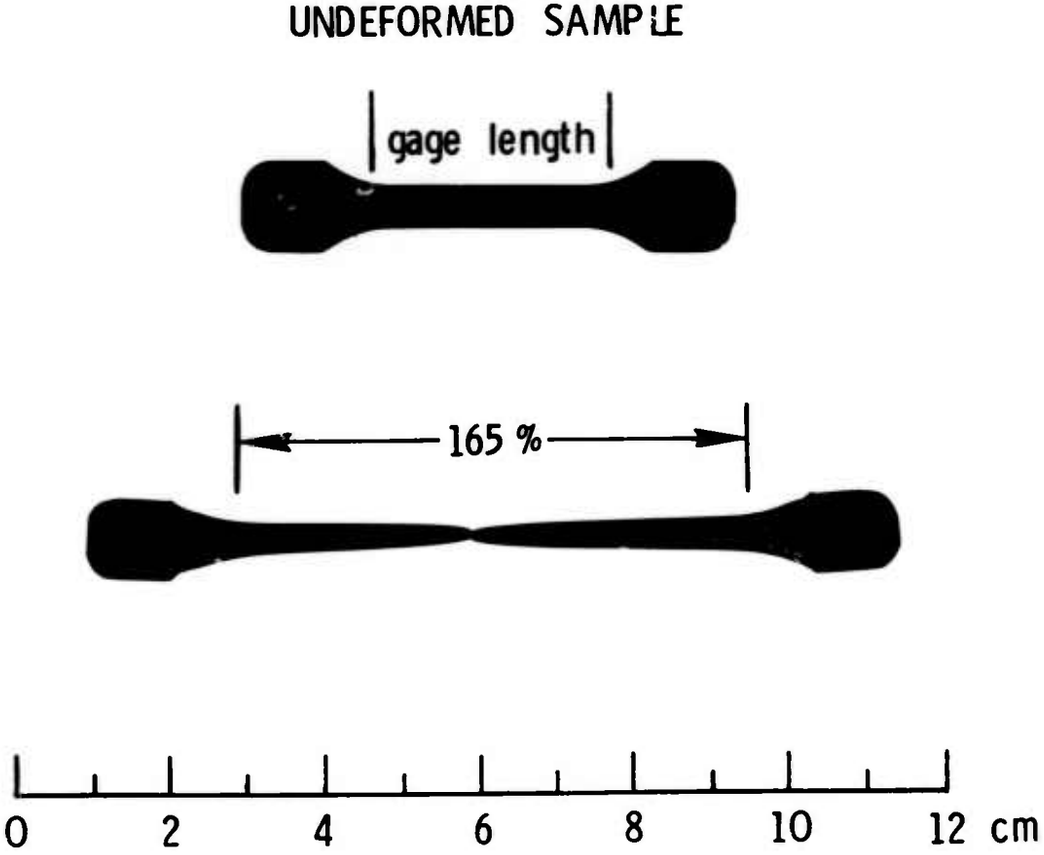

1.6% C- STEEL DEFORMED AT 800 C AT AN ENGINEERING STRAIN RATE OF 100 % PER MINUTE.

Figure 15.

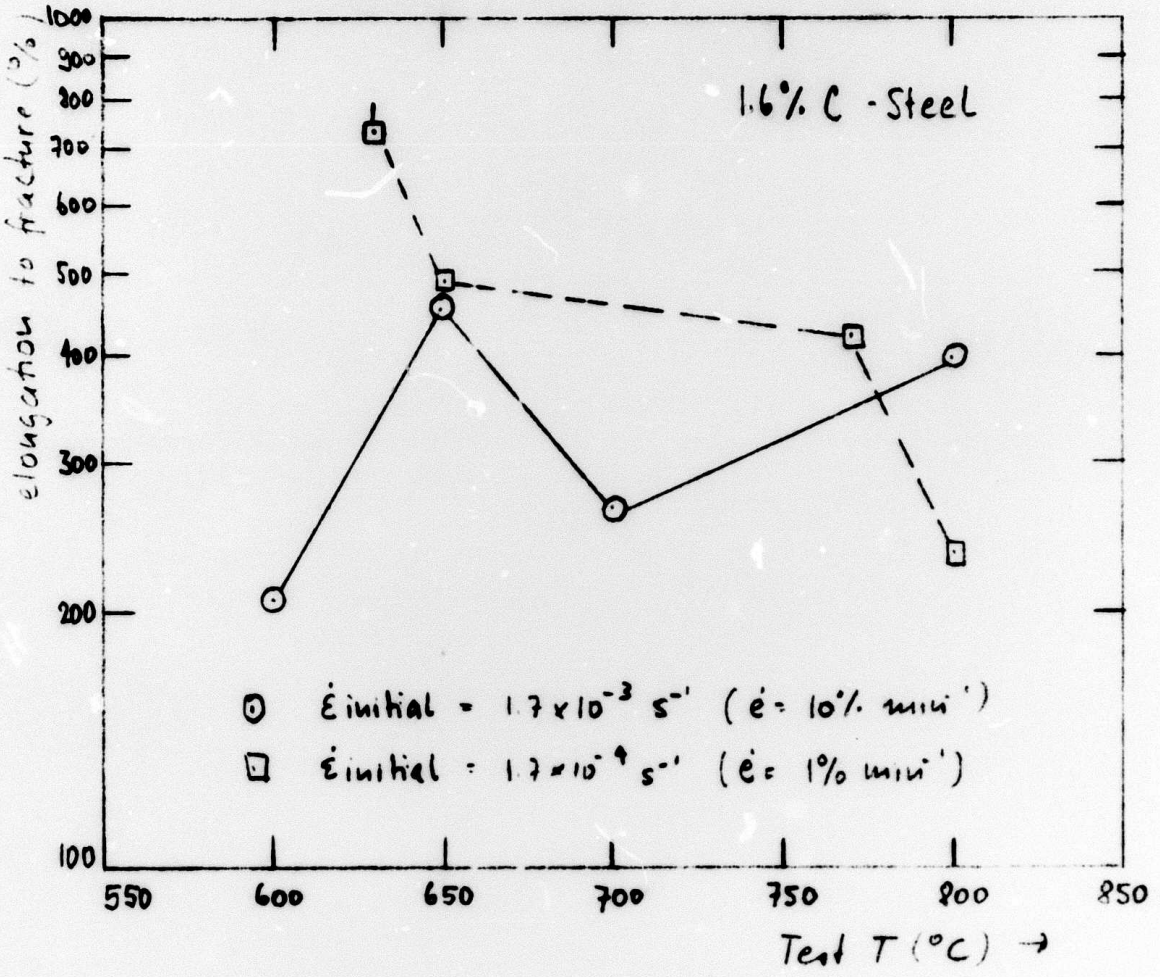

Figure 16. Inlfuence of temperature on the tensile ductility of a 1.6%C steel at two strain rates.

spheroidization, carbide size, and grain size. All those factors are directly influenced by warm working and are a strong function of the warm working strain and temperature. In Figure 14 the elongations to fracture are shown as a function of the initial strain rate. As expected the highest ductilities are observed at the lowest strain rates. The apparent limiting (i.e. maximum) elongations obtained between $\dot{e}$ = 1 and 10% min^{-1} is caused by inhomogeneous temperature distribution along the sample. As shown later, better testing conditions will lead to elongations of over 700 percent. Nevertheless, an obvious influence of the final warm working temperature can be observed for the tests done at 650°C. The material α-worked at 650°C shows higher ductilities than the one worked at 565°C. Although a material processed at a low temperature in the warm working range has a finer structure this will not necessarily be advantageous for deformation at a subsequently higher temperature. Due to high dislocation densities in such a material, a strong driving force exists for grain growth at high testing temperature and this can decrease the ductility. On the other hand, the material rolled at 650°C has a stable structure at the applied testing temperature and grain growth is limited. This observation could imply that it will be important for superplastic forming operations (in the α-region) to choose a material that was previously warm worked at the same or even at a higher temperature. This observation is probably only true for medium to low strain rates, whereas at high strain rates the fine structured material (i.e. material rolled in the low warm working range) could prove to have better ductility.

The material warm worked at 565°C exhibits very good ductility at 800°C and at high strain rates. At a deformation rate of 100% per minute the elongation to fracture was 165% (Figure 15). The fairly low ductility (230%) at the lowest rate of testing (1% per minute) is probably due to grain growth for this long time test at high temperature (Figure 14).

High ductility can be observed over a wide range of temperatures (Figure 16). This means that considerable flexibility in temperature of working is possible in a manufacturing operation (i.e. fluctuations of ±50°C are easily acceptable at a nominal temperature of 700-750°C). Figure 16 includes one point from tests done in the new set-up. Obviously, the measurement of the ductility as a function of temperature is not complete and more tests are required to establish the exact relations. But some preliminary conclusions can be drawn. The highest elongation to fracture are measured in the ferrite plus cementite range at about 650°C. The

ductility decrease that may be expected with increase in temperature in the gamma range may be due to grain growth (the driving force arising from the higher diffusion rates and the decrease in volume percent of cementite).

As explained earlier, the ductility can also be a strong function of the warm working condition that the material experienced. This point needs to be explored further.

All tests done in the new and old testing apparatus are summarized in Table 1.

The influence of the final warm working temperature was already shown in Figure 14 and is verified by the results presented in Table 1. But, it seems that another variable plays an important role in dictating the ductility of these superplastic materials, namely the amount of warm working strain. Materials never α-worked are much less ductile than α-worked materials tested under the same conditions(Table 1, tests 23 and 24). This is even true for testing in the austenite plus cementite range(Table 1, tests 31 and 32). For materials that were never alpha worked higher ductilities are observed in tests in the austenite plus cementite range than in the ferrite plus cementite range. It would be interesting to establish the optimal rolling condition in γw-cooling and (γ + Fe_3C) isothermal working that will yield the best superplastic material for manufacturing processes above the A_1.

The influence of warm working strain on the ductility to fracture is best shown on a 1.9%C steel (Table 1, tests 35 and 36) warm worked at the same temperature but to 5 times more strain. The ductility to fracture is enhanced considerable (from 230% to 335% elongation). A comparison of the ductilities of the three different high carbon steels with each other shows that the 1.3 and 1.6%C steels have about the same ductility. The 1.9%C steel, however, never exhibits the elongations to fracture one would expect based on the amount of second phase. One reason lies in the fact that it was very difficult to spheroidize fully this material; even fairly large amounts of strain were not enough to break up thoroughly the massive cementite structure. There is microscopical evidence of still "chunky" carbides and these could be originated in the original casting. Careful control of casting variables could probably lead to a good 1.9%C steel with exceptionally high formability and good room temperature properties. To date no tests on a 1.9%C steel were done in the austenite plus cementite range. It is possible that the high volume percent cementite present in austenite could lead to a material with higher ductility than in the α + Fe_3C range and these tests will be performed in the near future.

Table 1

Elongations to fracture for the superplastic ultra high carbon steels under different test conditions. (*tests done in new aparatus)

Material	Test T (°C)	Initial Strain-rate $\dot{e}$(%min^{-1})	$\dot{\varepsilon}$ (Sec^{-1})	elongation to fracture (%)	Test No.
1.3%C αw(650) εα=1.7	605	1	1.7×10^{-4}	230*	1
αw(650) εα=1.2	630	0.8	1.3×10^{-4}	700*	2
αw(650) εα=1.2	650	0.8	1.3×10^{-4}	600*	3
αw(650) εα=1.2	650	1	1.7×10^{-4}	480	4
αw(650) εα=1.2	650	1	1.7×10^{-4}	250	5
αw(565) εα=1.7	650	10	1.7×10^{-3}	320*	6
αw(565) εα=0.8	650	100	1.7×10^{-2}	76	7
αw(565) εα=1.7	800	10		140	8
1.6%C αw(565) εα=1.5	600	10	1.7×10^{-3}	207	9
αw(650) εα=1.7	620	0.4	6.7×10^{-5}	489*	10
αw(650) εα=1.7	630	0.8	1.3×10^{-4}	760*	11
αw(650) εα=1.7	650	0.4	6.7×10^{-5}	473*	12
αw(650) εα=1.7	650	1	1.7×10^{-4}	486	13
αw(565) εα=1.0	650	1	1.7×10^{-4}	334	14
as cast	650	1	1.7×10^{-4}	43	15
αw(650) εα=1.7	650	4	6.7×10^{-4}	532*	16
αw(650) εα=1.7	650	10	1.7×10^{-3}	457	17
αw(500) +100 Hrs /500°C εα=1.7	650	10	1.7×10^{-3}	273	18
αw(565) εα=1.0	650	10	1.7×10^{-3}	270	19
αw(700) +100 Hrs /500°C εα=1.3	650	10	1.7×10^{-3}	240	20
αw(650) εα=1.1	650	100	1.7×10^{-2}	78	21
αw(650) εα=1.7	670	0.4	6.7×10^{-5}	361*	22
αw(650) εα=1.1	700	10	1.7×10^{-3}	262	23
no αw	700	10	1.7×10^{-3}	73	24
αw(565) εα=1.0	750	200	3.3×10^{-2}	83	25
αw(650) εα=1.7	770	1	1.7×10^{-4}	421*	26
αw(650) εα=1.8	770	1	1.7×10^{-4}	165*	27
αw(650) εα=1.8	770	10	1.7×10^{-3}	183*	28
αw(650) εα=1.8	770	100	1.7×10^{-2}	89*	29
αw(565) εα=1.5	800	1	1.7×10^{-4}	234	30
αw(565) εα=1.5	800	10	1.7×10^{-3}	397	31
no αw	800	10	1.7×10^{-3}	120*	32
αw(565) εα=1.5	800	100	1.7×10^{-2}	165	33
1.9%C αw(650) εα=0.9 +700°C/30 min	650	1	1.7×10^{-4}	378/380	34
αw(565) εα=0.2	650	1	1.7×10^{-4}	231	35
αw(565) εα=1	650	1	1.7×10^{-4}	334	36
αw(593) εα=1.1	650	1	1.7×10^{-4}	328	37
αw(650) εα=0.9 +700°C/30 min	650	10	1.7×10^{-3}	113	38
αw(650) εα=0.9 +700°C/30 min	700	10	1.7×10^{-3}	222	39

It is interesting to note that very few true stress-true strain curves for superplastic materials are quoted in the literature. The reason for this might be that the interpretation of these curves is not always very obvious. In the following section we present an attempt to explain what information could be gained by a careful analysis of the stress-strain behavior of the superplastic ultra high C steels studied. In an earlier report[15] the influence of prior annealing on the shape of a true stress-true strain was shown. Longer annealing times lead to large grains and therefore higher flow stresses. The more fully annealed material exhibited a low strain hardening rate due to limited grain growth occurring during straining. Under the assumption that no grain growth occurs during a test the true stress-true strain curve for a constant crosshead speed test should continuously decrease because of the proportionality between strain rate and stress ($\dot{\varepsilon} \propto \sigma^2$). It is difficult to find reasons other than grain growth for the strain hardening observed. Transmission electron microscope studies[15] showed that the grain size increased after testing at 650°C (i.e. grains in the deformed sample were coarser than in the as-rolled material or the undeformed grip section). The structure in the as-tested material (after 100% deformation) is in general 3 to 4 times coarser[15] than the original grain size. This reasoning leads to the following interpretation of the true stress-true strain curve based on the equations presented in the introductory part. Figure 17 represents three actual tests done at the same temperature but at different strain rate. Curves based on the assumption that no grain growth will occur are also illustrated. If strain hardening is due to grain growth it should be possible to estimate grain growth kinetics during plastic deformation. The results of the calculations are contained in Table 2. The calculations are based upon the assumption that grain growth is the only hardening mechanism and that the stress depends on grain size to the 1.25 power.

As expected grain growth is a function of time at the same strain; the slow strain rate test shows the largest relative increase in stress and therefore in grain size. Figure 18 illustrates the calculated increase in grain size as a function of the strain for the three tests documented in Table 2. Grain growth is shown to be linear with strain but the slopes are a function of the strain rate and therefore the time to reach a certain amount of strain. These results point out that there could be a growth law governing the grain growth. It is natural to consider that the time law for grain growth might be a function of the square root of time (since the distance for diffusion is a function of $\sqrt{Dt}$). In Figure 19

Table 2

Calculated grain growth based on actual and theoretical true stress-true strain curves in Figure 17. Material: 1.6%C steel $(\gamma_w)c + 2_w$ (650°C), test temp. 650°C.

Crosshead speed in/min	True Strain ε	Strain rate $\dot{\varepsilon}(sec^{-1})$	σ_{theor} (ksi)	σ_{actual} (ksi)	
0.005	0	1.67×10^{-4}	3.5	3.5	$1.0 \cdot L_1$
	0.2	1.36×10^{-4}	3.16	7.4	$2.14 \cdot L_1$
	0.4	1.12×10^{-4}	2.87	8.7	$2.85 \cdot L_1$
	0.6	9.2×10^{-5}	2.59	9.5	$3.59 \cdot L_1$
	0.8	7.5×10^{-5}	2.35	9.95	$4.37 \cdot L_1$
	1.0	6.1×10^{-5}	2.12	10.2	$5.26 \cdot L_1$
	1.2	5.0×10^{-5}	1.92	10.25	$6.19 \cdot L_1$
	1.4	4.1×10^{-5}	1.74	9.7	$6.93 \cdot L_1$
	1.6	3.4×10^{-5}	1.57	8.2	$7.09 \cdot L_1$
	1.8	2.75×10^{-5}	1.42	4.8	$5.45 \cdot L_1$
0.02	0	6.67×10^{-4}	7.5	7.5	$1.0 \cdot L_1$
	0.2	5.46×10^{-4}	6.79	12.6	$1.77 \cdot L_1$
	0.4	4.47×10^{-4}	6.14	14.6	$2.35 \cdot L_1$
	0.6	3.66×10^{-4}	5.56	16.0	$2.96 \cdot L_1$
	0.8	2.99×10^{-4}	5.03	16.9	$3.64 \cdot L_1$
	1.0	2.45×10^{-4}	4.55	17.1	$4.30 \cdot L_1$
	1.2	2.01×10^{-4}	4.12	16.5	$4\ 90 \cdot L_1$
	1.4	1.64×10^{-4}	3.72	15.2	$5.40 \cdot L_1$
	1.6	1.35×10^{-4}	3.[illegible]	13.25	$5.66 \cdot L_1$
	1.8	1.10×10^{-4}	3.05	10.1	$5.36 \cdot L_1$
0.05	0	1.67×10^{-3}	12.7	12.7	$1.0 \cdot L_1$
	0.2	1.36×10^{-3}	11.5	19.0	$1.62 \cdot L_1$
	0.4	1.12×10^{-3}	10.4	21.1	$2.07 \cdot L_1$
	0.6	9.2×10^{-4}	9.4	22.2	$2.52 \cdot L_1$
	0.8	7.5×10^{-4}	8.5	22.4	$2.99 \cdot L_1$
	1.0	6.1×10^{-4}	7.7	22.3	$3.5 \cdot L_1$
	1.2	5.0×10^{-4}	7.0	21.8	$4.02 \cdot L_1$
	1.4	4.1×10^{-4}	6.3	20.8	$4.55 \cdot L_1$
	1.6	3.4×10^{-4}	5.7	18.6	$4.87 \cdot L_1$

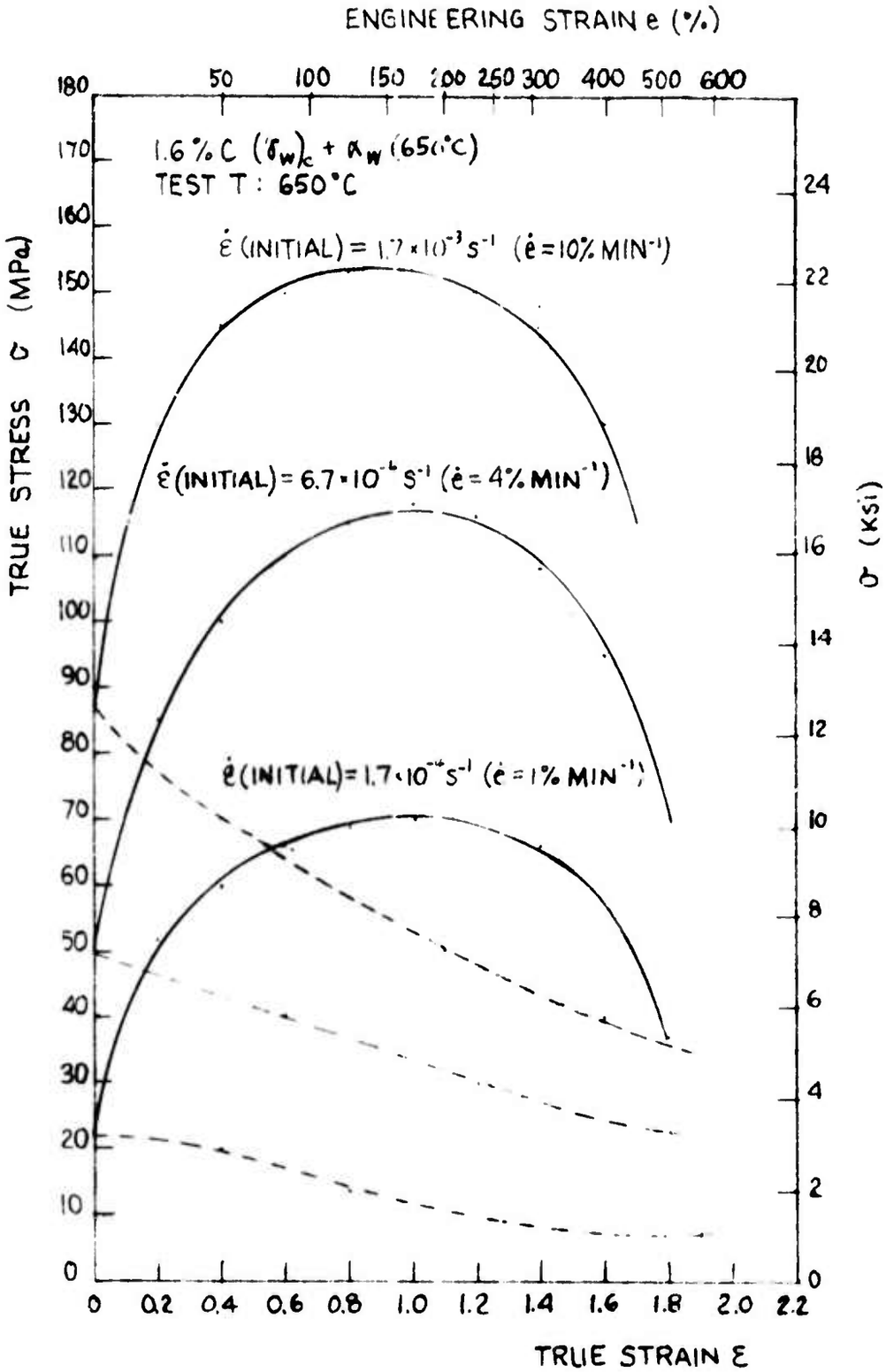

Figure 17. True stress-true strain curves for a 1.6%C steel at three strain rates at 650°C. Dashed lines are σ-ε curves expected at constant crosshead speed if no strain hardening occurred.

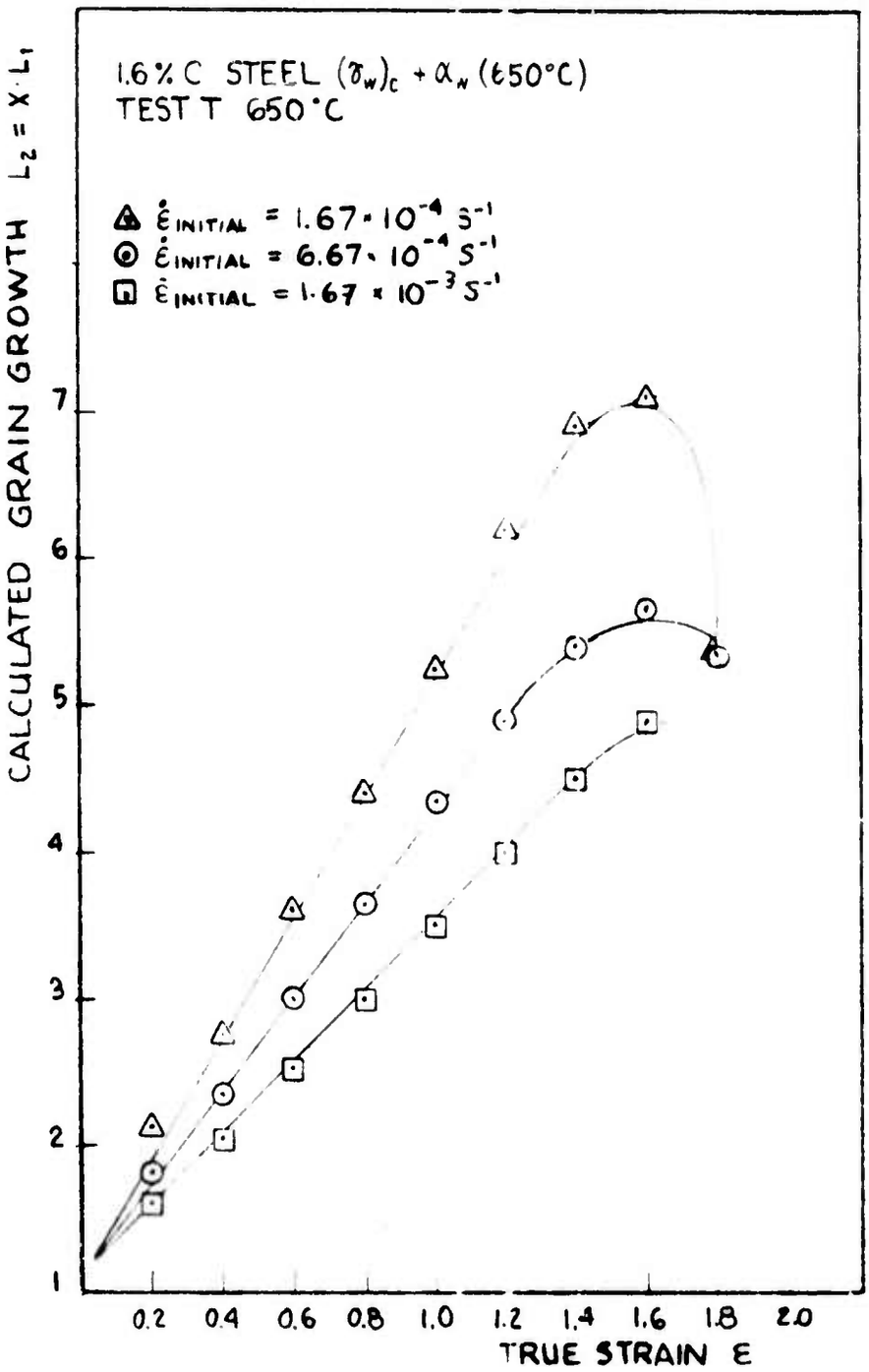

Figure 18. Predicted increase in grain size during superplastic flow in a 1.6%C steel based on the strain hardening behavior of the material.

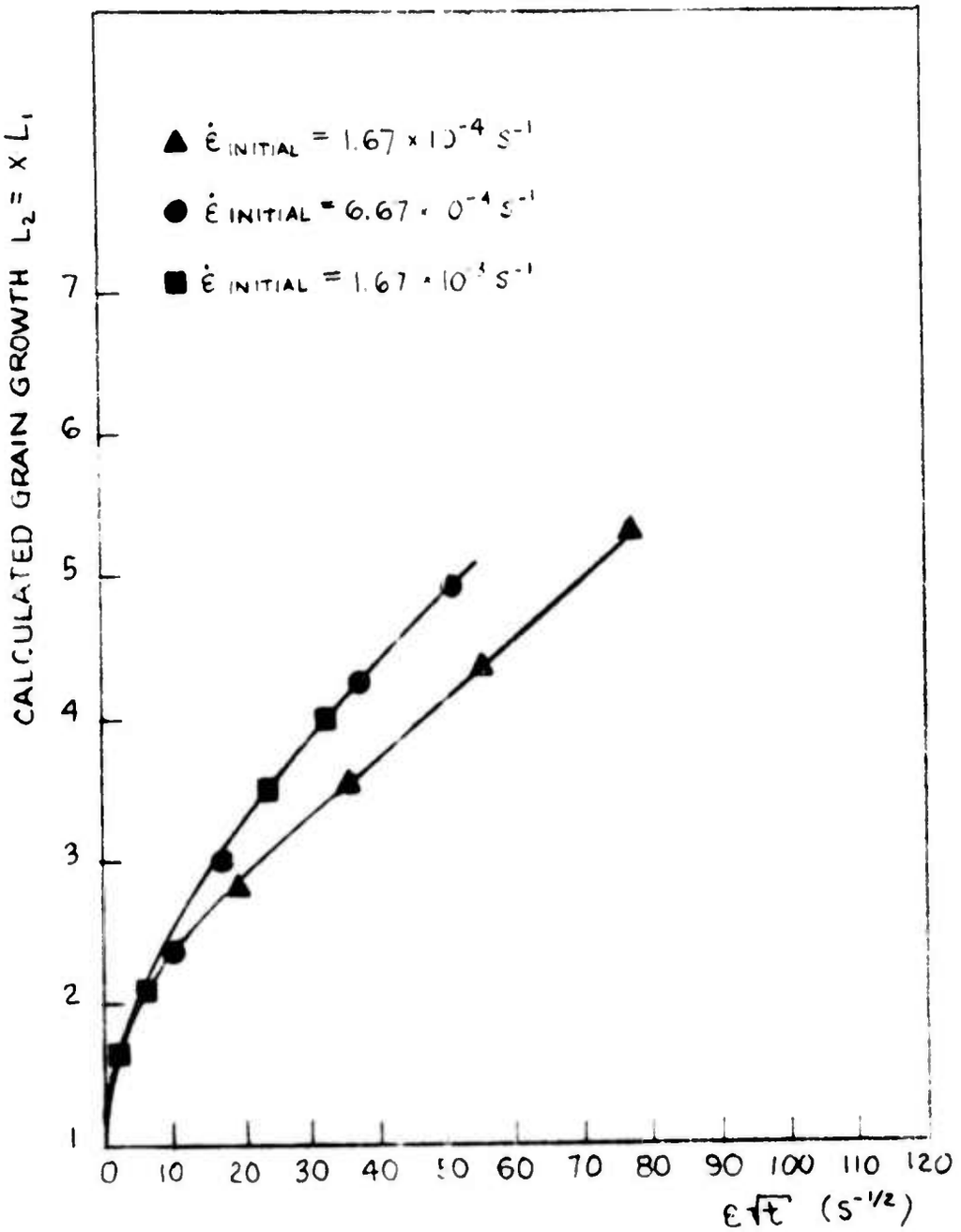

Figure 19. Predicted increase in grain size during superplastic flow in a 1.6%C steel as a function of the strain-time parameter, $\varepsilon\sqrt{t}$.

we plot the calculated grain size as a function of the strain and square root of time, $\varepsilon \cdot \sqrt{t}$. The data seem to fit within a narrow band of values and these preliminary considerations suggest that strain and time are the principal factors influencing grain growth during superplastic flow.

The following part describes some microscopic studies which indicate that grain growth occurs during superplastic deoformation. An electron transmission micrograph of a 1.9%C steel worked at 650°C is shown in Figure 20. The grain size of the as-rolled material is about 0.5μm. After a deformation of 100% the grain size increased to about 1.5 to 2 microns (Figure 20A-B). This observed grain size matches rather well the predictions made in Figure 18 for a 1.6%C steel. More straining(200%) led to more grain growth, the grain size is around 3μm (Figure 20C). This result is still in agreement with the predicted increase in grain size. Micrograph D in Figure 20 points out that straining very much enhances grain growth. Thus, the grip region (Figure 20D) of the same sample, where no straining occurred, exhibits a grain size of about 1μm after exposure to the same time at temperature; this grain size is about 3 times smaller than in the gage length.

(2) High Temperature Tests: Compression

a) Experimental procedure

The tests were done in a Instron-testing machine equipped with alumina platens on steel columns and a Marshall furnace. After soaking the sample for about one hour at the test temperature, change in crosshead speed tests were performed. The results presented in this section were done following the first testing scheme described in the section on tension testing. The sample was deformed to a certain strain followed by a sudden change in crosshead speed. The evaluation of the tests follows the same procedure as described earlier.

b) Results and Discussion

Compression tests are a very simple and fast method to measure m values and flow stresses. But to get more reliable results the temperature measurement has to be exact and one should follow a similar test pattern described earlier. Change in strain rate tests were done on the following materials.

1.3%C	$(\gamma_w)c + \alpha_w$	(650°C)	$\varepsilon_\alpha = 1.2$
1.6%C	$(\gamma_w)c + \alpha_w$	(400°C)	$\varepsilon_\alpha = 0.10$
1.9%C	$(\gamma_w)c$ no α_w		$\varepsilon_\gamma = 2.3$

One is to note that the 1.6%C and 1.9%C steels experienced little or no working in the α-range and therefore cannot be considered as representative of the behavior of a fully spheroidized material.

The true strain rate-true stress curves for the three materials are shown in Figures 21-23. The general behavior of all the materials is in accordance with the observations made in tension tests: the $\dot{\varepsilon}$-σ curves in the austenite range exhibit lower strain rate sensitivity exponents than in the ferrite range. The proposed explanation based on various deformation mechanism given earlier would appear to be equally applicable to the compression tests.

Although the 1.6% and 1.9%C steels are not fully spheroidized they show high m values at low strain rates. These are probably due to the fact that during the test considerable spheroidization occurs. The sample was always first tested at the high strain rates to a strain of about 0.4. The change to the slowest strain rate was performed as the last step and one can expect that the steels are better spheroidized by then.

The lines shown in Figures 21-23 were joined in the order of sequence of testing. The numbers given in Figure 21 illustrate the point. The 1.3%C and 1.9%C steels show an increase in strength at the same crosshead speed from the first (1) to the fourth (4) change. This increase in strength can be explained by the higher strain rate (which is taken into account) and by grain growth. But the 1.6%C steel exhibits the opposite behavior (Figure 22). A possible explanation for this result is that alpha working at 400°C resulted in a severely worked state; perhaps the additional straining reached by the fourth strain rate change at the test temperature leads to accelerated spheroidization. If a very fine spheroidized structure is obtained then it could be weaker than a less well developed spheroidized structure obtained during the first strain rate test. It is known that the 1.9%C steel is more difficult to spheroidize and that the effect of a better carbide distribution is not so important for this material. Based on the compression tests some activation energies were calculated in the normal way[9]; namely,

$$Q\Big|_{\sigma} = - \frac{4.576 \cdot \log \frac{\dot{\varepsilon}_1}{\dot{\varepsilon}_2}}{\frac{1}{T_1} - \frac{1}{T_2}}$$

where $\dot{\varepsilon}_1$ = strain rate at temperature T_1

$\dot{\varepsilon}_2$ = strain rate at temperature T_2

The calculated values are shown in Table 3. In general the activation energies obtained were as expected. At low values, in the superplastic range, Q was found equal to the value for grain boundary diffusion (Q_{gb} = 40 kcal per mole). At high

Table 3

Activation energies for plastic flow for the ultra high carbon steels.

Material	Range	T_1 (°C)	T_2 (°C)	at σ psi	Q_k cal/mole		
					1.3%C	1.6%C	1.9%C
	$\alpha+Fe_3C$	720	670	5000	29	62	24
				7000	34		
				9000	43	68	
				11000	44		42
				14000	50		
				18000	67	72	43
	$\alpha+Fe_3C$	670	625	9000	43	60	45
				11000	47		
				14000	53	70	65
				20000	56		
				26000	70	86	75
	$\gamma+Fe_3C$	820	770	4000	43	29	35
				6000	46	47	
				8000	57	37	58
				12000	61	51	
				14000	72		75

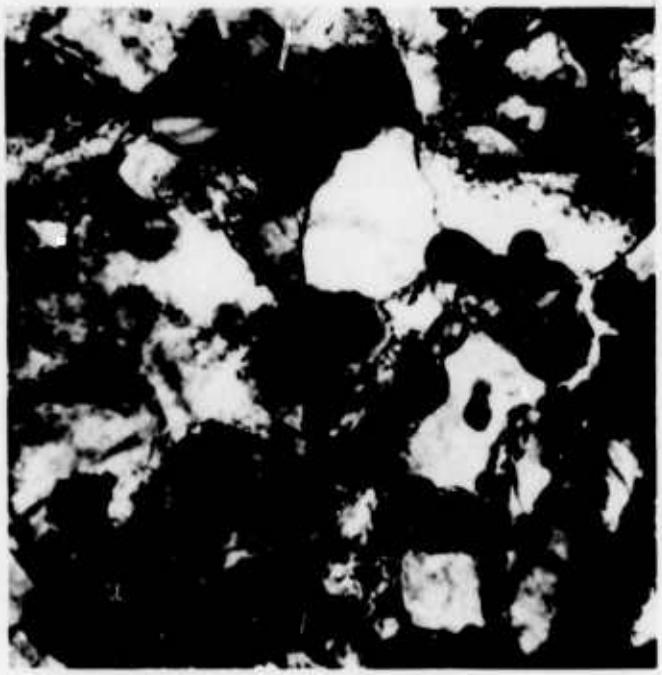

A - as rolled

B - e = 100%

C - e = 200%

D - grip region of sample C.

Figure 20. Transmission electron micrographs of a warm worked 1.9%C steel illustrating the grain growth that occurs during superplastic flow. (A) steel in as-rolled condition $(\gamma w)_C + \alpha w$ at 650°C), (B) and (C) superplastically deformed at 650°C and $\dot{e}$ = 1% per minute, (D) grip region of sample shown in (C).

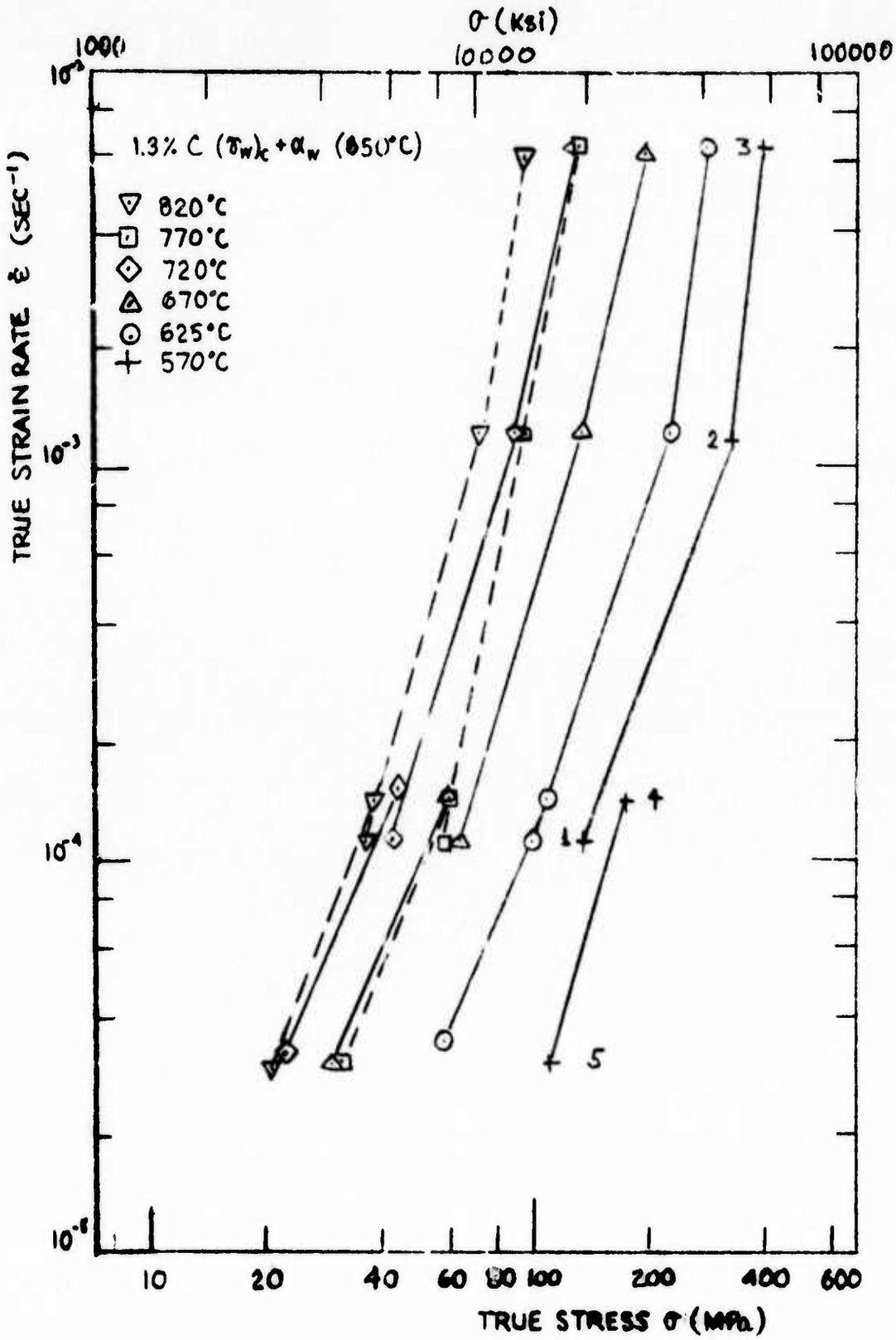

Figure 21. Flow stress-strain rate relation for a 1.3%C steel as obtained from strain-rate-change tests in compression in the temperature range 570 to 820°C. The strain rate change was made in the sequence shown (1→2→3→4→5).

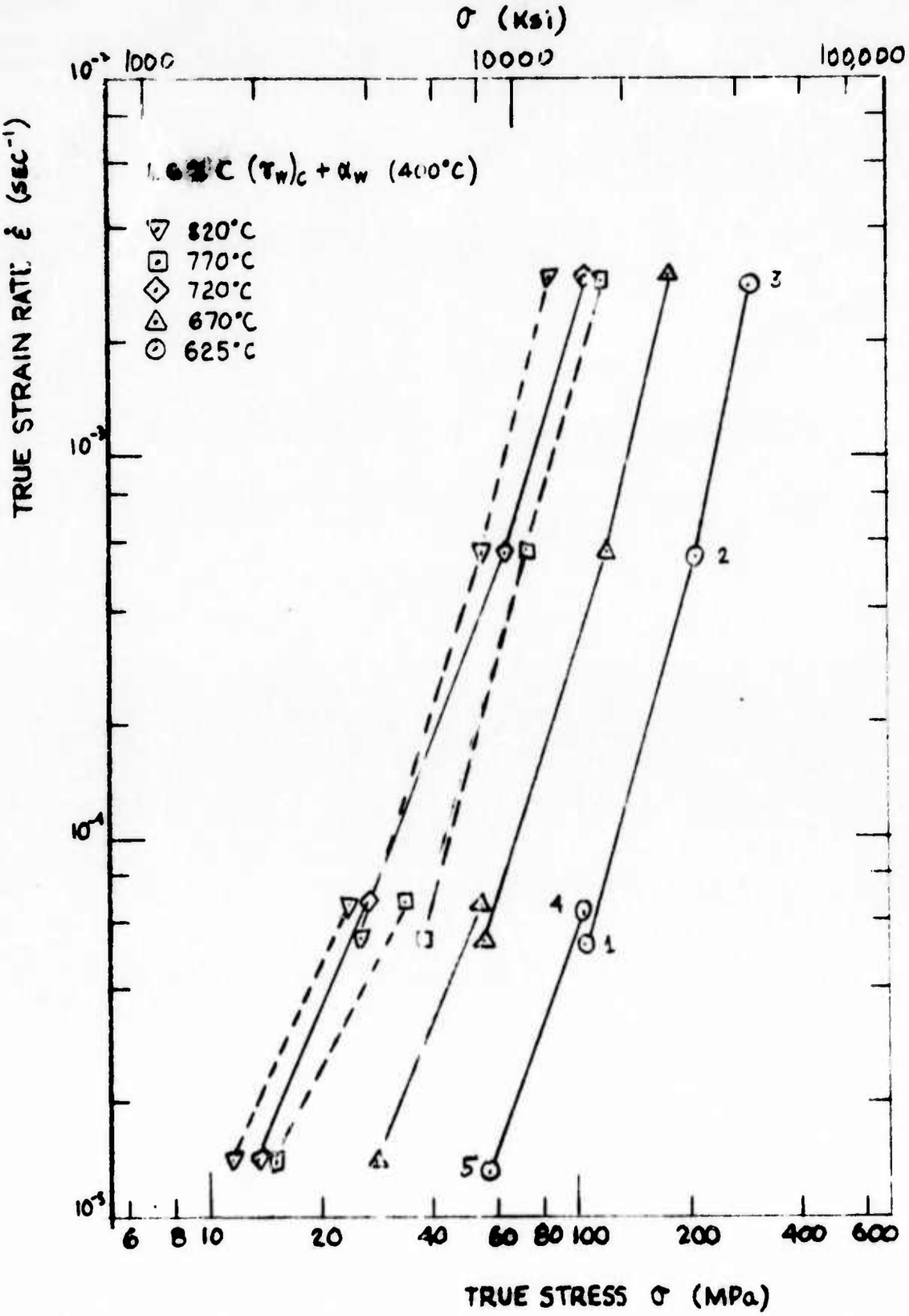

Figure 22. Flow stress-strain rate relation for a 1.6%C steel as obtained from strain-rate-change tests in compression in the temperature range 625 to 820°C. The strain rate change was made in the sequence shown (1→2→3→4→5).

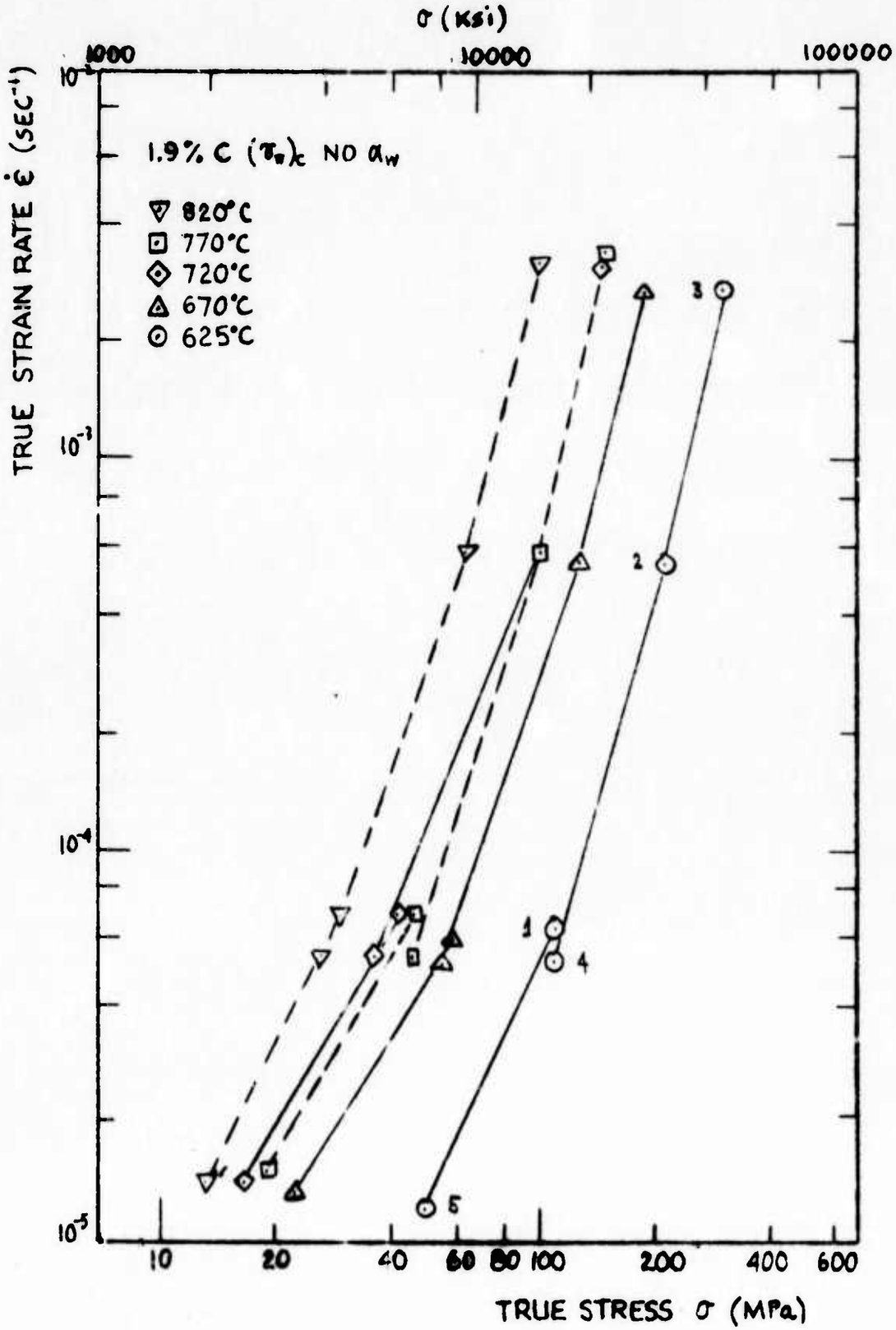

Figure 23. Flow stress-strain rate relation for a 1.9%C steel as obtained from strain-rate-change tests in compression in the temperature range 620 to 820°C. The strain rate change was made in the sequence shown (1→2→3→4→5).

stresses, in the slip creep range, Q was found equal to the value for lattice diffusion (Q_L = 65 kcal per mole).

From the tests shown in Figure 21-23, m values were calculated for three mean strain rates and plotted in Figure 24 as function of the testing temperature. The strain rate sensitivity is high over a wide range of temperatures. With increasing strain-rate the m values decrease. The highest values were observed for the 1.9%C steel although the tension tests showed that it is the least ductile. From the compression results one could conclude that the 1.9%C steel may be the best for forming processes but that due to not yet known factors premature failure occurs in tension.

c) Metallographic Observation

In order to get some information about grain growth after high temperature testing, metallographic samples were prepared. The method used was extraction replication and the replicas were examined with the electron microscope. Figures 25 and 26 present the results for two of the three tested ultra high carbon steels. The microstructure of the as-rolled 1.3% steel is shown in Figure 25A. The material was fine grained (~ 1µm) containing a duplex carbide structure with some pearlite islands remaining. The large carbides are the primary ones, whereas the small ones are spheroidized cementite from the original pearlite colonies Nevertheless, the material proved to be superplastic at 650°C (up to 700% elongation to fracture) and represents therefore a desirable structure. Testing at 570°C did not increase the grain and carbide size. At a test temperature of 670°C (Figure 25B), however, growth of the carbide particles occurred with an accompanying increase in grain size. Most of the pearlite islands have disappeared: the material was spheroidizing during the test. The grain size is now around 2µm and the observed structure is very equiaxed. One should note that the carbides do not form a continuous network in these two dimensional micrographs. At a test temperature of 720°C (Figure 25) considerable grain growth occurred (grain size about 3 to 3.5µm). But the structure is still very equiaxed and non continuous in terms of a carbide network. A test done above A_1 (T = 770°C) leads to a pearlite structure at room temperature (Figure 25D). The size of the primary carbides at 770°C is about the same as at 720°C (Figure 25C).

The 1.9%C steel was not isothermally worked in the alpha range and shows therefore a more pearlitic structure than the 1.3%C steel (Figure 26). At a test temperature of 620°C (Figure 26A) some spheroidization occurs. At 720°C the structure is almost fully spheroidized and some grain growth was observed to occur. In general the same observations made for the 1.3%C steel are valid for this material.

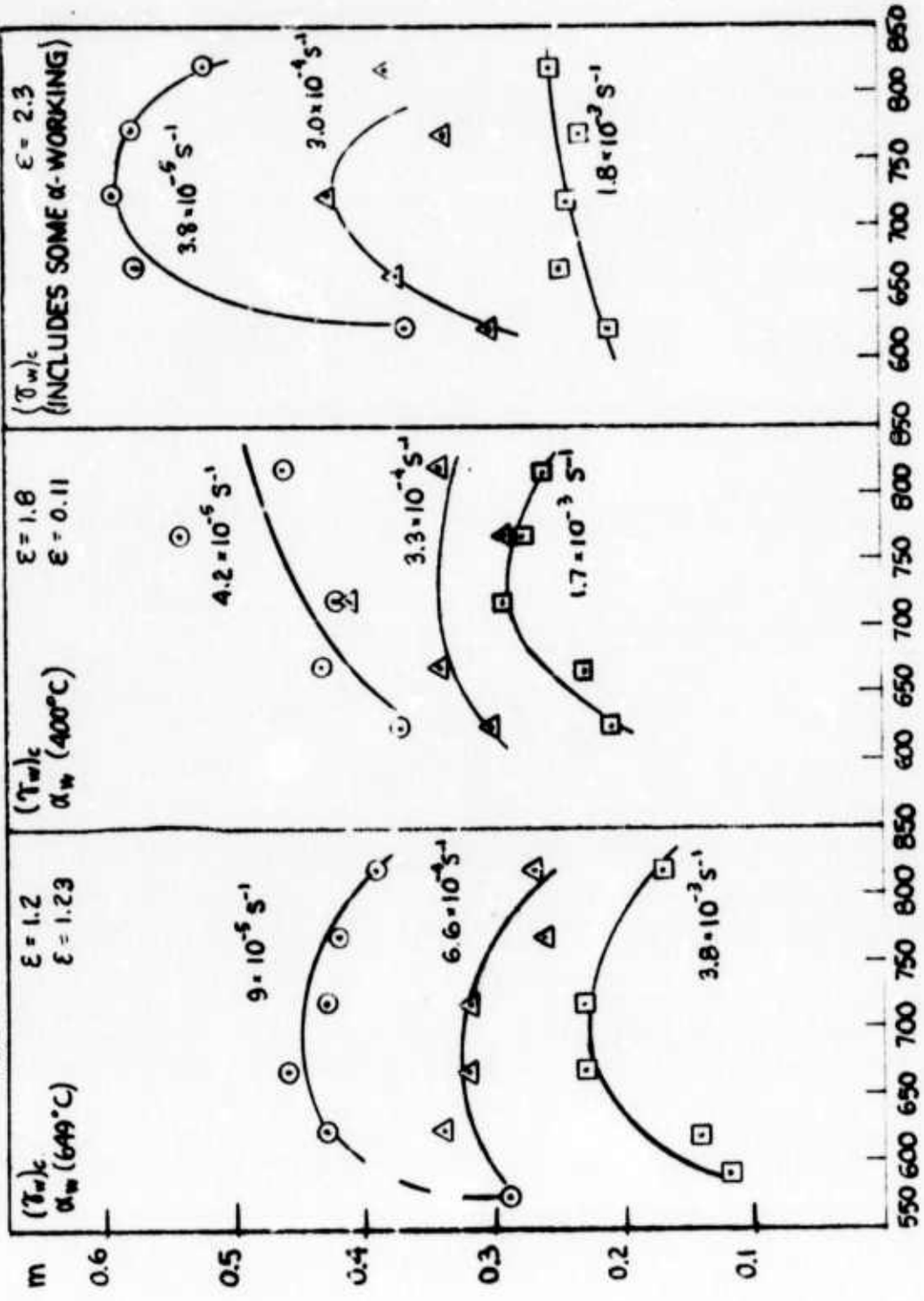

Figure 24. Strain rate sensitivity exponent as a function of temperature for the three commercial-grade steels investigated.

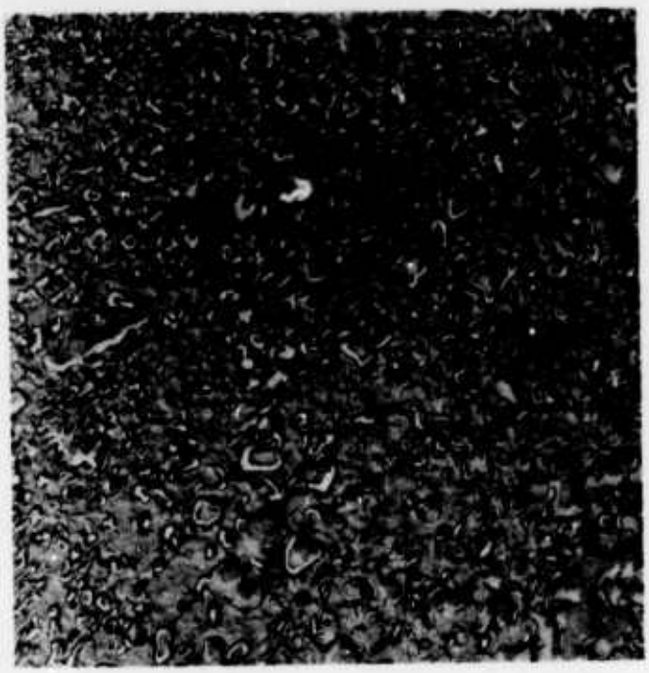

A. AS-ROLLED

B. 670°C

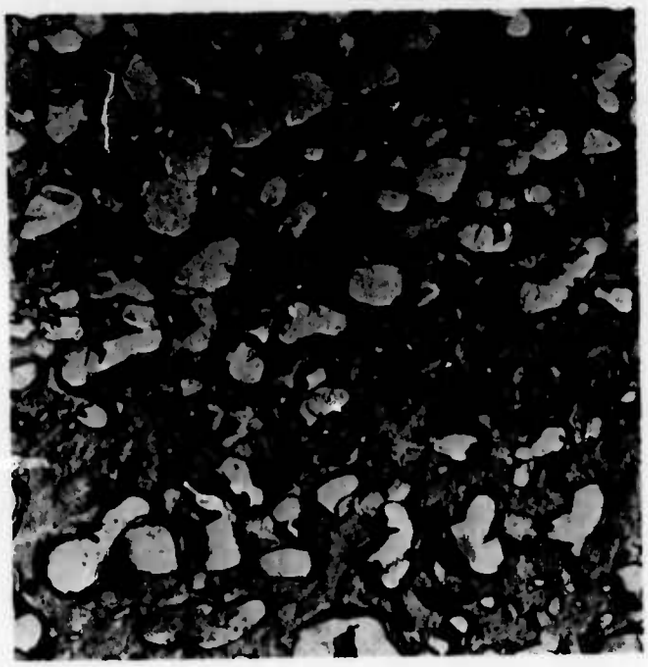

C. 720°C

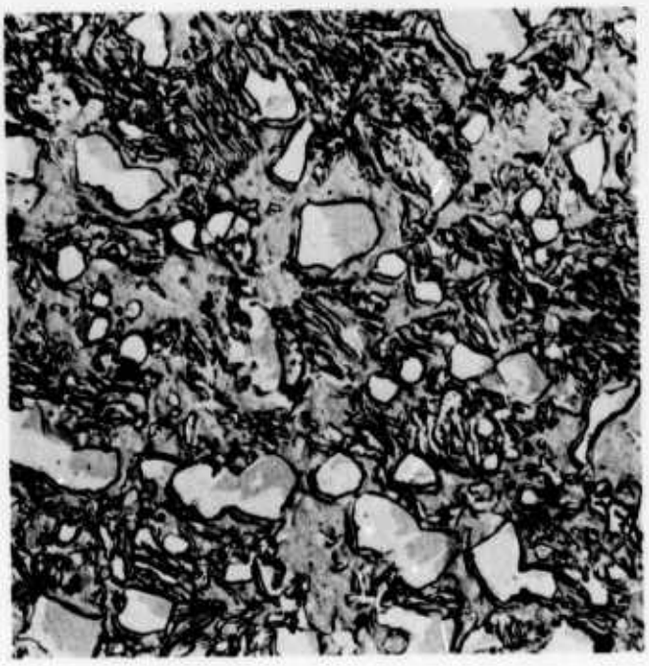

D. 770°C

Figure 25. Carbon replica micrographs of a warm worked 1.3%C steel illustrating the influence of compression creep deformation at various temperatures (ε = 0.5). The steel was originally worked during cooling in gamma and then alpha worked at 650°C to ε = 1.2.

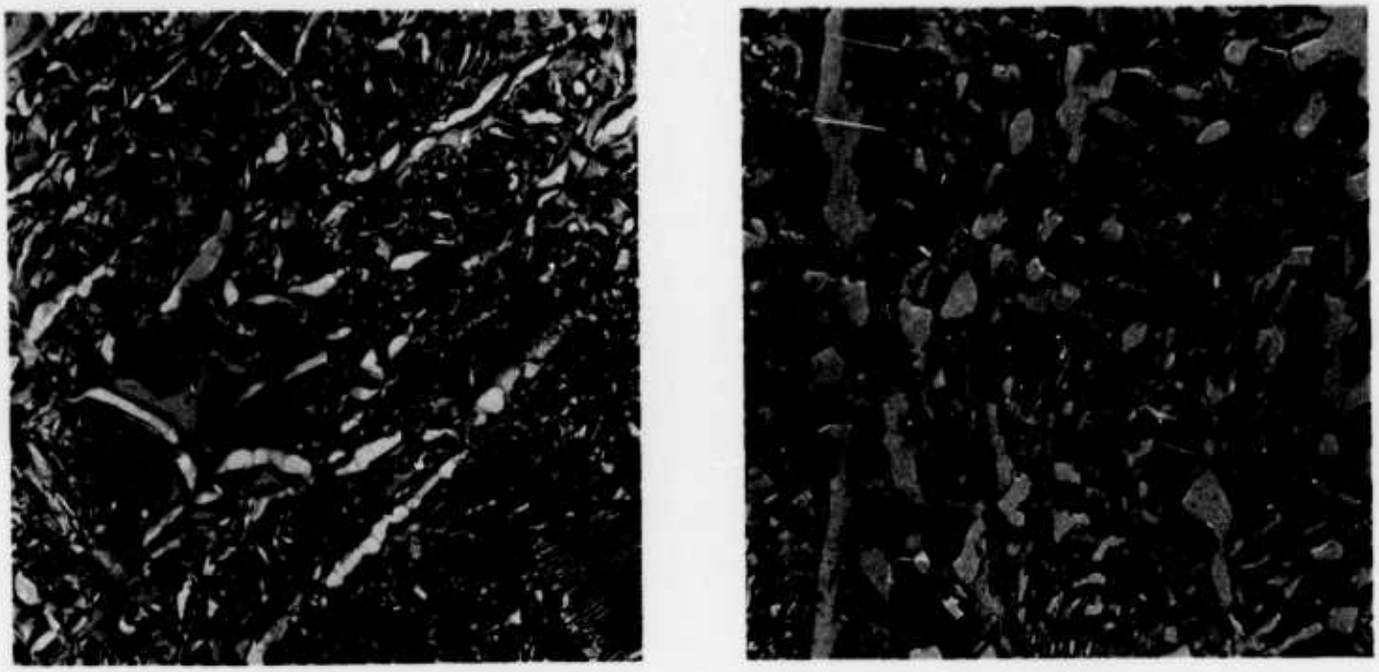

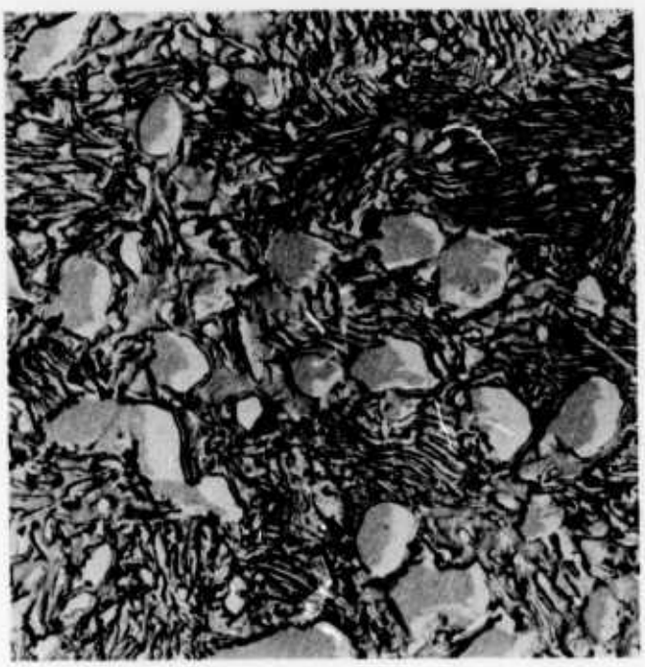

Figure 26. Carbon replica micrographs of a warm worked 1.9%C steel illustrating the influence of compression creep deformation at various temperatures (ε = 0.5). The steel was originally worked during cooling in gamma and was not subsequently worked in the alpha range.

3. Room Temperature Properties

a) Experimental Procedure

Room temperature properties of the ultra high carbon steels were obtained mainly by three testing procedures: tensile tests, hardness measurements, and bend tests.

i) Tensile Tests

All the tensile tests were done in our Instron machine and, in most cases, the extension was measured with a 1/2" extensometer. The engineering strain rate was 1.7×10^{-3} sec^{-1}. Figure 27 shows the standard flat tensile specimen used for all ambient temperature tests. Table 4 summarizes the tensile properties of as-rolled and as heat treated materials for the three ultra high carbon steels. As reported earlier[15] the 1.3%C steel exhibits the best room temperature properties: namely, very high strength and reasonable ductility. Annealing improves the ductility but lowers the strength somewhat. The results presented in Tables 4-1 to 4-3 point out that the room temperature properties can be manipulated by different factors. For example: 1) The higher the final rolling temperature in the isothermal α-rolling step the lower the strength and the higher the ductility of the final product at ambient temperature. 2) The amount of straining during α-working increases the ambient temperature strength and decreases the ductility. For example, in Table 4-2, test nos. 13, 14 and 15 (1.6%C steel) reveal the same (γw) cooling strain of 1.9, but different α-working strains (at 650°C); the room temperature yield strength increases with increasing strain. This increase in strength may be due to the fact that strain leads to a better spheroidized structure. The ductility, however, decreases in tension. This may be attributed to the fact that very high dislocation densities are produced at large strains and therefore the strain hardening potential will be reduced for room temperature deformation. A preliminary transmission electron microscope investigation[15] revealed that after rolling a very fine grained material with high dislocation densities and some subgrain formation is developed. In order to increase the ductility one has to anneal the as-rolled material.

Heat treatment after working is another factor influencing strength and ductility. Thus, very high strength, but low ductility, can be achieved by annealing at temperatures above A_1 followed by quenching. This leads to a martensitic or bainitic structure that can be tempered. There is evidence that the 1.3 and 1.6%C steels can be made very ductile by heat treatment. The 1.9%C

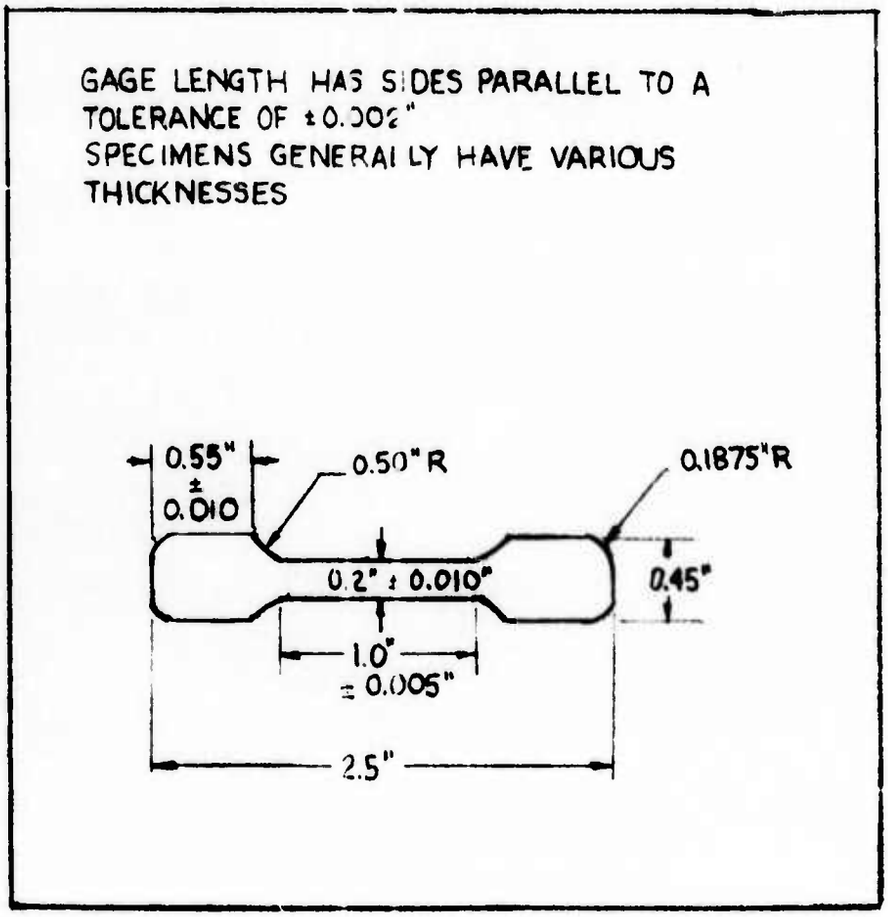

Figure 27. Drawing of standard flat tensile specimen used in room temperature tests.

Table 4-1

Material		Treatment	Yield Strength 0.2% offset ksi	MPa	UTS ksi	MPa	Elongation to fracture e (%)
1.3%C	1	γw+w.Q.+αw(565°C) $\varepsilon\gamma$=0.78; $\varepsilon\alpha$=1.68	186		204		4.0
	2	$(\gamma w)_C$+αw(565°C) $\varepsilon\gamma$ = 2; $\varepsilon\alpha$=0.81	188		205		1.7
	3	$(\gamma w)_C$+αw(650°C) $\varepsilon\gamma$=1.2; $\varepsilon\alpha$=1.23	147		182		7.2
	4	$(\gamma w)_C$+αw(650°C) $\varepsilon\gamma$=2.7; $\varepsilon\alpha$=1.33	124		143		7.1
	5	$(\gamma w)_C$+αw(650°C) $\varepsilon\gamma$=2.7; $\varepsilon\alpha$=2.06	147		150		2.1
	6	$(\gamma w)_C$+$(\gamma+Fe_3C)w$ at 850°C $\varepsilon(\gamma+Fe_3C)\tilde{=}$ 2	94.2		171		6.6
	7	$\gamma w]_C$+$(\gamma+Fe_3C)$ w850°C+αw(650°C) $\varepsilon(\gamma+Fe_3C)\tilde{=}2$ $\varepsilon\alpha$=1.2	130		145		4
	8	$(\gamma w)_C$+αw(565°C) $\varepsilon\gamma$=2; $\varepsilon\alpha$=0.81 +750°C/10min/air	120		158		6.0
	9	$(\gamma w)_C$+αw(650°C) $\varepsilon\gamma$=2; $\varepsilon\alpha$=0.81(as#2) 500°C/100 hrs	150		162		8.0
	10	$(\gamma w)_C$+αw(650°C) $\varepsilon\gamma$=2; $\varepsilon\alpha$=0.81(as#2) 700°C/30 min/air	124		151		13.3

Table 4-2

Material		Treatment	Yield Strength 0.2% offset ksi	MPa	UTS ksi	MPa	Elongation to fracture e (%)
1.6%C	11	$(\gamma w)_C + \alpha w$(565°C) $\varepsilon\gamma$=2.5; $\varepsilon\alpha$=1	194		219		2.0
	12	$(\gamma w)_C$+W.Q+αw(565°C) $\varepsilon\gamma$=1; $\varepsilon\alpha$=1.5	-		172		0.7
	13	$(\gamma w)_C + \alpha w$(650°C) $\varepsilon\gamma$=1.9; $\varepsilon\alpha$=1.14	118		140		4.9
	14	$(\gamma w)_C + \alpha w$(650°C) $\varepsilon\gamma$=1.9; $\varepsilon\alpha$=1.8	145		152		1.6
	15	$(\gamma w)_C + \alpha w$(650°C) $\varepsilon\gamma$=1.9; $\varepsilon\alpha$=1.95	154		157		1.1
	16	$(\gamma w)_C + \alpha w$(593°C) $\varepsilon\gamma$=2,2; $\varepsilon\alpha$=1.3	191		201		1.1
	17	$(\gamma w)_C + \alpha w$(593°C) $\varepsilon\gamma$=2.2; $\varepsilon\alpha$=1.6	174		182		1.0
	18	only $(\gamma + F_{e3}C)w$(850°C $\varepsilon(\gamma + F_{e3}C) \tilde{=} 3.0$	175		200		1.2
	19	$(\gamma w)_C + (\gamma + F_{e3}C)w$ (850°C) + αw(650°C) $\varepsilon\alpha \tilde{=} 2$; $\varepsilon\gamma = F_{e3}C \tilde{=} 2$; $\varepsilon\alpha \tilde{=} 1.2$	142		151		1.4
	20	$(\gamma w)_C + \alpha w$(565°C) $\varepsilon\gamma$=2.5; $\varepsilon\alpha$=1(as#11) +500°C/100 hrs/air			180		brittle
	21	(γw)+W.Q.+αw(565°C) $\varepsilon\gamma$=1; $\varepsilon\alpha$=1.5 +650°C/30 min/air	166		167		3.0
	22	$(\gamma w)_C + \alpha w$(650°C) $\varepsilon\gamma$=1.4; $\varepsilon\alpha$=1.7 700°C/90 min/air	125		129		4.8

Table 4 -3

Material		Treatment	Yield Strength 0.2% offset ksi	MPa	UTS ksi	MPa	elongation to fracture e (%)
1.9%C	23	$(\gamma w)_C + \alpha w$(650°C) $\varepsilon\gamma$=2.3; $\varepsilon\alpha$=1.1	146		148		1.0
	24	$(\gamma w)_C + \alpha w$(565°C) $\varepsilon\gamma$=1.9; $\varepsilon\alpha$=0.9	208		212		0.4
	25	$(\gamma w)_C + (\gamma + F_{e3}C)w$850°C $\varepsilon\gamma \tilde{=} 2$; $\varepsilon\gamma + F_{e3}C \tilde{=} 2$	89		133		2.5
	26	$(\gamma w)_C + (\gamma + F_{e3}C)w$850°C $+\alpha w$(650°C) $\varepsilon\gamma \tilde{=} 2$; $\varepsilon\gamma + F_{e3}C \tilde{=} 2$; $\varepsilon\alpha$=1.2	120		124		0.5

steel could not be made to exhibit such ductilities, but a special working procedure $(\gamma w)_C + (\gamma+Fe_3C)w$ at 850°C, (#25) leads to a reasonable elongation to fracture (2.5%).

It is obvious that the tensile room temperature properties can be altered by different means but much more systematic studies are needed here.

ii) Hardness-tests

The influence of rolling conditions on the strength of a material are rather clearly shown with the help of room temperature hardness measurements. In Table 5 the change in hardness with the amount of warm working strain is demonstrated. A similar increase in strength with strain was shown for a ferritic stainless steel[16]. It would be interesting to find out if continuous deformation at temperature compared with deformation accompanied by reheating leads to a difference in substructure and therefore in hardness increase. It seems that the reheating process produces recrystallization and a very fine grain structure whereas continuous deformation perhaps achieves a very fine subgrain structure. This would probably yield different behavior at high and at room temperature. Simulation of the warm working deformation history by torsion testing could be worth-while here. Such apparatus is available at Stanford.

The hardness is also affected by the final warm working temperature. This is shown by the result given below. Although the warm working strains are not constant, it is obvious that the final temperature has a very strong influence on the subsequent ambient temperature properties: the higher the final working temperature the softer the rolled product.

Material	Final warm working temperature	ε_α	R_c
1.6%C	565	1.0	45
	593	1.1	42
	650	1.1	30
1.3%C	538	0.25	36
	565	1.68	37
	650	1.23	30

Table 5

Hardness as function of warm working strain

Material	Treatment	Warm working strain	R_c
1.6%C	only $(\gamma w)_C$	$\varepsilon\gamma = 1.9$ $\varepsilon\alpha = 0$	26
	$(\gamma w)_C + \alpha w(650°C)$	$\varepsilon\gamma = 1.9$ $\varepsilon\alpha = 1.1$	30
		$\varepsilon\gamma = 1.9$ $\varepsilon\alpha = 1.8$	39
		$\varepsilon\gamma = 1.9$ $\varepsilon\alpha = 1.95$	41
1.6%C	$(\gamma w)_C + \alpha w(593°C)$	$\varepsilon\alpha = 1.1$	42
		$\varepsilon\alpha = 1.3$	44
		$\varepsilon\alpha = 1.6$	44

The hardness can be changed by heat treatment. Table 6 represents a few studies done on a 1.3%C and a 1.9%C steel. The hardness is a function of annealing time and annealing temperature (Figure 28). It would appear that a R_c = 35 yields a material with good ductility combined with fairly high strength. This rule of thumb is not fully true for the 1.9%C steel where R_c values below 30 did not yield a very ductile material.

iii) Bend Tests

The three point bend test represents a relatively fast low cost method to evaluate the strength and ductility of as-rolled and as heat-treated materials. The following section describes results obtained on 1.6%C steel. Specifically, the influence of different annealing treatments on the ductility and strength was assessed. As a measure of the ductility the plastic deflection D of the sample was determined (Figure 29). D is measured from the beginning of plastic deflection until the first crack in the outer fiber occurred. Some difficulties arose for the determination of the strength: in general the values measured in bending were between 30 and 40 ksi higher than similar values measured in tension. Preliminary bend tests showed that transverse properties were comparable to longitudinal properties in our rolled sheet, suggesting that isotropic structures were developed.

The influence of annealing temperature on the hardness and bend of ductility our rolled 1.6%C steels is shown in Figures 28 and 29. The annealing time was held constant at 30 minutes. Dramatic changes can be produced by annealing our steel at 750°C and then water quenching. The hardness reaches values (Rc = 67) observed for only a few ferrous materials. As expected these high strength materials do not have any ductility. Annealing of the quenched plates leads to a gradual decrease in hardness, whereas the ductility can be improved at temperatures around 600°C. Our studies revealed that a quenched and 700°C annealed material exhibits about the same ductility but a slightly higher hardness than a plate heated to 750°C and air cooled. Homogenizing and oil quenching of a $(\gamma w)_C$ 1.6%C steel yields a fairly hard but brittle material. Increasing the annealing temperature changes the room temperature properties following the same pattern as described above. Annealing at 700°C leads to a very soft and ductile material.

From the fracture behavior of the bend test samples some preliminary conclusions about the toughness of ultra high carbon steels can be made. The materials with the highest strength are very brittle. But a combination of an acceptable strength with relatively good ductility produces a tough material: the crack does not

Table 6

Influence of different heat treatments on the room temperature hardness of ultra high carbon steels.

Material	Rolling and heat treatments	R_c	Remarks
1.3%C	$(\gamma w)_C$ + αw (650°C)	35	spheroidized
	+750°C/10 min/H_2O	62	martensite
	+200°C/60 min/	58	(Heat treatments
	+300°C/10 min	56	done on the same
	+400°C/10 min	50	sample in the order shown)
	or 500°C/ 100 hrs	30	spheroidized
	or 700°C/ 30 min	30	spheroidized
1.9%C	$(\gamma w)_C$ + αw (650°C)	40 5	spheroidized
	750°C/ 30 min/ air	35	pearlite
	$(\gamma w)_C$ + αw (565°C)	43	spheroidized
	+650°C/ 30 min	39	spheroidized
	or 650°C/ 240 min	34	spheroidized
	or 650°C/ 480 min	30	spheroidized
	or 500°C/ 100 hrs	42	spheroidized

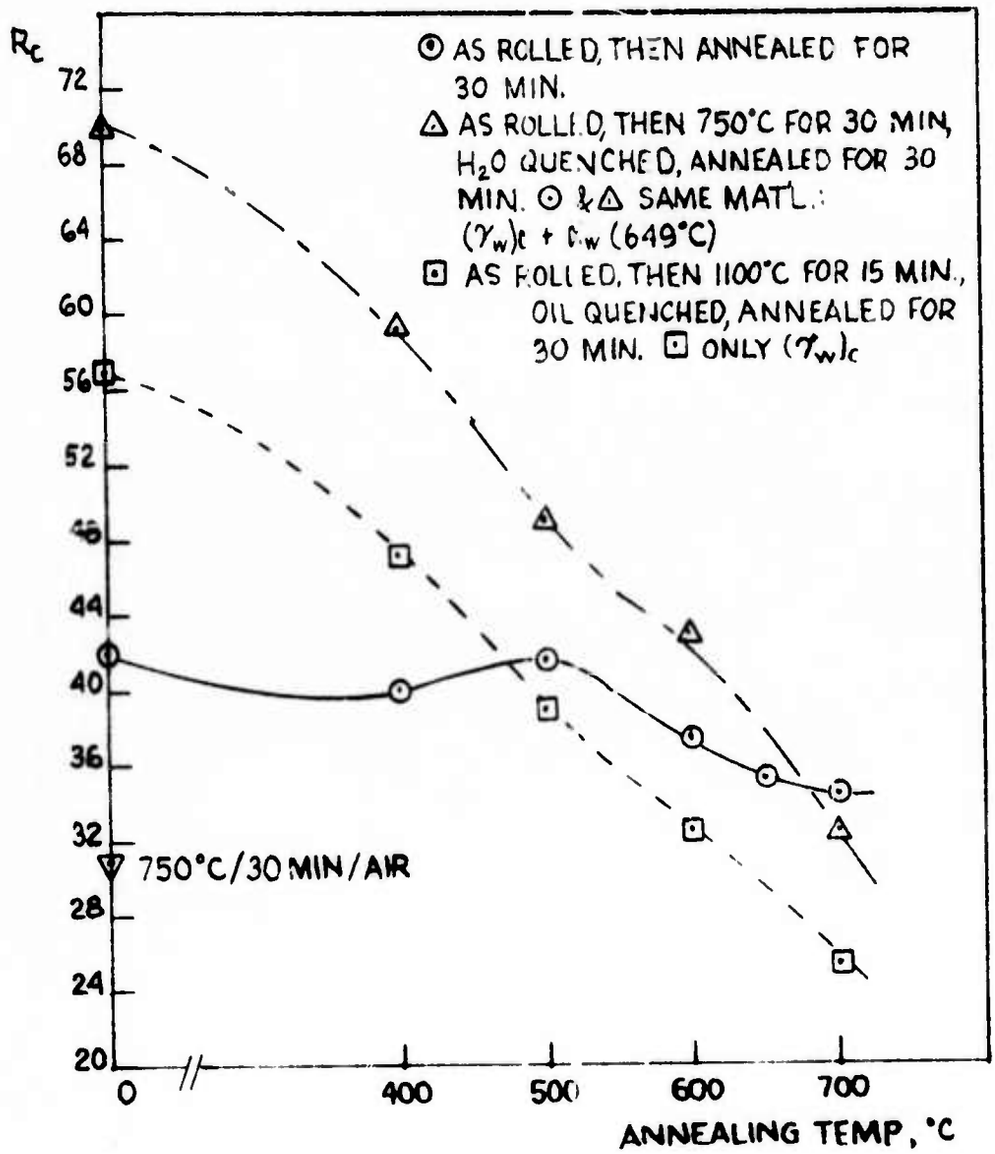

Figure 28. Influence of various heat treatments on the hardness of a 1.6%C steel.

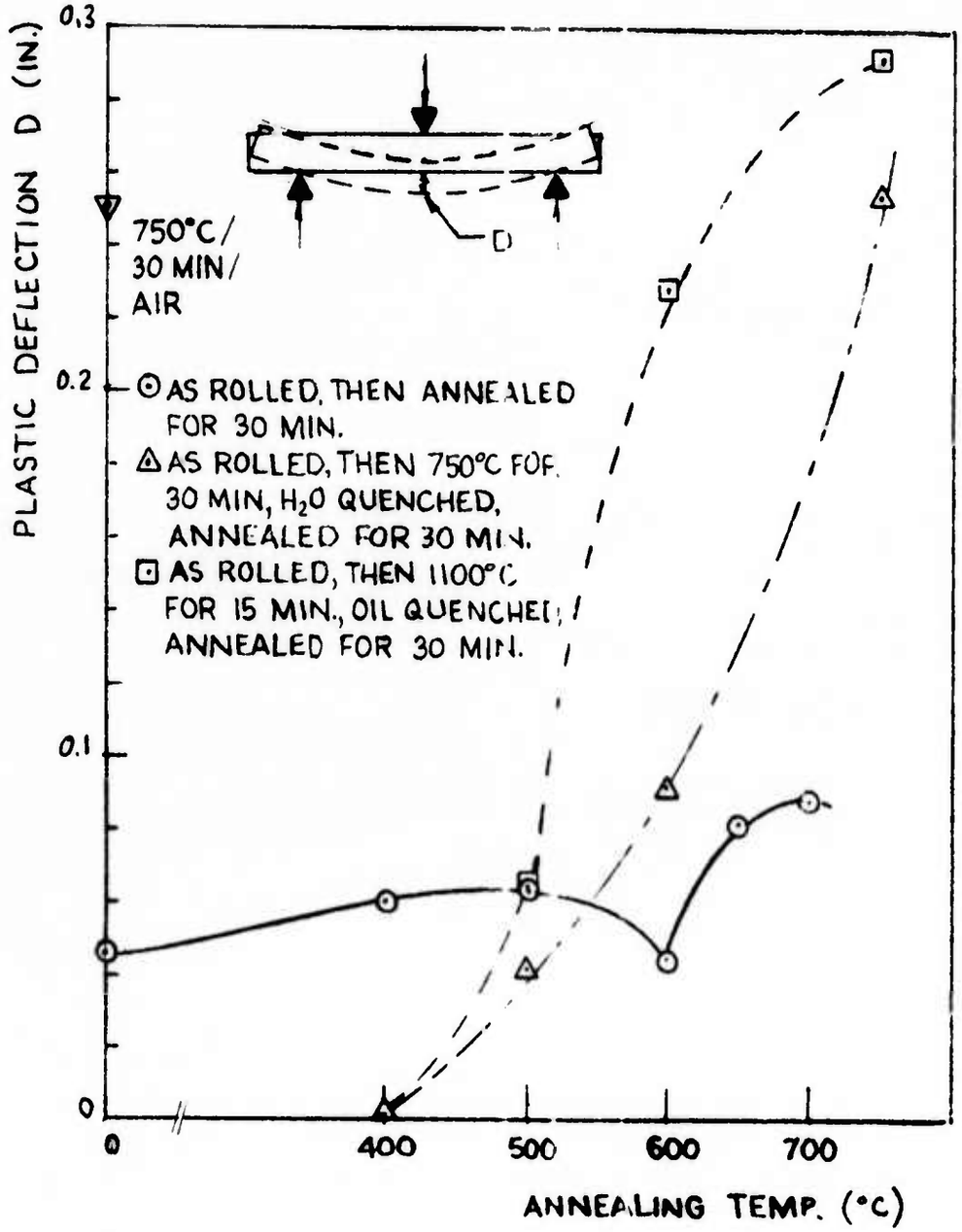

Figure 29. Influence of various heat treatments on the ductility of a 1.6%C steel from three point bend tests. D is measured as the linear deflection to the start of the first visible crack (see sketch).

58-C

propagate very rapidly through the material.

It is obvious that our investigation of the room temperature properties of the ultra high carbon steels is very incomplete. Nevertheless, the results show that it is possible to produce materials with high strength combined with good ductility.

4. References

1. Oleg D. Sherby, Bruno Walser, Conrad M. Young and Eldon M. Cady, Third Semi-Annual Progress Report to Advanced Research Projects Agency, Grant No. DAHC-15-73-G15, February 1975 (Center for Materials Research, Stanford University, Stanford, California, 94305).
2. Oleg D. Sherby, Bruno Walser, Conrad M. Young and Eldon M. Cady, Scripta Metallurgica, 9, 1975, p. 569.
3. G. Rai and N. J. Grant, Met. Trans., 6A, 1975, p. 385.
4. H. Naziri and R. Pearce, Acta Met., 22, 1974, p. 1321.
5. M. L. Vaidya, K. Linga Murty and J. E. Dorn, Acta Met., 21, 1973, p. 1615.
6. C. M. Packer and O. D. Sherby, Transactions ASM, 60, 1967, p. 21.
7. H. W. Hayden, R. C. Gibson, H. F. Merrick and J. H. Brophy, Transactions ASM, 60, 1967, p. 3.
8. K. B. Gove and J. A. Charles, Mets Tech., 1, 1974, p. 229.
9. O. D. Sherby and P. M. Burke, Prog. Mats. Sci., 13, 1968, p. 325.
10. E. Koester, Z. Metallkunde, 39, 1948, p. 1.
11. T. Watanabe and S. Karashima, Met. Trans., 2, 1971, p. 1359.
12. S. Kayali, work in progress, Stanford University, 1975.
13. A. R. Marder, Trans. Met. Soc. of AIME, 245, 1969, p. 1337.
14. G. R Yoder and V. Weiss, Met. Trans., 3, 1972, p. 675.
15. First Annual Technical Report, Defense Advanced Research Project Agency, DAHC 15-73-G15, June 1974, p. 31, (Center for Materials Research, Stanford University, Stanford, California, 94305).
16. C. M. Young, B. Walser and O. D. Sherby, Final Report, Army Materials and Mechanics Research Center, May 1974, DAAG-46-73-C-0163.

IV. SYNTHESIS OF NEW TYPES OF CATALYST MATERIALS

J. P. Collman

Professor of Chemistry

M. Boudart

Professor of Chemical Engineering
and Chemistry

and

W. A. Little

Professor of Physics

A. Hybrid Homogeneous-Heterogeneous Catalysts

J. P. Collman

1. Introduction

This section concerned with hybrid homogeneous-heterogeneous catalysts is divided into two parts--the first dealing with a new class of conducting catalyst supports (transition metal dichalcogenide layered compounds), and the second with silated ligands to be used with silica supported homogeneous catalysts. This work has been carried out in the laboratories of J. P. Collman with consultation from M. Boudart (Chemical Engineering). Materials assistance has been provided by T. H. Geballe (Applied Physics).

2. Group V Dichalcogenides as Catalyst Supports

M. Marrocco

a. Introduction

This group has had a continuing interest in the modification of the activity of homogeneous catalysts through attachment to solid phase supports. Our interest in this area stems from our belief that in addition to acquiring many of the desirable properties (ease of removal, amenability to flow rather than batch processes) of heterogeneous catalysts, supported complexes might exhibit higher activity than their soluble analogs. This enhanced activity might be obtained by "trapping" on the solid surface coordinatively-unsaturated species similar to intermediates proposed in reaction schemes for some well studied homogeneous catalysts.[1,2,3] Homogeneous catalysts are in general more selective and less easily

poisoned, properties expected to be retained upon supporting these complexes. Control of the reactive site by chemical design seems feasible with these catalysts. One stage multi-step reactions using two different supported catalysts is another example of the potential of this technique[7].

We have had prior experience with polymeric organic supports and also with silica materials. The literature[4,5,6] in both these areas is steadily growing in spite of the fact that such supported catalysts are difficult to study--primarily because of the paucity of effective analytical methodologies. It is probably not possible to characterize a surface complex to the degree to which crystallizable compounds are routinely analyzed. Methods of following reactions are also limited and mechanistic studies are very difficult. Kinetic results provide little information beyond absolute rates and their response to indirect variables. These difficulties are not insurmountable. For instance, there is much to be learned from the particular products of catalytic reactions. Specific activity may be utilized to differentiate between catalysis by supported metal particles and supported metal compounds. Surfaces modified to include chiral ligands allow study of induced optical activity.

A set of materials has recently come to our attention as potentially useful support phases. These are the early transition metal dichalcogenides. These compounds are layered and like graphite and other layered materials form intercalation compounds

with a variety of substances. The properties of the pure metal dichalcogenides (MCh_2) and their intercalates have been investigated at Stanford in the Applied Physics Department by Geballe's group[8], whose interest has been directed toward the modification of low temperature electrical properties on intercalation. Other groups elsewhere, also mainly interested in the physics of MCh_2 compounds, have produced a literature of respectable size and have discovered some effects which seemed to offer opportunity for chemical study and application.

MCh_2 compounds may be intercalated with protons using an electrolytic technique[9]. If then placed in an appropriate solvent system and vigorously stirred, they will intercalate additional quantities of solvent until their layer structure is completely disrupted becoming sheets three atoms thick and up to several microns across. Experiments have demonstrated that these are giant planar anionic, sulfur-tantalum-sulfur sandwiches, whose negative charges are balanced by a layer of protons held electrostatically to the surface[10]. Other cationic species were found to displace the surface protons[11]. This process could be followed with visible spectra as adsorbed species studied formed surface aggregates with altered electronic spectra. The dispersed form of these compounds exhibit a remarkable average surface area, every sulfur atom being exposed. Dispersed NbS_2 is calculated to have a surface area of about 650 m^2/g. Before dispersion, these compounds exhibit this

apparent surface area only to substances which will intercalate. High surface area is, of course, a primary requirement for a catalyst support. The electrical properties of MCh_2 can be varied from insulating through semiconducting to metallic by choice of the metal and crystalline phase. Working with conductive phases, one could hope to observe surface species using electrochemical techniques. Interactions of MCh_2 are thought to be of a donor-acceptor type. The thermal conductivity of these substances may prove useful in the catalysis of highly exothermic reactions. Our long term interest in such intercalcated catalysts is their use as highly selective electrode catalysts.

Thus, our aim has been to investigate MCh_2 compounds as conductive support materials. Work was done first on electrochemistry of the pure crystalline materials. We then attempted to intercalate a number of catalytically active metal complexes. We have also attempted to use ESR as a method for detecting the intercalated compounds. Finally, we have briefly examined the catalytic activity of these systems.

Cyclic voltammetry is the method chosen for our preliminary electrochemical studies. Small single crystals of 2H-TaS_2 were mounted with wax in the tip of a disposable pipette in such a fashion that a portion was accessible to contact with mercury inside the pipette and another portion was free to contact the cell solution outside of the pipette. Small crystals had to be

used because the high currents drawn as a consequence of the large effective surface area could overload the potentiostat. These studies were mainly carried out in water varying the electrolyte. Some measurements were carried out in nonaqueous solvents although these are somewhat less reliable due to solvent purity problems. TaS_2 showed qualitatively similar behavior in various cell systems. In acid electrolyte a complex system of peaks accompanies H_2 evolution. In non acidic electrolytes this was not observed. In both cases a set of three peaks occurred upon cathodic scanning from O.v SCE. The position of these peaks is dependent on scan rate, pH, solvent, and for $NbSe_2$ the peaks are shifted half a volt cathodic with respect to TaS_2 leaving a large "electrochemical window" for studying surface reactions of adsorbed metal complexes. In some systems these peaks have associated reverse waves. They do not represent reversible processes in any case. In the anodic direction a passivation occurs, the current reaching a limiting plateau constant out to 5 to 10 volts.

At this point, assignment of the electroactive species was not possible. We felt a useful approach would be to try to detect a reversible process involving an intercalate species. Here an alternate electrode geometry was devised. A copper wire was sealed into a thick walled glass capillary tube leaving about one eighth inch open tube at the end with the copper wire just exposed at this end. TaS_2 as a wet powder could be packed tightly into the open end, contact being made through the copper. This arrangement

does not completely isolate the copper from the cell electrolyte, however the results were similar to studies with single crystals. Electrically prepared $TaS_2 \cdot H_x$ was stirred with $Rh(diphos)_2Cl$ or $AgNO_3$ solutions in attempt to displace the protons with the metal cations. The resulting powders were used to fabricate capillary electrodes. Additional peaks were observed but none displayed reversible behavior. We also failed to see a reversible I_2/I^- couple using a single crystal TaS_2 electrode. Several methods were applied in attempt to prepare intercalates of tetra(N-methyl-4-pyridal)-porphryin, tetra-4-pyridalporphyrin, the corresponding two Fe complexes, tetra-o-aminophenylporphyrin, $Rh(diphos)_2ClO_4$* and $Rh(di||phos)_2ClO_4$--all without success.

During the course of these experiments the need for a simple analytical tool became increasingly clear. In an effort to remedy this problem we looked to ESR. Paramagnetic metals had been intercalated into TaS_2 in the literature using electrolytic techniques. It seemed an easier goal instead to intercalate the radical cation of N,N,N',N'-tetramethyl-p-phenylenediamine (Wurster's blue salt). The neutral compound was known to intercalate TaS_2[12] and there was potential information about the amine--TaS_2 interaction to be had. No intercalation of a radical species was achieved. We have not yet attempted to form the radical cation

*diphos≡1,2-bis(diphenylphosphine)ethane
di||phos≡1,2-bis(diphenylphosphine)ethylene

after intercalation of the neutral diamine. Intercalation of 2,2,6,6-tetramethyl-4-hydroxypicoline-N-oxide (a spin-label) met with limited success. In the first experiment two peaks could be resolved near g=2. They were unfortunately obscured due to instrumental problems. A second experiment produced a single peak indicating concentration broadening. Reflux in benzene rather than forcing deintercalation only broadened the peak drastically. In a number of experiments a signal at g 4.4 has also been observed and while its origin is unclear, it may represent metallic contamination. We hope that ESR will prove to be a valuable tool in further studies.

One attempt at electrochemical hydrogenation of olefins using a TaS_2-$Rh(diphos)_2$ system failed. The $RhCl_3$-TaS_2 system was more successful. We had hoped to mimic the known catalytic complex $Cl_3Rh(Et_2S)_3$[14] by adding $RhCl_3$ to dispered TaS_2 so that three adjacent sulfurs of a TaS_2 slab would take the place of the thioethers. The system should be amenable to modification by using electrocatalytic processes. Using conventional techniques, cyclooctene was hydrogenated at room temperature under 40 psi H_2 to cyclooctane. Products were checked by gas chromatography (glc) using coinjection of pure compounds to identify alkene and alkane. A control with all components present except TaS_2 proved inactive. After twelve hours TaS_2 dispersion was added and activity demonstrated. This catalyst became inactive after reducing 10^3

equivalents of olefin. TaS_2 alone is also inert under these conditions. Systems incorporating $RuCl_3$ and $IrCl_3$ have not shown activity.

It is the ability to exfoliate these layered compounds thereby generating high surface area conductors which has provoked our interest. As mentioned earlier, it has recently been found that this process can be taken to the extreme limit in which the TaS_2 planes are completely isolated from each other by solvent. The early reports[11] of dispersing these complexes required intercalating protons from aqueous acid into charged layers. We found DMSO to be effective as a dispersing solvent but only after previous exfoliation with water. DMSO dispersions were also easily precipitated. In his doctoral thesis, Ruthardt[13] reported that TaS_2 could be dispersed in N-methylformamide (NMF) by vigorous shaking at about 200°. Geballe's group repeated this and also found sonication to be effective. In our hands NMF "out of the bottle" was effective using the sonication method and the following were not:

H_2O	formamide
EtOH	dimethylformamide
DMSO	N-methylacetamide
triethylamine	formanalide
$CHCl_3$	N-cyclohexylamide

Freshly distilled NMF was also found to be ineffective. The addition of a small amount of methyl amine restored the ability of distilled NMF to disperse TaS_2. One equivalent (based on TaS_2)

of n-propylamine was also effective with NMF, as was n-propylamine in N-methylacetamide. Diethylamine did not yield dispersions with NMF or DMF. Large excesses of n-propylamine caused aggregation of TaS_2 and/or prevented dispersion. While this method is not as universal as could be hoped, NMF is a useful solvent. The most vigorous conditions employed were 5 min. at ambient temperature. More forcing conditions may allow use of other solvents. Careful removal of dimethylamine from DMF may also be important. The dispersions produced by this method contain neutral $(TaS_2)_x$ units rather than $(TaS_2^-H^+)_x$ which is reducing. Water may be eliminated completely. Visible spectra of these dispersions are almost identical to the aqueous dispersions with a broad peak at 395 nm[11]. Tetra-o-aminophenylporphyrin spectra were unchanged on addition of TaS_2-NMF dispersion.

b. Experimental. Electrochemistry was performed on "home built" instruments at Anson's group (Caltech) and Taube's group (Stanford). A Varian E-100 was used to measure ESR. TaS_2 was synthesized from the elements and crystallized by I_2 vapor transport[12]. $NbSe_2$ crystals were provided by the Geballe group. Intercalation of H^+ and preparation of aqueous dispersions followed Murphy et al[10,11] as did attempts to displace H^+ with larger cations. Intercalation of neutral compounds was attempted from benzene at reflux. For the porphyrins and Wurster's salt both pre-intercalation of NH_3 and intercalation from liquid NH_3 failed.

TaS_2-NMR dispersion. 35 µl n-propylamine (.425 mmol) was added to 100 mg 2H-TaS_2 powder (.408 mmol) in 5 ml NMF. This mixture was sonicated by holding the reaction vessel in an active region of a 1 qt. ultrasonic cleaning bath for 30-60 seconds. A red-brown suspension resulted having very little solid residue. This could be diluted with NMF, DMF, H_2O and EtOH without coagulation.

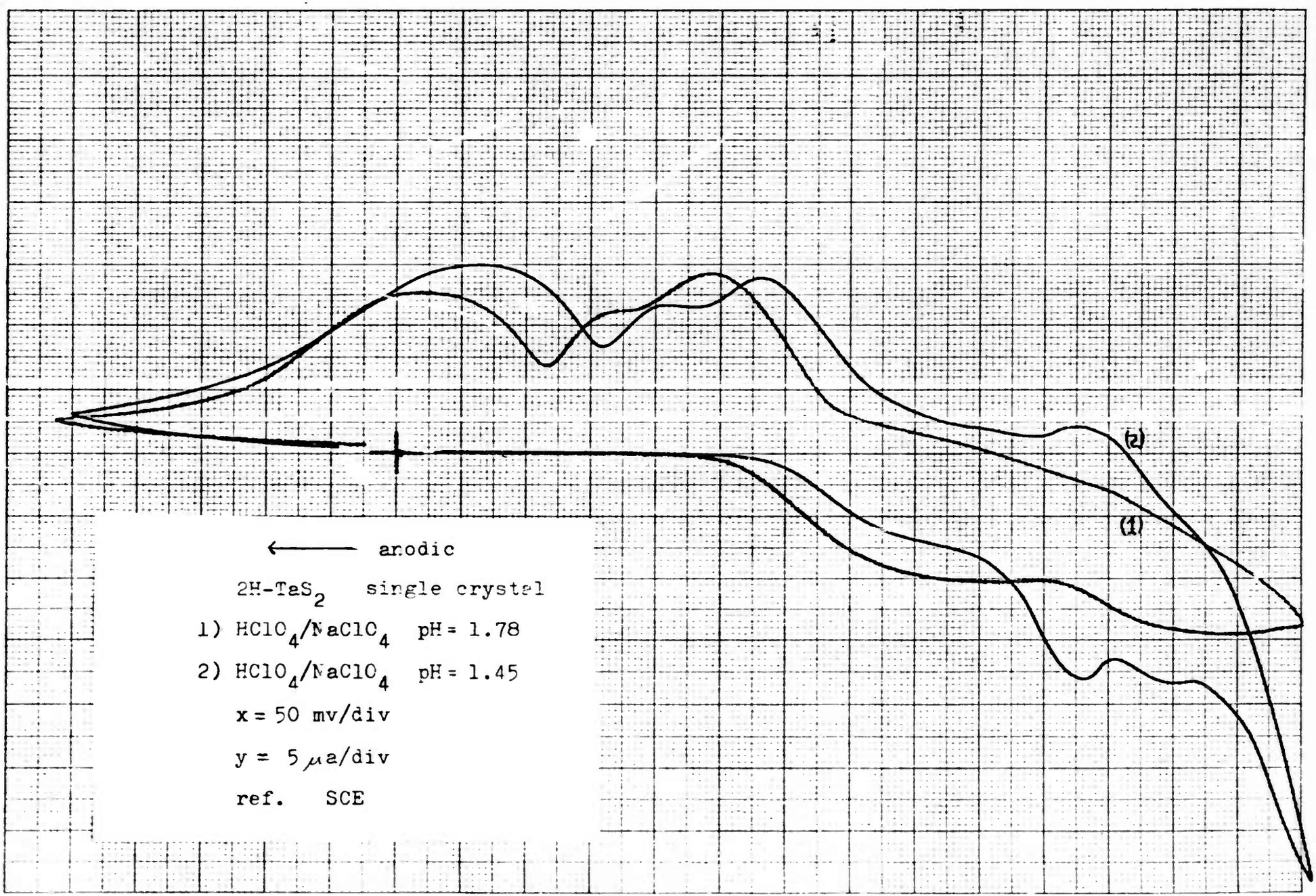
(2)
(1)
← anodic
2H-TaS2 single crystal
1) HClO4/NaClO4 pH = 1.78
2) HClO4/NaClO4 pH = 1.45
x = 50 mv/div
y = 5 μa/div
ref. SCE

72a

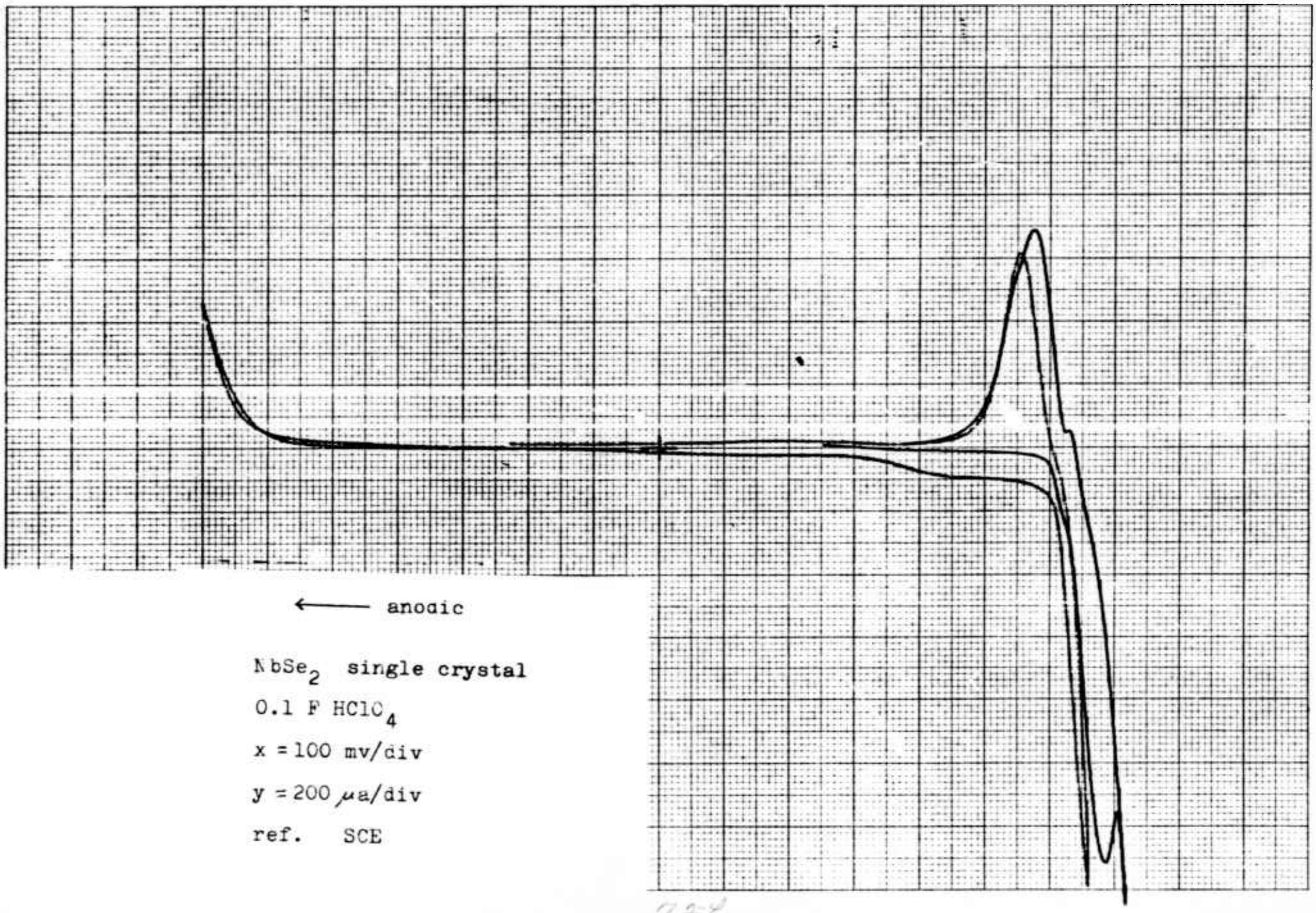

← anodic

$NbSe_2$ single crystal

0.1 F $HClO_4$

x = 100 mv/div

y = 200 μa/div

ref. SCE

-72-

c. References

(1) H. Arai and J. Halpern, Chem. Comm., 1571 (1971).

(2) J. P. Collman, Accts. Chem. Res., 1, 136 (1968).

(3) C. K. Brown and G. Wilkinson, J. Chem. Soc., A, 2753 (1970).

(4) K. G. Allum, R. D. Hancock, I. V. Howell, R. C. Pitkethly, and P. J. Robinson, J. Organomet. Chem., 87, 189, 202 (1975).

(5) G. O. Evans, C. U. Pittman, Jr., R. McMillan, R. T. Beach, and R. Jones, J. Organomet. Chem., 67, 295 (1974).

(6) C. U. Pittman, Jr., L. R. Smith, and R. M. Hanes, J. Amer. Chem. Soc., 97, 1742 (1975).

(7) C. U. Pittman, Jr. and L. R. Smith, J. Amer. Chem. Soc., 97, 1749 (1975).

(8) S. F. Meyer, R. E. Howard, G. R. Stewart, J. V. Acrivos, and T. H. Geballe, J. Chem. Phys., 62, 4411 (1975), and references therein.

(9) M. S. Whittingham, Chem. Comm., 328 (1974).

(10) D. W. Murphy, F. J. DiSalvo, G. W. Hull, Jr., J. V. Waszczak, S. F. Meyer, G. R. Stewart, S. Early, J. V. Acrivos, and T. H. Geballe, J. Chem. Phys., 62, 967 (1975).

(11) D. W. Murphy and G. W. Hull, Jr., J. Chem. Phys., 62, 973 (1975).

(12) F. J. DiSalvo, Ph.D. Thesis, Stanford University (1971).

(13) R. Ruthardt, Ph.D. Thesis, Ludwig Maximilians University (1968).

(14) B. R. James and F. T. T. Ng, J. Chem. Soc. Dalton, 355, 1321 (1972).

3. Chelating Silica Bonded Ligands

K. Neuberg

For reasons summarized in the preceding section[1] we have been interested in the preparation and behavior of transition metal complexes immobilized on various solid supports. During the past several years we have most often used silica gel as the support material for our work. Recent developments with these silica-supported systems are described below.

Silica-Supported Metal Complexes

a. Introduction

In order to firmly attach metal complexes to the silica surface the surface must first be modified so as to contain strong metal-coordinating groups. One way in which this can be done is to treat the free surface silanols (≡SiOH) with a bifunctional organosilicon compound of type A (eg, $(EtO)_3Si(CH_2)_3NH_2$) as in reaction 1(a). An alternate route shown in reaction 1(b) utilizes

Y = Cl, OR

R' = alkyl, aryl or R' = Y

L = PPh_2, NH_2, etc.

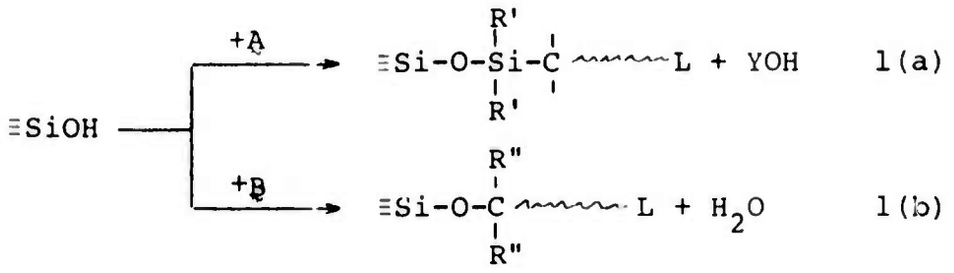

a bifunctional compound of type B possessing both an hydroxyl group and a liganding group. Both methods are characterized by a single-step functionalization of the silica. A solid-phase synthesis approach, i.e., one in which a ligand precursor is first attached and later converted in one or more steps to the desired ligand, is to be avoided as it introduces uncertainties about the exact nature of the surface species. Of the two schemes 1(a) is preferred due to the strength of the Si-O-Si linkage and to the greater hydrolytic and thermal stability of the Si-C bond relative to the Si-O-C unit.

Both of the above methods have been used by this group to prepare modified silica gels containing tertiary phosphines. These materials were then treated with rhodium compounds (eq. 2) to give supported complexes which catalyzed the hydrogenation of olefins at 25°C, 1 atm H_2[2,3]. The exact structures of these catalysts

$$\equiv Si\text{-}O\text{-}Si(CH_3)_2CH_2CH_2PPh_2 + [Rh(C_8H_{12})Cl]_2 \xrightarrow[r.t., N_2]{C_6H_6} \quad (2)$$

$$\text{"}\equiv Si\text{-}O\text{-}Si(CH_3)_2(CH_2)_2PPh_2Rh(C_8H_{12})Cl\text{"}$$

could not be determined due to the inapplicability of conventional analytical techniques for the identification of surface species.

Electron micrograph pictures did, however, reveal some interesting information[3]. Metal particles could be observed in

catalysts prepared without the rigorous exclusion of air and moisture. This was true of samples taken both before and after use in an hydrogenation. In contrast, few if any crystallites were found in catalysts prepared using high vacuum and dry-box techniques. The fact that the former catalysts were always much less active than the latter is believed to be related to this absence of metal particles.

b. Bisphosphine Bidentate Ligand--Si-O-Si-C Linkage

It appeared likely that the monodentate phosphine ligands were not effectively immobilizing the rhodium atoms as discrete organometallic complexes and that a possible monolayer of water on the silica surface provided a medium through which metal atoms could migrate and form crystallites. A possible solution to this mobility problem was seen in the use of bidentate ligands which should hold the metal more strongly. Bis(tertiary-phosphine)organosilicon compounds of type C were therefore desired.

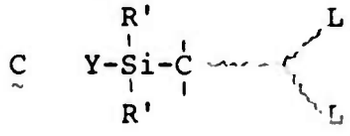

The preparation of such compounds poses quite a synthetic challenge owing to the following points: (1) only a few methods are known for forming Si-C bonds; the two most general are Grignard reactions (eq. 3) and hydrosilylations of olefins (eq. 4);

$$RMgX + R'_3SiY \longrightarrow R'_3SiR + YMgX \qquad (3)$$

Y = Cl, Br, OR, H

$$\text{>C=C<} + R'_3SiH \longrightarrow -\overset{|}{\underset{R'_3Si}{C}} - \overset{|}{\underset{H}{C}}- \qquad (4)$$

(2) at least one easily cleaved group (Cl, OR) must be present on the silicon atom for attachment to the silica; this limits the types of operations which can be carried out once the silicon has been introduced; (3) tertiary phosphines are reported to be easily oxidized to the phosphine oxide (R_3PO); therefore, reactions must be carried out in the absence of oxygen.

Several different synthetic schemes were investigated before a successful route (Figure 1) was found[4]. The bisphosphine IV was then bound to silica and finally complexed with rhodium. The supported catalyst obtained functioned in the manner expected for an organometallic complex, but not for metallic rhodium. In addition, it possessed some unusual properties which we were interested in studying in more detail. However, having demonstrated the effectiveness of this bidentate ligand in immobilizing the metal and having found indications of some interesting behavior, it was decided that it would be worthwhile at this stage to first improve the ligand synthesis, as it contained some unsatisfactory steps.

For example, the hydrosilylation reaction with trichlorosilane was done at 250° in a sealed tube. This is inconvenient

and also may have resulted in some decomposition of either I or II, as tosylates in general are known to be sensitive to temperature. Furthermore, due to the extreme hydrolytic instability of Si-Cl bonds, compound I could not be purified, or even well-characterized, before it was ethanolyzed to give III. The chloride ions liberated in this reaction may well have displaced some of the tosyl groups, affording a mixture of products. Ordinarily this would not present

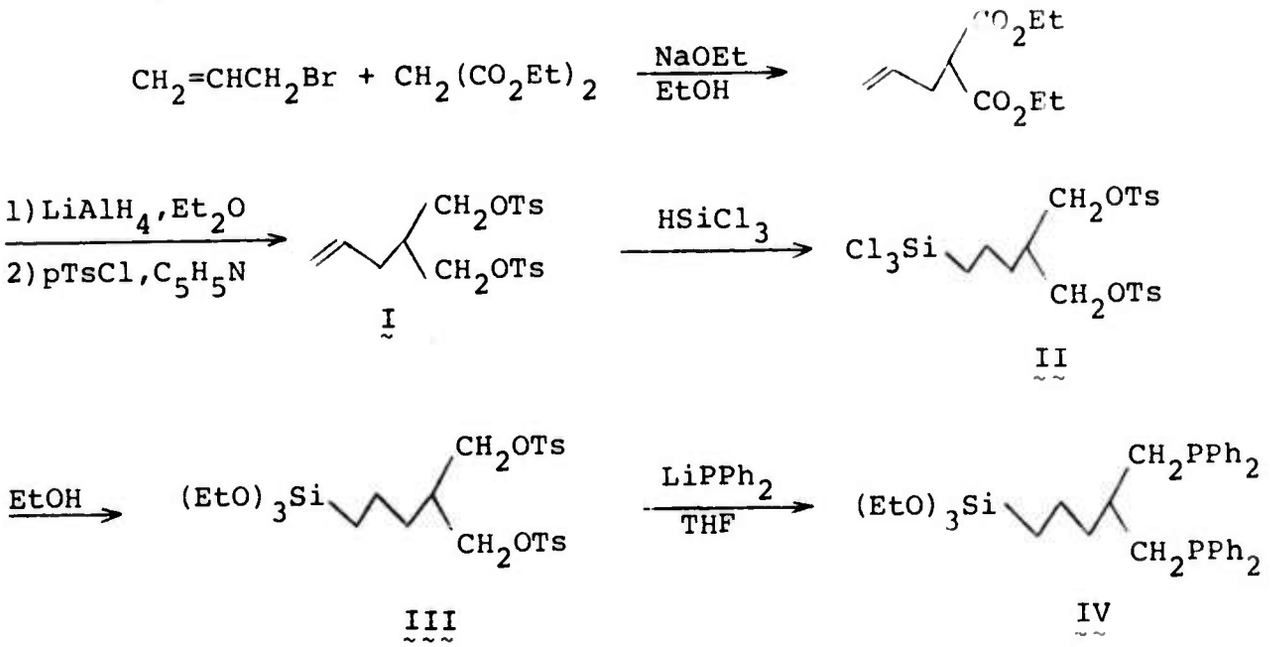

Figure 1

a serious problem, but standard purification techniques could not be used with III just as they could not be used with II. The oil III decomposed during an attempt to distill it. Chromatography was avoided as it was believed that the siloxy groups would react

with both silica and alumina adsorbents. Compound IV was also an undistillable oil which was never obtained in a pure form. One of the projects we have been working on during the last year has been the development of new methods of preparing and purifying ligand IV and its precursor III.

The crystalline compound I was prepared as already described[4] and then alternate methods of hydrosilylating the olefin were investigated. The addition of hydrosilanes to substituted olefins have been accomplished by the use of elevated temperatures, by irradiation with UV light, and by metal catalysis. The inconvenience and unsuitability of the first of these methods, as discussed above, and the repeated failures using UV irradiation[4] left the last method as the only reasonable approach. Metal-catalyzed hydrosilylations appeared attractive in that (1) the catalysts were readily available in our laboratory; (2) these reactions generally take place under relatively mild conditions; (3) additions using $(EtO)_3SiH$ were known and offered the possibility of preparing compound III directly from I.

Because separation and purification of III was expected to be difficult on the basis of the earlier work, it was clear that the best synthetic method would be one which had few side reactions and whose by-products could be easily removed. The homogeneous catalysts $RhCl(PPh_3)_3$ and $Rh_2(CO)_4Cl_2$ were used with some success in several hydrosilylations in which the metal concentration, reaction

temperature, and reaction time were varied. But a heterogeneously catalyzed reaction using Pt-on-charcoal was superior in meeting the above requirements. First of all, the catalyst could be easily and completely removed at the end of the reaction. Secondly, the reaction was very clean. Using about 3-4% by weight (of olefin) of Pt/C, silane/olefin = 2, and refluxing toluene, the reaction appeared to be almost quantitative in 12-16 hrs. The "crude" product obtained after removal of catalyst and solvent contained a very small amount of a compound whose R_f value in tlc was apparently the same as that of the starting material. However, there was not evidence for a vinyl group by nmr or ir, and, therefore, this contaminant may not in fact be starting material. In addition to this minor impurity, the "crude" product contained a larger amount of a material with $R_f = 0$, which is undoubtedly mainly excess $HSi(OEt)_3$ and could be partially removed by heating under vacuum.

Although the purity of III, as ascertained by the excellent nmr and by tlc, was certainly sufficient for use in the next reaction, two attempts were made to bulb-to-bulb distill the oil. These failed due to decomposition, in agreement with earlier observations[4]. A successful method for purifying III was discovered when column chromatography on silica gel was tried on a small amount of III. Such chromatography had formerly been avoided because the product was expected to remain on the column or to be decomposed

by the adsorbent. In fact, the siloxy-tosylate chromatographed well with $CHCl_3$ as the eluent. We recently found that this purification process can be simplified; by merely stirring the "crude" product with silica gel for a short time, the impurities with $R_f = 0$ in tlc are completely removed. The contaminant which moves with the same R_f value as the starting material is still present after this treatment, but it is only a trace impurity on the basis of the analysis: calcd: %C, 53.03%, %H, 5.85%; obsd: %C, 52.72%; %H, 6.77%.

Platinum-on-charcoal also catalyzed a hydrosilylation using $(CH_3)_2(EtO)SiH$ (eq. 5), although under the conditions used this

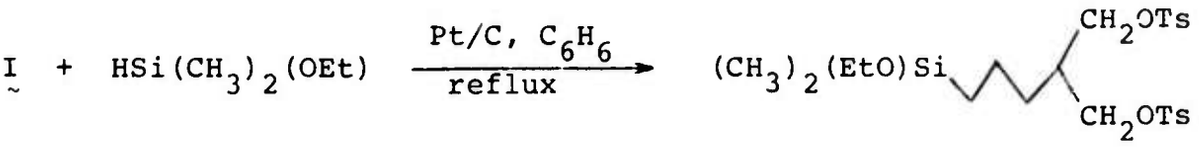

(5)

reaction was much slower and not as clean as the one just discussed. It had been hoped that substitution of two of the ethoxy groups of III with methyl groups would result in a more volatile compound. Compound V, however, also turned out to be an oil which decomposed during an attempt to distill it. Preliminary efforts to crystallize V by the general methods used for tosylates[5] also failed. The compound appeared to be a solid at ≈-60-78°C, but upon warming once more became an oil. More graduate cooling and other techniques may be more successful. Even if they are not, low temperature filtration is preferable to tedious column chromatography as a purification method for this compound.

Having found ways to prepare and purify compound III the next stage is to carry out the phosphination reaction and develop methods for isolating IV in pure form. The single phosphination reaction attempted to date employed $NaPPh_2$ in dioxane/THF; the only identifiable product was $HPPh_2$. In the next experiments $LiPPh_2$ and $KPPh_2$ will be used.

It should be noted than an alternate route to IV (Figure 2) was tried early on[4] but was abandoned when VI could not be hydrosilylated. A recent report in the literature[6] describing the reaction of $p\text{-}Ph_2PC_6H_4(CH_2)_2CH_2{=}CH_2$ and $HSiCl_3$ using UV irradiation prompted us to reinvestiage this problem. Irradiation of a mildly refluxing solution of $HSiCl_3$ and VI for 41 hrs., followed by ethanolysis, yielded the desired adduct in an impure state, but free of unreacted olefin by nmr. The reaction needs to be repeated using more care (IV is easily oxidized) and the overall yield calculated to determine whether the two step sequence I→VI→IV is competititve with I→III→IV.

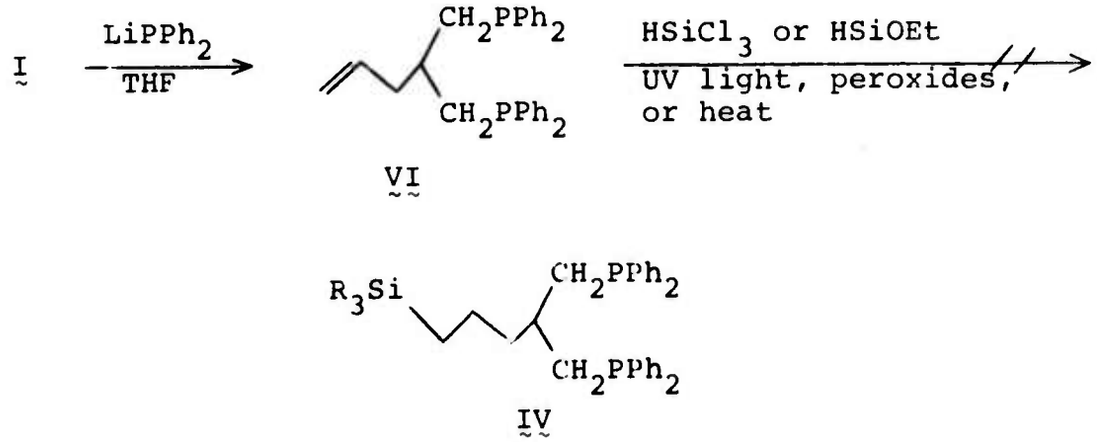

Figure 2

c. Nitrogen, Phosphorous Bidentate Ligand--Si-O-Si-C Linkage

In the last year we have also been interested in an entirely different bidentate ligand, the silicon analog VII of the known[7] ligand VIII, o-(diphenylphosphino)-N,N-dimethylaniline ("PN"). Two schemes for the preparation of VIII are shown in Figure 3, where the solid lines indicate the steps which have already been carried out. Step a is likely to be complicated by polymerization

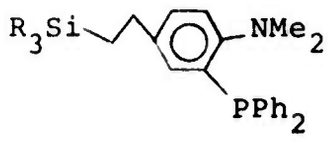

VII

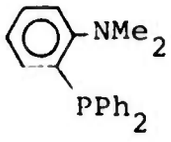

VIII

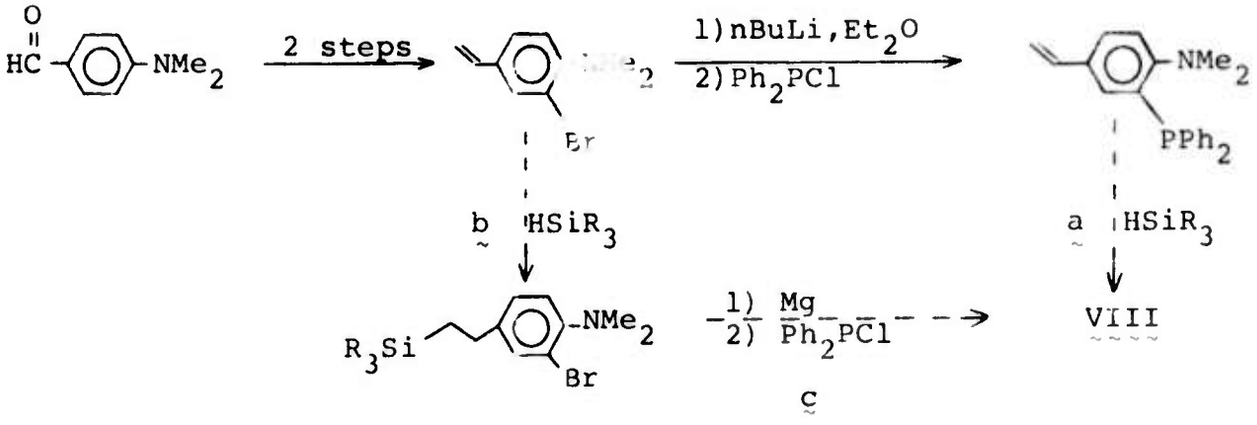

Figure 3

of the styrene derivative during free radical hydrosilylations using UV light or peroxides; metal catalysis will probably be ineffective here due to catalyst poisoning by the phosphine. The better route may involve steps b and c.

The model compound VIII was synthesized as described in the literature[7] and treated with the rhodium(I)-olefin complexes often used in this laboratory for the in situ generation of a hydrogenation catalyst (eq. 6). A PN ligand/Rh atom ratio of 1.0 was used to avoid formation of the catalytically inactive species $Rh(PN)_2Cl$. The active catalyst or its precursor would be expected to have the general structure shown.

$$[RhL'_2Cl]_2 \quad (L' = C_2H_4,\ C_8H_{14}) \quad + \quad PN \xrightarrow{C_6H_6} \quad \text{(P, N, Cl, L on Rh)} \qquad (6)$$

L = solvent or olefin

Both the ethylene dimer and the cyclooctene dimer generated catalysts which hydrogenated only a small amount of cyclooctene and then stopped. Addition of PPh_3 to break up possible dimers of the type $(PN)Rh\langle^{Cl}_{Cl}\rangle Rh(PN)$ had little or no effect. The catalytic activity of $Rh(C_5H_8O_2)(PN)$ had been previously reported[7]. Although it would appear that our usual method for forming the catalyst in situ does not apply here, interpretation of the results are complicated by the facts that (1) the ethylene dimer was very unstable, sometimes decomposing under H_2 before the PN solution was injected into the hydrogenation vessel (2) the cyclooctene dimer used was old and could have been partially decomposed. Work with the PN ligand and the silicon analog will continue.

d. Bisphosphine Bidentate Ligand--Si-O-C Linkage

A third ligand which has attracted our attention lately is the chiral bisphosphine IX, 2,3-O-isopropylidene-2,3-dihydroxy-1,4-bis(dipehnylphosphino)butane ("DIOP"). Soluble rhodium complexes prepared in situ from IX and rhodium(I)-olefin complexes as in eq. 6 have catalyzed asymmetric hydrogenations[8,9] and hydroformylations[10] of olefins and asymmetric hydro-

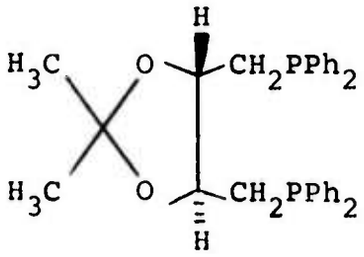

IX

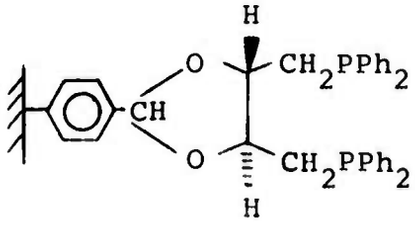

X

silations[11,12,13] of carbonyl compounds. In 1974 Kagan and coworkers attached DIOP to polystyrene giving X. An insoluble rhodium catalyst prepared from this resin was less efficient than the homogeneous analog for asymmetric hydrogenations, but the two systems were comparable in their ability to catalyze asymmetric hydrosilylations. Part of the inactivity of the supported catalyst for hydrogenations was attributed to the necessity of using polar cosolvents like ethanol to solubilize the most interesting substrates, multifunctional olefins like XI which are amino acid precursors. In C_6H_6/EtOH solvent systems

the polystyrene resin contracted strongly making the catalyst inaccessible.

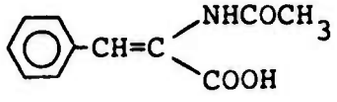

XI

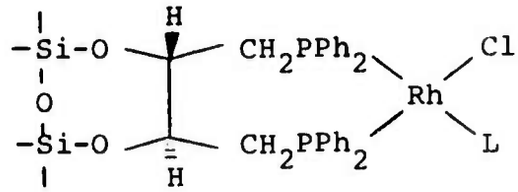

XII

Because of silica's rigid structure this support does not have the swelling/contracting properties of an organic polymer. Therefore, a DIOP-Rh complex bound to silica as in XII should be able to function in the presence of most polar solvents. Possible exceptions might be hydroxylic solvents like ethanol which might cleave the ligand from the surface at the relatively weak Si-O-C linkage.

Aside from its potential use in the asymmetric hydrogenation of olefins like XI, the silica-DIOP-Rh material XII is interesting because it will provide direct information about the nature of the catalytically active species in silica-supported systems. If optically active products are formed using XII one could conclude that the catalyst operates in the form of a discrete complex. The formation of optically inactive products would be suggestive of a metallic rhodium catalyst.

We have synthesized (-)-DIOP from tartaric acid in six steps as described in the literature[11], attached the ligand to

silica using the techniques developed in this lab[3], and finally complexed it with $Rh_2(C_8H_{14})_4Cl_2$ as in eq. 6 to give a light tan material containing 2.15% Rh. The hydrogenation of cyclooctene (1 atm H_2, 25° C, C_6H_6) with this catalyst was rather slow, only a small amount of cyclooctane being formed in 4 hrs. After reaction overnight a substantial amount of C_8H_{16} was present and possibly cyclohexane to the extent of 0.1% or less. The reaction mixture at this time may have been grayer than it was in the beginning, a color change which in the past[2,3] has been an indication that metal particles have formed. It would be unsafe to draw too many conclusions from this preliminary experiment, however, as leaks were detected in the hydrogenation line and O_2 may have been admitted to the system. A detailed study of catalyst XII is planned.

e. References

(1) M. Marrocco, Research Report, June, 1975.

(2) M. Takeda, Research Report, September, 1973.

(3) M. Marrocco, Research Report, October, 1973.

(4) D. N. Marquardt, Ph.D. Thesis, Stanford University, May, 1974.

(5) L. F. Fieser and M. Fieser, Reagents for Organic Synthesis, John Wiley and Sons, N.Y., 1967, p. 1180.

(6) G. Allum, et al., J. Organomet. Chem., 87, 203 (1975).

(7) T. R. Rauchfuss and D. M. Roundhill, J. Amer. Chem. Soc., 96, 3098 (1974).

(8) H. B. Kagan and T. P. Dang, ibid., 94, 5429 (1972).

(9) M. Tanaka, et al., Chem. Lett., 137 (1974).

(10) R. Stern, A. Hirschauer, and L. Sajus, Tet. Lett., 3247 (1973).

(11) W. Dumont, J. C. Poulin, T. P. Dang, and H. B. Kagan, J. Amer. Chem. Soc., 95, 8295 (1973).

(12) R. J. P. Corriu and J. J. E. Moreau, J. Organomet. Chem., 64, C51 (1974).

(13) I. Ojima and Y. Nagai, Chem. Lett., 191 (1975).

B. Preparation of Fine Particles

W. A. Little and J. W. Brill

During the past several months, work was continued in developing an electron energy loss analyzer for studying plasmon effects in metals. We hope to incorporate an analyzer of the type we are using in an electron microscope to examine plasma resonance in single fine metal particles. The analyzer we are using is of the type developed by Boersch [Z. Physik 139, 115 (1954)]; we found that the proper operation of such an analyzer depends critically on the spacing and sizes of its apertures. We are using electron guns with oxide cathodes; considerable time has been spent stabilizing the emission of these guns. Our system now is capable of a resolution of 3/10 volts and is sufficiently sensitive to detect aluminum films of $<<$ 100 Å and collodion films of 100 - 200 Å. However our collection efficiency falls off quickly with film thickness so that films of thickness $\gtrsim 10^{-7}$ g/cm^2 result in very poor signal to noise. We are trying to improve this situation without sacrificing resolution. To date, energy loss spectra have been taken in Magnesium, Aluminum, carbon, and collodion, in all cases agreeing with published results.

We have attempted to take spectra of $(SN)_x$ and TaS_2 (2H phase). We have not been able to prepare satisfactory films of these substances. Work on resonance effects in aluminum - collodion sandwiches is also underway.

V. DEVELOPMENT OF ELEVATED TEMPERATURES

ELECTROCRYSTALLIZATION TECHNIQUES

R. S. Feigelson

Director, Crystal Technology
Center for Materials Research

and

R. A. Huggins

Professor of Materials Science
and Engineering

A. Introduction

The majority of work reported in the literature on electrochemical crystallization has been concerned with the synthesis of various compounds, primarily of the transition elements and the preparation of metallic coatings for commercial applications. Very little effort, however, has been expended on the development of a sufficiently sophisticated understanding of the principles involved in the technique to allow adequate control of the nucleation and growth processes necessary for the production of useful bulk samples including single crystals of a wide range of materials. In order to achieve this level of control, it is necessary to understand how to produce and maintain the appropriate thermodynamic and kinetic conditions at the growth interface during the electrocrystallization process. It is in this direction that the major emphasis of this program is oriented. One of the outgrowths of this effort will be the ability to produce material continuously including single crystals by refined electrochemical crystallization techniques.

Attention is also being given to the development of the electrochemical conditions necessary for the production of a group of specific materials of special interest. These include intermetallic niobium compounds with high superconducting transition temperatures, high melting point boride compounds with unusual hardness and good electron emissivities, and other materials of interest because of their potential technological use as optical materials or mixed conductors in new types of battery systems.

During this report period, significant achievements have been made. Large single crystals of Na_xWO_3 have been produced by the electrochemical crystallization method under controlled conditions using molten tungstate baths and a Czochralski-like growth technique. The Electrochemical Czochralski Technique (ECT) has now been well characterized in this study. Growth parameters can be pre-adjusted

(based on a simple theoretical model) so as to yield a richly effective automatic diameter control. The influence of seed orientation, temperature fluctuation and crystal rotation rates on growth kinetics has been determined.

The superconducting phase Nb_3Ge has been synthesized by electrolysis of a molten salt bath.

A system capable of reproducibly growing LaB_6 single crystals from molten salt baths has been developed and crystallites up to 4 mm on a side have been produced.

Each of these programs will be discussed separately in the following sections.

B. Investigation of the LaB_6 System

I. V. Zubeck and P. A. Pettit

1. Introduction

Very little previous effort has gone into the development of a sufficiently sophisticated understanding of the principles involved in electro-crystallization to allow the production of useful bulk samples and single crystals. The emphasis of this section of the program has been to understand how to produce and maintain the thermodynamic and electrochemical conditions necessary for morphology control.

During the first phase of the program, techniques were developed which allowed the growth of small crystals of LaB_6 from a molten oxyfluoride bath on gold electrodes. From these early experiments the effect of process parameters on morphological stability, nucleation rate, and deposition efficiency were extensively studied. The need for more sophisticated processing and control equipment was recognized as an important requirement for the attainment of reproducible results.

During the past twelve months a system has been developed which allows accurate and reproducible control of growth parameters for periods greater than 300 hours. Growth of the lanthanum hexaboride system is now easily controlled, and clusters of crystallites containing individual crystals 4 mm on a side are now routinely produced. Seeded growth of the compound has begun. The growth mechanism as well as the interrelationship among growth parameters is now well understood.

The experience gained in the course of the LaB_6 program is directly applicable to other synthesis programs. The range of cell materials compatible with molten salt systems has been explored. The necessary processing and control equipment has been assembled, and the effects of cell parameters such as voltage, temperature and current density are understood. Having this information eliminates the need for much preliminary exploration in other deposition programs.

An investigation of the electrochemical synthesis of ScB_2, which is of current research interest, was begun recently. Its deposition from oxide and fluoride baths is being explored and an analysis of initial deposits from these baths is currently underway. Electrodeposition of some sulfides is planned for the near future. Very little literature exists on the electrodeposition of sulfides or on any of the II-VI materials. FeS is currently an important material in battery research and the II-VI materials including CdS are of interest to the semiconductor industry.

2. Experimental Results

Large crystals of LaB_6 4 mm on a side are now routinely produced using experimental equipment which guarantees stable growth conditions for periods greater than 300 hours. A new furnace has provided a flatter temperature gradient in the region of the crucible. Installation of a temperature controller has allowed regulation of furnace temperature to within $\pm.5°C$. A research model potentiostat-galvanostat has provided a very stable, accurate, potential source. Cell potential can now be controlled over a wide current range, and capability is provided for control and monitoring of a third reference electrode.

Sources of bath contamination within the system have been identified and are being systematically eliminated. Components of the electrolytic cell were being attacked by the highly corrosive molten oxides, and the products of this chemical attack, other metal oxides highly soluble in the molten salts, contaminated the bath. During the course of electrolysis, conductive puddles collected on the melt surface, interferring with electrolysis. Other contaminants dissolved in the melt were electrodeposited at the cathode. The electrodeposits often contained Ni from the Ni crucibles. Electrodeposits and bath puddles contained Cu from the brass flange covering the inconel electrolysis system. Nickel crucibles have been replaced by platinum and vitreous carbon. The brass flange has been coated with electrodeposited Ni. Puddles no longer accumulate

on the bath surface during electrolysis, and cathode deposits containing contaminate metals have been almost entirely eliminated. Decreases in current early in a run (~ 100 hrs) have been attributed to accumulation of O_2 within the growth system, and adequate flushing of the system with inert gas has been provided.

The interrelationships among cell potential, cell current, and electrode configuration are now well understood and have led to reproducible growth conditions. Cell potential is held constant during any given run, and cell current and resistance follow Ohm's law:

$$E = IR \qquad \text{where } R = \frac{\rho l}{A}$$

$$E = \frac{I\rho l}{A}$$

ρ = resistivity

l = distance between electrodes

A = f (cathode area, anode area)

If we assume that the resistivity ρ of a solution remains constant during a run (bath not run to depletion) then we can write

$$E = \text{constant}$$

$$\frac{E}{\rho l} = \frac{I}{A} = \text{constant}$$

Thus, operation of an electrolysis cell at constant potential E implies operation at constant cathodic current density I/A. The cell current rises during a run as deposited material increases the effective cathode area (A increases), anode area being constant. This argument also implies that for constant cell potential E and a given initial cathode area, the cathode current density used during a run can be chosen by suitable choice of anode area. If $A_1 > A_2$, then $I_1 > I_2$ by $\frac{E}{\rho l} = \frac{I}{A}$ = constant.

A nucleation study has shown that when controlled growth conditions are achieved, grain selection occurs after crystallites have nucleated. When electrodeposition begins, crystallites approximately 10 μ on a side nucleate and completely cover the cathode.

(Fig. 1) As electrodeposition continues some of the crystallites grow, crowding out others (Fig. 2) until a few larger growing crystallites remain. Under stable growing conditions, secondary nucleation does not occur, and the growth process continues uninterrupted. After a period of approximately 100 hours, a typical deposit (Fig. 3) contains cubic crystallites 1 mm on a side. If electrolysis is continued, crystallites 4 mm on a side can be obtained in a period of 300 hours. The crystals will continue to grow larger if electrolysis is continued, but the time element involved becomes prohibitive.

As electrodeposition proceeds, the cathode surface area increases. This is manifested as a rise in cell current (Fig. 4). I_o represents the initial current as measured ten minutes after the start of electrolysis. The current rises rapidly during the first few hours of a run as crystallites nucleated on the smooth substrate result in a large percentage increase in cathode area. The current rises more slowly during the remainder of a run as crystallites already nucleated continue to grow. The progress of an electrodeposition run is monitored by recording current vs time on a chart recorder. Fig. 4 shows current vs time for a typical run.

The growth mechanism operating in the electrodeposition of materials such as LaB_6 is now understood (Ref. 1-7). Individual crystallites in the deposit grow as layers approximately 1 μ in step height which form at pyramidal active centers or sources on the crystal face and spread outward in all directions from their source. At low to moderate current densities, these active centers are located at the interior of the (100) crystal faces and the layers spread outward toward the edges of the crystallites (Figs. 1, 5 and 6). As the current density is increased, the active centers (Fig. 7) shift to the corners and edges of the crystallite closest to the incoming nutrient. The growing layers spread toward the interior of the (100) crystal face. The photo in Fig. 7 was taken normal to a (100) face, the upper right hand corner of the crystallite projected slightly into the melt. At high current densities, corner growth is accentuated and the cubes become distorted. At extremely high current densities (Figs. 8, 9) the accentuated corners become

Figure 1. Small crystallites, ~10 μ on a side, showing exaggerated pyramidal structure at the face centers, 2000X.

Figure 2. LaB_6 grown on Au substrate: 100X. Light grey LaB_6 crystallites, and the two phase dark grey region the plastic sample mount.

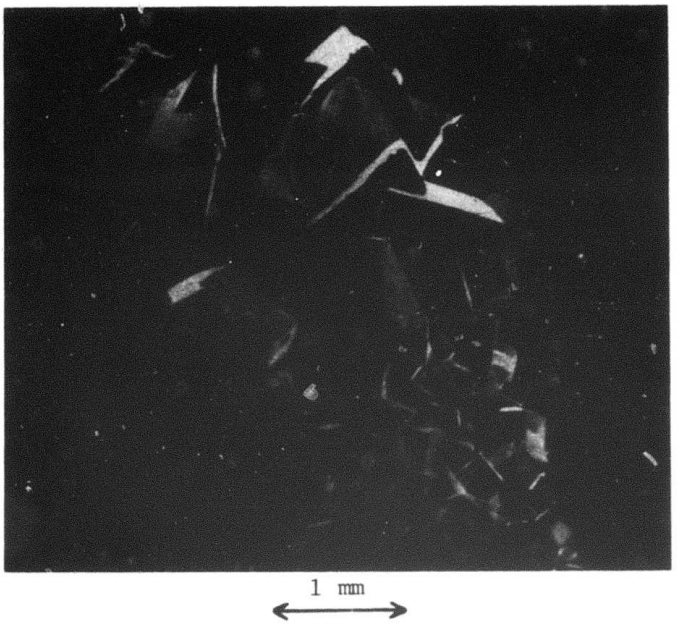

Figure 3. LaB_6 electrodeposit, 100 hrs.

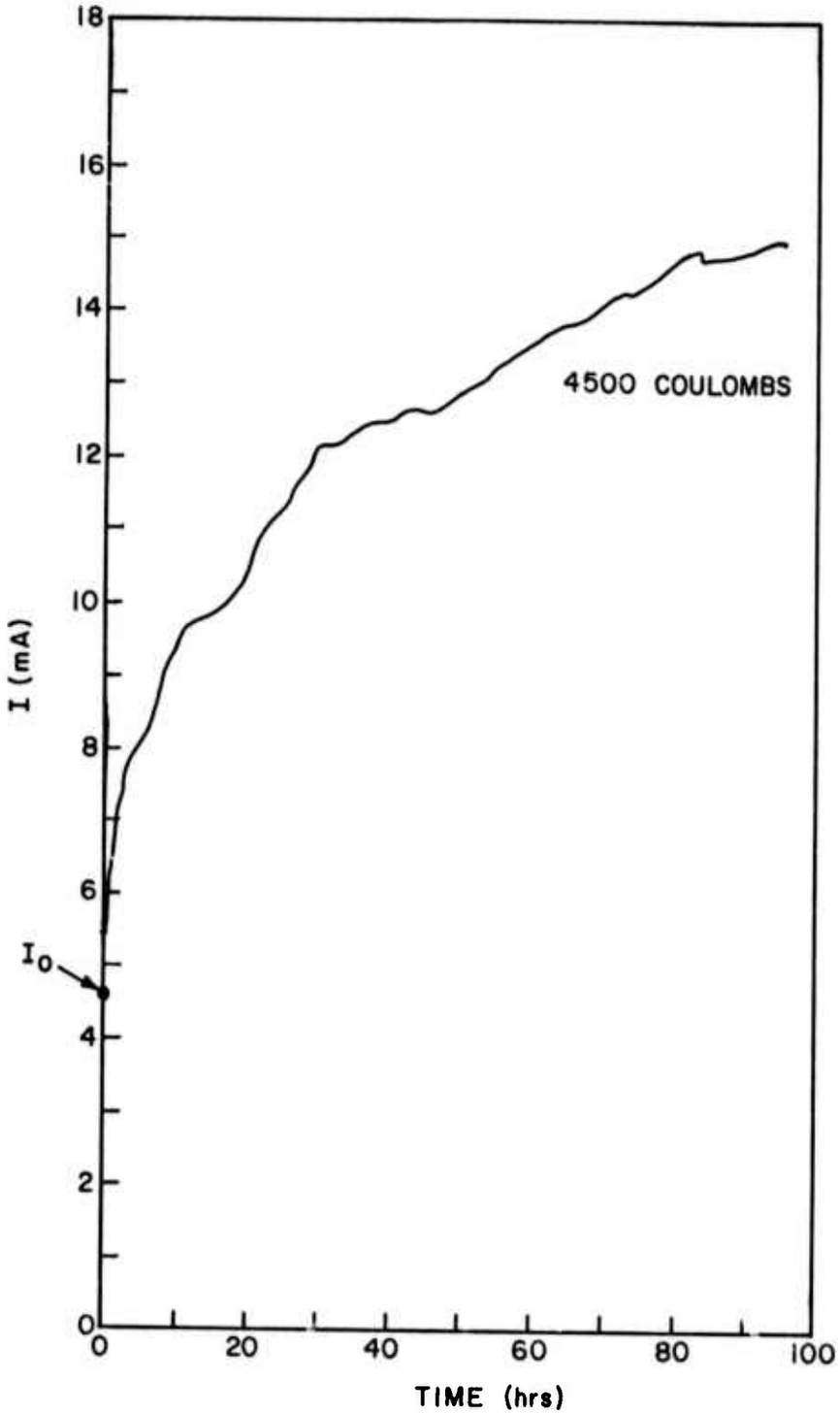

Figure 4. Current vs. time for LaB_6 growth.

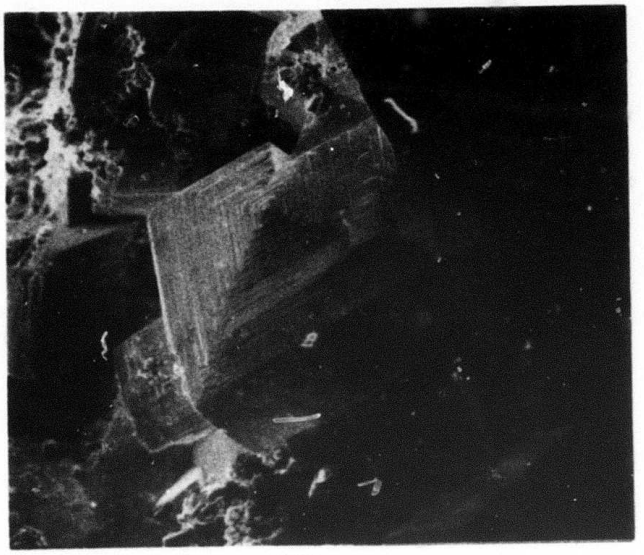

Figure 5. Pyramidal active center at interior of (100) face.

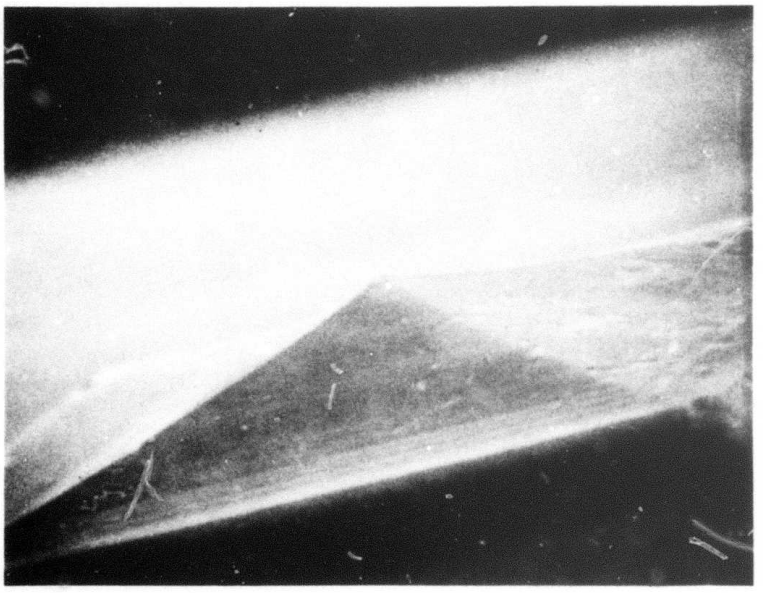

Figure 6. Pyramidal growth structure, 5000X.

Figure 7. Pyramidal active center at corner of (100) face of crystallite.

Figure 8. Dendrites along [111] direction, composed of stacked cubes, evidence of corner growth, 180X.

Figure 9. Dendrites along [111] direction, 500X.

dendrites along the [111] direction. The critical current density for growth of crystals of cubic shape appears to lie in the region of 30 mA/cm^2. The optimum current density for growth of cubic material appears to lie in the region from 15 to 25 mA/cm^2. This corresponds to a linear growth rate on the order of 10^{-6} cm/sec.

The cathode deposit which results from these growths consists of clusters (Fig. 3) of interlocking crystals which share the incoming nutrient. If electrodeposition could be carried out on a single piece of LaB_6 seed material, a cathode product of substantial dimensions could be obtained in much less time. Experiments in seeded growth are now underway, and these should provide, in the near future, a method to prepare large single crystals.

A series of runs explored electrolysis using the research model potentiostat in its overpotential control mode, in which the instrument maintains a constant potential (IR drop) between the cathode and reference electrode. A Pt wire inserted into the melt proved too unstable a reference to use for control purposes, and construction of a compartmented reference electrode was impractical due to the corrosive nature of the molten salt system in use.

3. Scandium Boride Program

In an extension of the technology developed in the lanthanum hexaboride program, a study of the electrodeposition of another boride compound, scandium diboride ScB_2, has been initiated recently. In a study preliminary to the LaB_6 program, a diboride ZrB_2, already reported in electrochemical literature, was very easily synthesized. Electrochemical synthesis of other diborides has been reported, but not yet that of scandium. ScB_2, with a melting point of 2250°C and a Knoop hardness of 2630, has a hexagonal crystal structure and is of current research interest in Mossbauer studies.

An oxide bath similar to that used for LaB_6 deposition, and a bath consisting of eutectic LiF-NaF-KF (Flinak) flux with a Sc_2O_3-B_2O_3 solute are being explored. Cathode deposits obtained at each in a

sequence of different bath compositions were evaluated. At each bath composition the current vs voltage (I-V) characteristics of the molten bath were recorded between zero and approximately three volts. Electrolysis was then performed at several selected voltages. Resulting deposits were examined by optical and/or scanning electron microscopy and analyzed by x-ray and electron microprobe analysis.

An oxide bath similar to that used for LaB_6 deposition was chosen for investigation because of its success in the deposition of many borides.[8] The proportions of the oxide bath were varied as shown in Table 1. With each successive bath the Sc:B ratio was increased in order to bring the Sc:B ratio in solution closer to that needed for deposition of the desired compound ScB_2 (1:2). The solubility of Sc_2O_3 in the oxide bath is quite low, resulting in an inconveniently high melting point for the Sc:B = 1:1.06 bath (SB 17).

Complicated multiphase electrodeposits were obtained from these oxide baths. A typical example, Fig. 10, shows such a deposit surrounding a gold cathode wire. Analysis of the cathode deposit is difficult due to the insolubility of salt inclusions and the multiphase character of the deposits. A concentrated effort toward analysis is currently in progress.

The low melting (450°C) LiF-NaF-KF eutectic (Flinak) solvent system offered the possibility of using a high ratio of Sc:B in solution while retaining a low melting point. It also allowed study of the I-V behavior of B_2O_3 and Sc_2O_3 separately in Flinak. This cannot be accomplished in the oxide bath, in which the B_2O_3, as well as taking part in the cell reaction, is also the important fluxing agent in the bath due to its low melting point (450°C). The oxide bath containing no B_2O_3 cannot be melted at temperatures within the operational range of the resistance furnaces, and the I-V behavior of the Sc_2O_3 component cannot be isolated.

The approach used with the Flinak solvent was to record the I-V characteristics of a series of concentrations of each component alone in the Flinak solvent. The two components were then combined in the Flinak solvent in concentrations determined such that at a

TABLE 1

Composition of Oxide Baths Used in Sc-B Program

	SB1		SB3		SB4		SB5		SB6		SB11		SB17	
		mole %		mole %		mole %		mole %		mole %		mole %		mole %
bath composition	Sc_2O_3	1.6	Sc_2O_3	2.2	Sc_2O_3	3.2	Sc_2O_3	1.6	Sc_2O_3	5.55	Sc_2O_3	12.0	Sc_2O_3	16.0
	B_2O_3	49.2	B_2O_3	32.6	B_2O_3	32.3	B_2O_3	24.6	B_2O_3	27.78	B_2O_3	21.33	B_2O_3	17.0
	LiF	24.6	LiF	32.6	LiF	32.3	LiF	36.9	LiF	33.3	LiF	33.33	LiF	33.3
	Li_2CO_3	24.6	Li_2CO_3	32.6	Li_2CO_3	32.3	Li_2CO_3	36.9	Li_2CO_3	33.3	Li_2CO_3	33.33	Li_2CO_3	33.3
Sc:B ratio of bath	1:31		1:15		1:10		1:15		1:5		1:1.77		1:1.06	
Solute: flux ratio of bath	1:1		1:2		1:2		1:2.8		1:2		1:2		1:2	
Deposition temperature °C	840°		850°		855°		810°		810°		850°		-	

Figure 10. Multiphase electrodeposit from oxide bath.

chosen cell voltage the fluxes of the two ions (Sc^{+3}, B^{+3}) arriving at the cathode would be in the Sc:B ratio of the desired compound ScB_2, approximately 1:2. Baths composed of 1, 5, and 10 mole % B_2O_3 alone in Flinak and 1 and 5 mole % Sc_2O_3 alone in Flinak were prepared, and the I-V characteristics of each was recorded. The I-V curves appear in Figs. 11 - 15.

An I-V curve is obtained by applying a ramped voltage across the anode and cathode of the electrolysis cell. Arrows pointing up and down (see Figs. 11 - 15) indicate increasing and decreasing ramp voltages. The horizontal separation between the increasing and decreasing portions of the curves is a function of ramp speed and concentration of the specie being deposited. The decomposition potential of a bath containing a single solute specie is estimated by determining an approximate average (dotted line) of the increasing and decreasing portions of an I-V curve. The average is extrapolated to zero current, the intercept on the voltage axis being taken as an approximate value of E_d. The values of E_d for the B_2O_3 baths increase with decreasing solute content of the baths, in accordance with electrochemical theory. Conclusions concerning the I-V curves for Sc_2O_3 in Flinak are more difficult to draw, but it is clear that the I-V curve has shifted left with increasing Sc_2O_3 content as expected, implying an increase in E_d with decreasing solute content. I-V information for 10 mole % Sc_2O_3 in Flinak was not obtained due to the unexpectedly high melting point of this composition. In addition to E_d information, the I-V curves provide an estimate of the amount of current to be expected at a given voltage.

The decomposition potential of Sc_2O_3 in Flinak (see I-V curves) is approximately 300 mV higher than E_d for B_2O_3 in Flinak. Combining the two components in Flinak does not alter their E_d values, and therefore at a cell potential large enough to decompose the Sc_2O_3 considerable current flows due to B_2O_3 decomposition. Due to the unexpectedly low solubility of Sc_2O_3 in Flinak, baths containing large amounts of Sc_2O_3 could not be used. The B_2O_3 composition of the baths was therefore kept very low so that at voltages above the

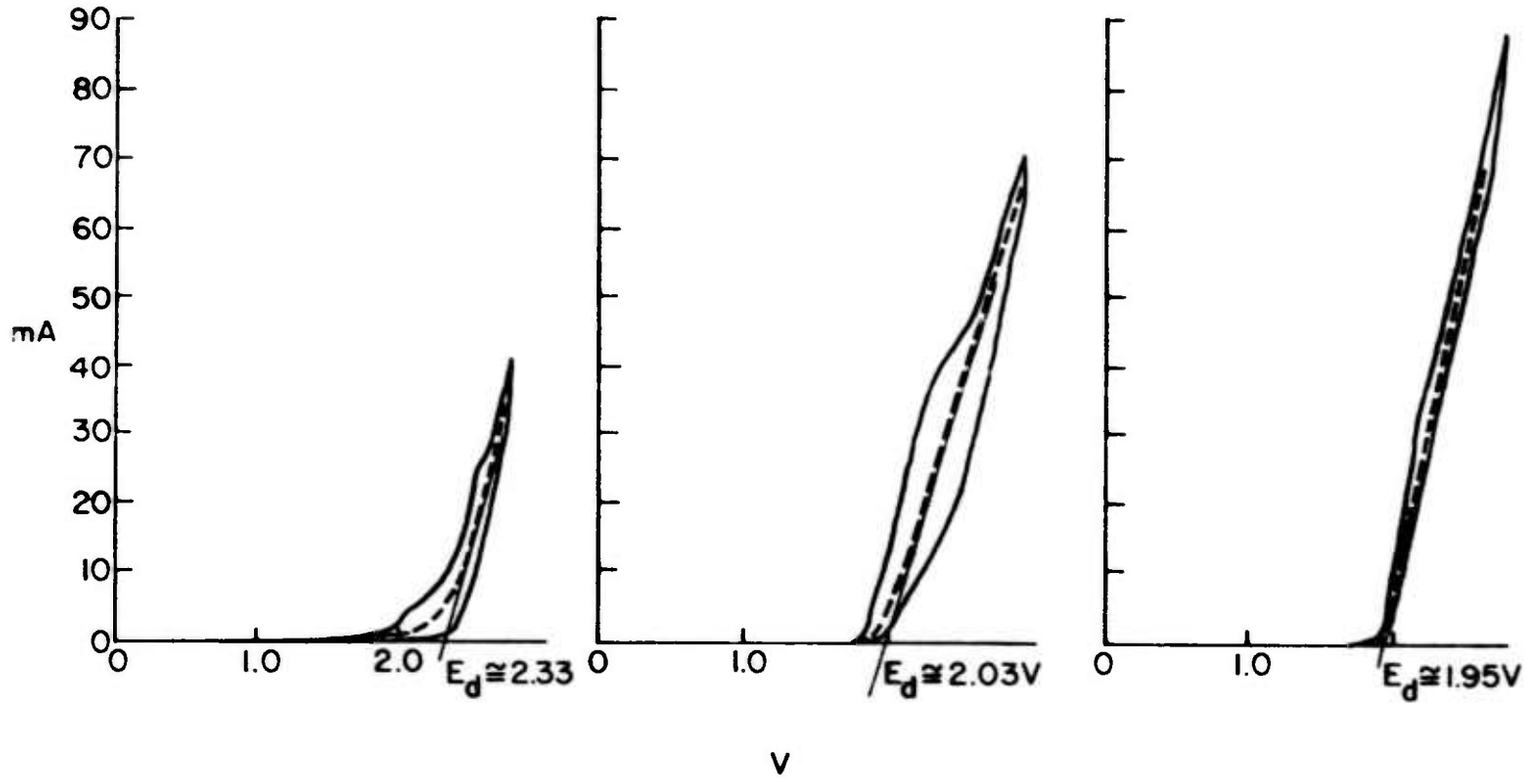

Figure 11. Figure 12. Figure 13.

Figure 11. Current vs Voltage, 1.0 mole % B_2O_3 in Flinak, 750°C.

Figure 12. Current vs Voltage, 5.0 mole % B_2O_3 in Flinak, 750°C.

Figure 13. Current vs Voltage, 10.0 mole % B_2O_3 in Flinak, 750°C.

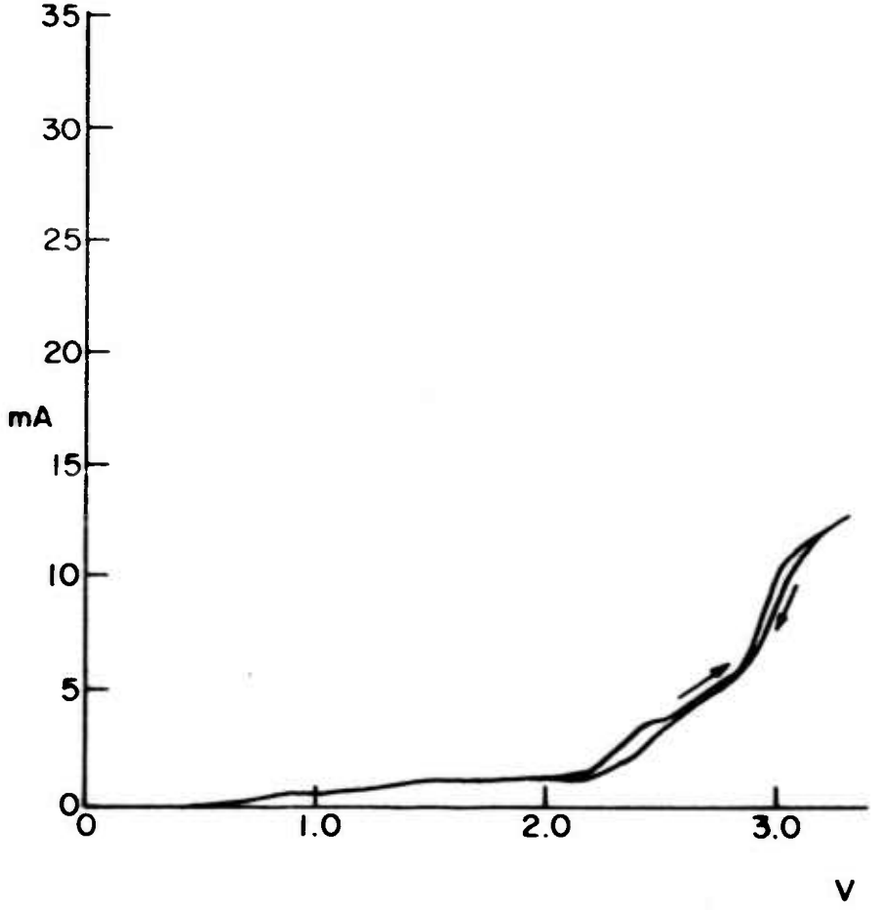

Figure 14.

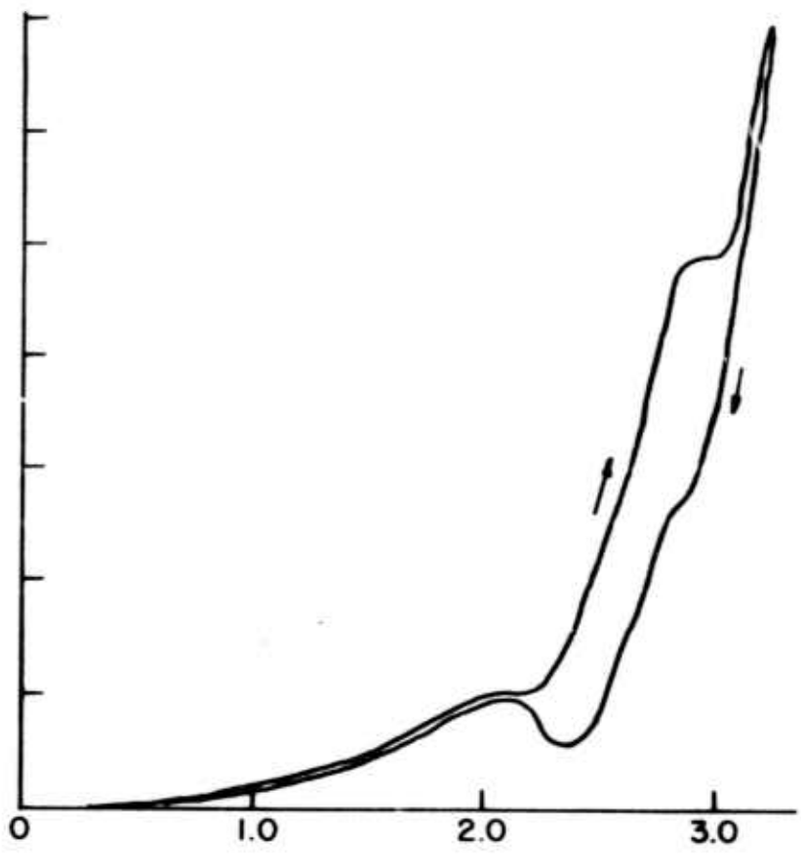

Figure 15.

Figure 14. Current vs Voltage, 1.0 mole % Sc_2O_3 in Flinak, 800°C.

Figure 15. Current vs Voltage, 5.0 mole % Sc_2O_3 in Flinak, 800°C.

decomposition potential of Sc_2O_3 the current due to the boron component would not greatly exceed the desired Sc:B ratio of 1:2.

The composition of the Flinak baths used are listed in Table 2. Cathode deposits containing clusters of black cubic crystals have been obtained from SB14 and SB16 (see Fig. 16). These samples are presently undergoing analysis.

At the time of this writing, analysis of electrodeposits from the oxide and Flinak baths is underway. It is clear that B and Sc have been codeposited, but a definite Sc-B compound has not yet been identified.

4. Conclusions and Future Plans

Routine production of 4 mm crystals of LaB_6 in a 300 hour period has shown that stable conditions for electrochemical crystal growth have been achieved. Seeded growth of the compound is being explored.

Electrochemical synthesis of ScB_2 is being pursued, the major current effort being analysis of deposits. It is clear that Sc and B are being codeposited, but a definite Sc-B compound has not yet been identified.

Phosphides and sulfides are of current interest to the semiconductor industry. Electrochemical synthesis of a number of phosphides has been reported in the literature, and production of single crystal or bulk samples of some of these materials would be a useful extension of present knowledge. Very little literature exists on the electrodeposition of sulfides or on any of the II-VI materials. FeS_x is currently an important material in battery research, and the II-VI materials including CdS are of general interest to the semiconductor industry. Electrodeposition of sulfides and/or phosphides would therefore be a useful area for future study, and some preliminary studies will be initiated shortly.

TABLE 2

Composition of Flinak Baths Used in Sc-B Program

	SB14		SB15		SB16	
		mole %		mole %		mole %
bath composition	Sc_2O_3	5.0	Sc_2O_3	5.0	Sc_2O_3	5.0
	B_2O_3	1.0	B_2O_3	.25	B_2O_3	3.0
	LiF	43.8	LiF	44.2	LiF	42.9
	NaF	10.8	NaF	10.9	NaF	10.6
	KF	39.4	KF	39.7	KF	38.5
deposition temperature °C	760°		810°		810°	

Figure 16. Sample #SB14-1, 100X.

5. References

(1) A. Damjanovic, M. Paunovic, and J. O'M. Bockris, J. Electroanalytical Chem. 9, 93 (1965).

(2) G. Wranglen, Electrochem. Acta 2, 130 (1960).

(3) H. J. Pick, G. G. Storey, and T. B. Vaughan, Electrochim. Acta 2, 165 (1960).

(4) T. B. Vaughan and H. J. Pick, Electrochim. Acta 2, 179 (1960).

(5) H. Fischer, Electrochim. Acta 2, 50 (1960).

(6) H. Seiter, H. Fischer, and L. Albert, Electrochim. Acta 2, 97 (1960).

(7) D. Elwell, I. Zubeck, R. Feigelson, and R. Huggins, J. Crystal Growth, 29, 65 (1975).

(8) L. Andrieux, Ann. de. Chim. 12, 432 (1929).

C. Continuous Growth

R. DeMattei

1. Introduction

Since faradaic processes deposit material at a controlled rate, in principle a new method for growing crystals combining electrochemical crystallization and the Czochralski technique for crystal growth can be developed. The major thrust of the continuous growth phase of the electrochemical crystallization program over the past year has been directed toward the development of such a method and an understanding of the growth parameters of importance in the electrochemical Czochralski technique (ECT).

To facilitate the study of ECT, the growth of sodium tungsten bronze crystals (Na_xWO_3, $0.1 < X < 0.9$) from WO_3-Na_xWO_4 melts was chosen as a model system because large crystals can be easily grown by electrocrystallization and the electrochemical technique has been well characterized.[1-9] The cubic phase of Na_xWO_3 ($0.38 < X < 0.9$) can be synthesized at the cathode of an electrochemical cell in a melt whose composition can range from 58 m/o tungstic oxide (WO_3)-sodium tungstate (Na_2WO_4) [$Na_{.38}WO_3$] to 5 m/o WO_3-Na_2WO_4 [$Na_{.9}WO_3$] according to the reactions:

$$xe^- + \frac{x}{2}\,Na_2WO_4 + (1 - \frac{x}{2})\,WO_3 \rightleftharpoons Na_xWO_3 + \frac{x}{2}\,O^2 \qquad \text{cathode 1a)}$$

$$\frac{x}{2}\,O^{-2} \rightleftharpoons \frac{x}{4}\,O_2 + xe^- \qquad \text{anode 1b)}$$

$$\frac{x}{2}\,Na_2WO_4 + (1 - \frac{x}{2})\,WO_3 \rightleftharpoons Na_xWO_3 + \frac{x}{4}\,O_2 \qquad \text{overall 1c)}$$

Such a system is ideal for investigating the growth parameters of this new technique.

2. Experimental Results

a. Initial Considerations

Since the sodium tungsten bronze is formed by reaction 1c, it is known[10] that a growing crystal can be remelted if it comes in

contact with free oxygen at elevated temperatures. An apparatus designed to pull Na_xWO_3 from a melt, therefore, must have provisions for keeping the as-grown bronze crystal out of contact with oxygen. A series of experiments to test the importance of the meltback problem and to devise a means to prevent it were undertaken.

It was shown that a bronze crystal exposed to air at 750°C quickly melted back. In a flowing helium atmosphere the bronze was stable as long as oxygen bubbles from the anode (reaction 1b) did not come in contact with it. The oxygen formed at the anode did, however, float across the surface of the melt to the cathode where oxidation took place. To avoid this problem, the anode was enclosed in a compartment which doubled as a helium outlet.

b. Apparatus

An apparatus for ECT has been designed and constructed, Fig. 1. Pulling is accomplished using a commercial crystal puller. This unit may be operated over a pull rate range of 0.1 to 20 mm/hr. Seed rotation in the range 0 to 80 rpm is provided by a motor with feedback for speed regulation. The crucible containing the melt is held in a quartz tube sealed by a watercooled brass flange. The flange is provided with fittings for the introduction of both an inert gas atmosphere and the three electrodes, including (1) the seed rod (which doubles as the cathode on which growth takes place), (2) the compartmented anode, and (3) a reference electrode for overpotential measurements. The quartz tube fits inside a resistance furnace whose temperature is controlled by a three function proportional controller which senses the temperature of the outer wall of the quartz tube by means of a chromel-alumel thermocouple. The axial gradient near the melt surface is 13.5°C/cm in the present experiments and the radial gradient is 10°C/cm.

The applied potential for electrodeposition is provided by a power supply which may be operated in either a constant voltage or a constant current mode. Contact to the rotating cathode is made by dipping a copper cup attached to the cathode rod into a pool of mercury.

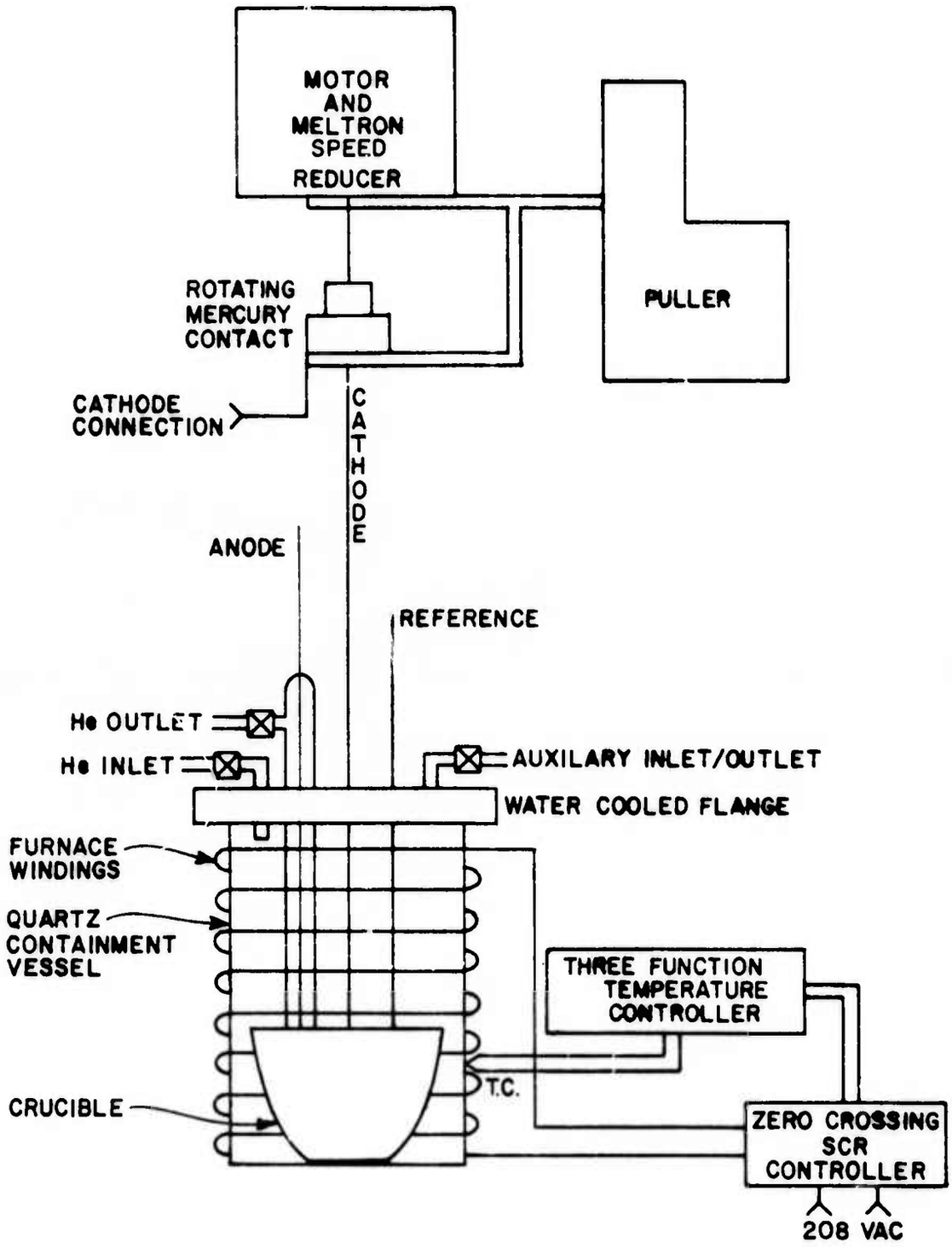

Figure 1. Diagram of the pulling-rotating mechanism and the furnace and controller of the ECT apparatus. 103a

Measurements of both overpotential and applied cell potential are made with a differential voltmeter and the cell current is monitored with a clip-on ammeter. These parameters are recorded and monitored continuously. See Fig. 2.

c. Initial Pulling Experiments

The initial series of experiments was designed to demonstrate that ECT would work and to give information on which to base further experiments. These first experiments were performed with seeds oriented along the [111] and in melts containing 25 m/o WO_3 - 75 m/o Na_2WO_4. The crystals grown in these experiments showed a three-fold axial symmetry consistent with [111] orientation in a cubic system. The sides of these crystals were convex. Unlike normal Czochralski growth, the interface region exhibited facetting with well developed {100} planes. (Fig. 3). These results are very similar to those observed by Perry[11] for the top-seeded growth of $(Ba,Pb)TiO_3$ pulled from a borate melt.

The bronze crystals also exhibited a constant cross section when grown in a stable manner. In some cases the crystals showed a marked curvature which was traced to seed misorientation.

d. Diameter Control

One of the difficulties of normal Czochralski growth is the control of the diameter of the growing crystal. The approach to diameter control usually taken in normal Czochralski growth involves the sensing of the diameter and the feedback of this information to control temperature or pull rate. Since electrochemical crystallization is an isothermal process depending only on faradaic processes for crystal growth, the diameter of the growing crystal should be controllable by variations in pull rate and total current in combination and without the need of sensing or feedback. The results of the initial experiments support this assumption. An application of Faraday's law gives a theoretical basis for establishing automatic diameter control in ECT.

The weight (W) of any material deposited electrochemically is given by

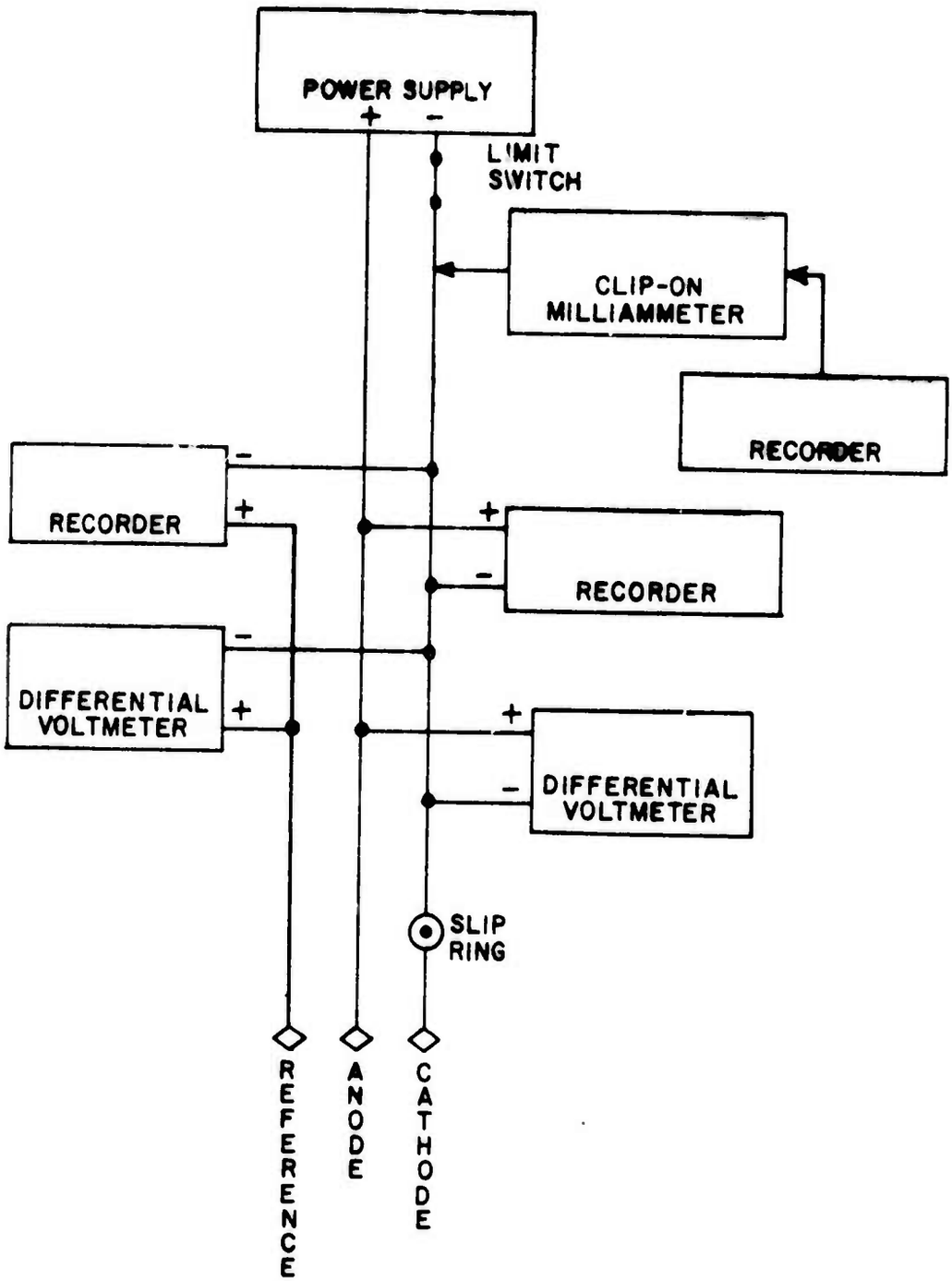

Figure 2. Block diagram of Electronics for the ECT apparatus.

Figure 3. Top left: Typical cross section of ECT grown crystal.
Top right: Typical interface of ECT grown crystal.
Bottom: Typical ECT grown crystal.
All crystals were grown along [111].

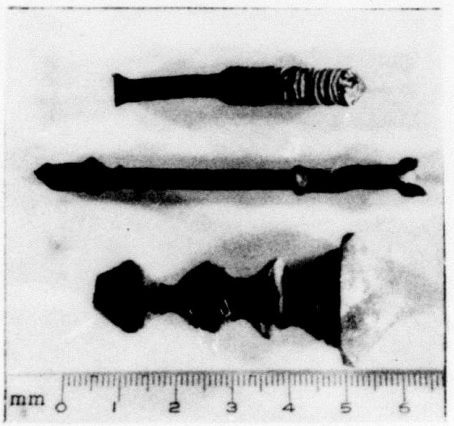

Figure 4. ECT grown crystals ([111]) with various current-pull rate combinations.

Top: Constant pull rate with current doubled after initial growth period.

Middle: Current and pull rate varied to maintain constant cross section. Branching due to exceeding maximum stable pull rate.

Bottom: Constant pull rate with constantly varying current.

$$W = \frac{M\varepsilon}{nF} Q \tag{2}$$

where M is the molecular weight of the material, Q the total charge transferred in coulombs, ε the efficiency of deposition, n the number of electrons transferred per unit of material deposited and F is Faraday's constant. The volume of material is

$$V = \frac{W}{\rho} = \frac{M\varepsilon}{nF\rho} Q \tag{3}$$

where ρ is the density of the material. The change of volume with time is given by

$$\frac{dV}{dt} = \frac{M\varepsilon}{nF\rho} \frac{dQ}{dt} = \frac{M\varepsilon}{nF\rho} I \tag{4}$$

where I is the total current. V may also be written

$$V = Ay \tag{5}$$

where A is an area and y a distance, and

$$\frac{dV}{dt} = y \frac{dA}{dt} + A \frac{dy}{dt} \tag{6}$$

But at equilibrium A is constant, thus

$$A \frac{dy}{dt} = \frac{M\varepsilon}{nF\rho} I \tag{7}$$

or

$$A = \frac{M\varepsilon}{nF\rho} \frac{I}{dy/dt} = \frac{KI}{dy/dt} \tag{8}$$

where dy/dt is the pull rate. For electrochemical growth A can be identified with the interface area and for a cubic material grown along the [111]

$$A = 0.75\ d^2$$

where d is the distance across one of the crystal sides. Thus,

$$d = \left(\frac{KI}{0.75} \frac{I}{dy/dt} \right)^{1/2} \tag{9}$$

and it should be possible to pull a crystal with a constant d or to vary d in a controlled manner by varying I and/or dy/dt. Figure 4 and Table 1 show the results of applying equation (9) to crystals grown in the [111]. For this orientation at least, diameter control is possible with ECT.

e. Rotation Experiments

Since stirring or seed rotation has been shown to have beneficial effects on normal crystal growth,[12,13,14] a series of experiments were designed to test the effect of seed rotation in the ECT. In particular, the effect of rotation on maximum stable pull rate was studied. At a given rotation rate, the pull rate was increased in steps of 0.25 mm/hr and the current was increased to maintain a constant diameter. This process was continued until the growth became unstable. The nature of the instability during growth along the [111] took two forms depending on the rotation rate: at or below 32 rpm the crystal would branch in the <110>, at or about 48 rpm, the normally convex sides of the growing crystal became concave and the absolute maximum pull rate (without branching) increased more than 3 fold. There was also evidence that the growth layers which normally in electrochemical crystallization nucleate at the edge of the crystal and propagate across the interface, did not propagate all the way to the face centers. This indicates that a low concentration of nutrient is present in this region. The experimental results are shown in Figure 5.

The limiting current density to a rotating electrode (i_{lim}) which is related to the maximum stable pull rate can be predicted by Levich's equation[15]

$$i_{lim} = 0.62\ nFD^{2/3}\ \nu^{-1/6}\ \omega^{1/2}\ C \qquad (10)$$

where D is the diffusion constant, ν the viscosity, ω the rotation in rpm and C the concentration. This equation was developed for a smooth interface. The crystals grown by ECT along the [111] have facetted interfaces (trigonal pyramids). The flow past the sharp edges of such

Table 1. Predicted distance across crystal (d) compared to experimental values.

Conditions	Calculated (ε = 0.925)	Experimental
I = 7.5 ma dy/dt = 1 mm/hr	3.84 mm	3.86 ± 0.12 mm
I = 15 ma dy/dt = 2 mm/hr	3.84 mm	4.20 ± 0.51 mm
I = 22.5 ma dy/dt = 3 mm/hr	3.84 mm	3.67 ± 0.15 mm
I = 15 ma dy/dt = 1 mm/hr	5.44 mm	6.0 ± 0.2 mm
I = 20 ma dy/dt = 1 mm/hr	6.29 mm	6.1 ± 0.2 mm
I = 30 ma dy/dt = 0.65 mm/hr	9.55 mm	9.17 ± 0.2 mm

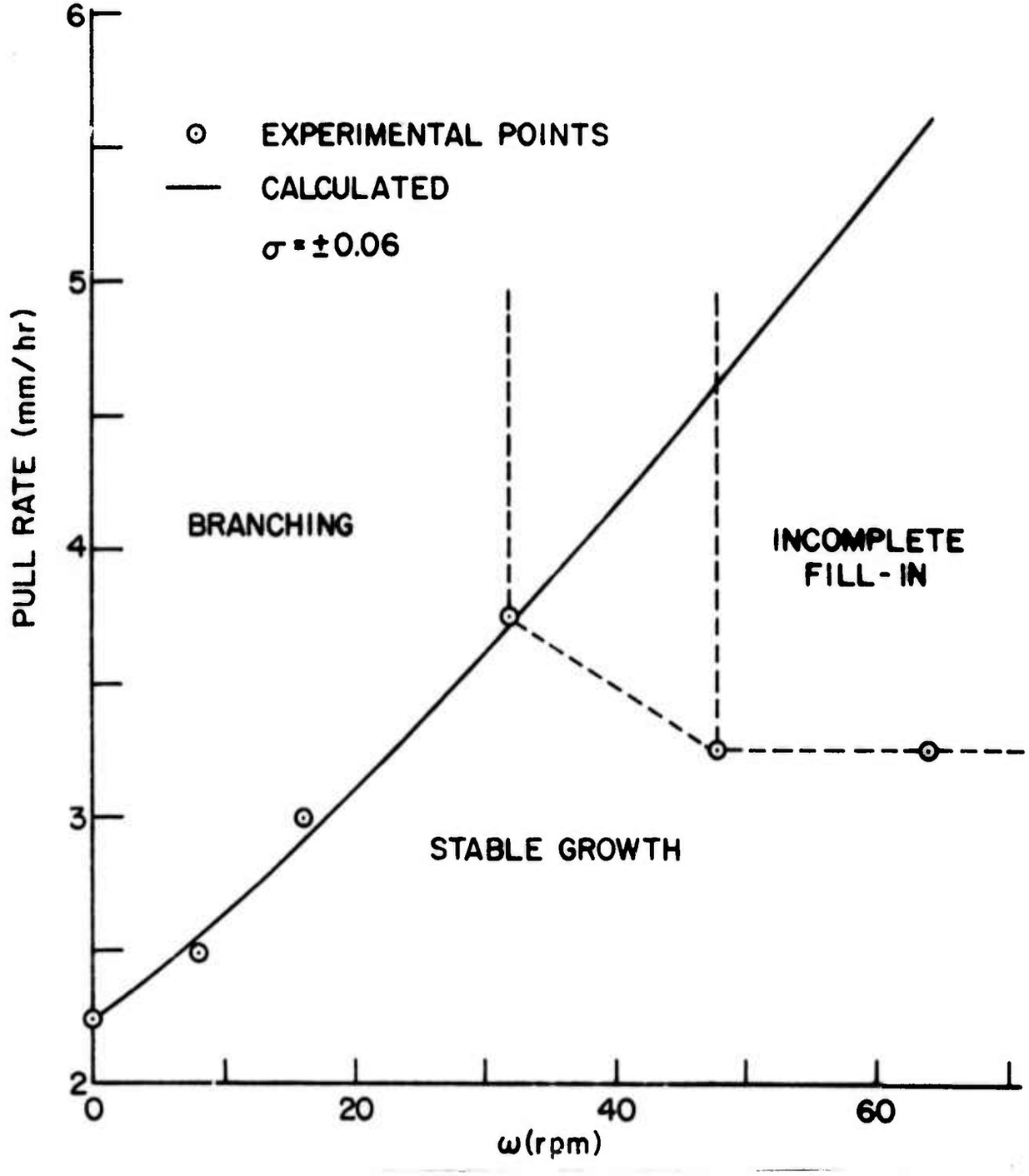

Figure 5. Maximum stable pull rate versus rotation rate.

an interface could induce eddies. If this is the case, then D is no longer constant, but is proportional to V the stream velocity which is related to ω. Thus equation (10) may be rewritten

$$i_{lim} = K\,\omega^{1.17}$$

or in terms of pull rate

$$dy/dt = 2.25 + K'\,\omega^{1.17} \qquad (11)$$

The solid curve in Figure 5 was calculated by a least squares fit of equation (11) to the data.

The behavior above 48 rpm may be caused by flow separation from the apexes of the interface at higher stream velocities (higher rotation) with the result that a non-mixing, depleted zone forms in the center of the growing facets. The behavior of this system is being modeled in a water-glycerin system.

The ultimate breakdown in either case may be explained by Chernov's interface stability model[16] in which stability is determined by the anisotropy of the kinetic coefficient [b(p)]. This coefficient is defined by

$$b(p) = \beta_{sT}\,|p|\,(1 + p^2)^{1/2}$$

where β_{sT} is a kinetic coefficient related to the step velocity parallel to the interface plane and p is the local slope. This local slope is determined by that angle (θ) between the interface plane and the face of a vicinal hillock (i.e. $p = \tan\theta$). The kinetic coefficient [b(p)] increases until either the local slope becomes 1($\theta = 45°$) (angles greater than 45° would, in this treatment, be referred to other interface planes, thus giving angles of less than 45° [$p < 1$]) or the rate of material uptake becomes greater than the supply and the layers can no longer propagate. In the region below 32 rpm the first case pertains and branching occurs when the rate of generation of new layers and their rate of propagation is such that b(p) is forced to its maximum (the [110] branch occurs at 45° to the (100)

facets). In the region above 48 rpm, nutrient concentration is low in the face centers and the increased growth rate is suppressed.

f. Seed Orientation

In the experiments previously described [111] oriented seeds were used exclusively with only one exception. In this one experiment a [112] oriented seed was utilized, and with the growth parameters employed, the crystal still grew along the [111]. Based on the results of the diameter control experiments with [111] oriented seeds, it was hoped that by proper adjustment of the growth parameters (current and pull rate) boules of constant cross section could be grown along the other major directions ([100] and [110]). In all cases the crystals widen uncontrollably as they grow and eventually lose contact with the melt. See Fig. 6 and Fig. 7.

Of the three growth directions studied, the [111] is unique in that its interface is made up of (100) facets oriented so that they bound each other on two sides, thereby limiting the growth at the edges thus formed. Along the [110] and [100] there is an absence of such boundaries. This situation allows the unbounded edges to grow out and, thereby, increase the interface area. Referring back to the development of equation (7), the situation during growth along the [100] and [110] is such that

$$dA/dt \neq 0$$

and

$$y \frac{dA}{dt} + A\, dy/dt = \frac{M\varepsilon}{nF\rho} 1$$

so that with both the pull rate and current fixed, the area continues to increase. As the area increases with a fixed flux of material for growth, the linear growth rate in the y direction eventually becomes less than the pull rate and the crystal loses contact with the melt. This can be prevented by constraining the growth within a ring or by using an edge-defined, film-fed growth (EFG) technique.

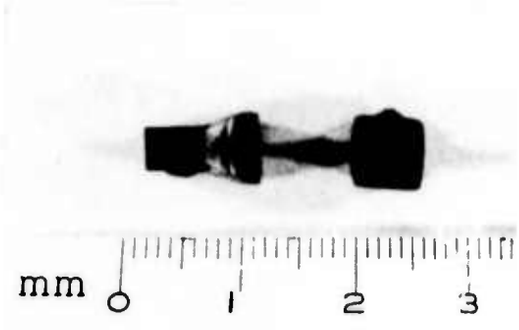

Figure 6. ECT grown crystal with [100] orientation.

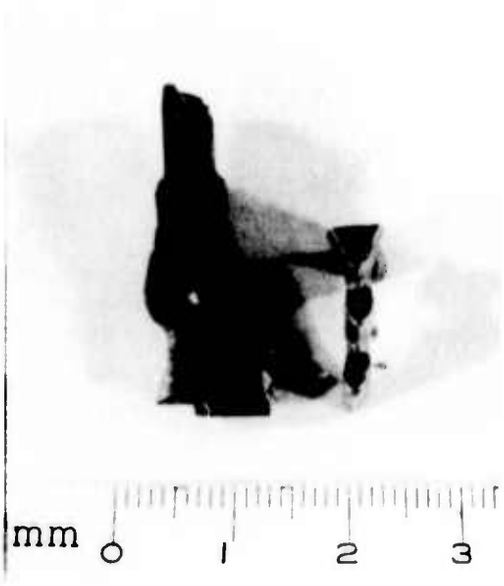

Figure 7. ECT grown crystal with [110] orientation.

g. Temperature Effects

Randin[9] has investigated the effect of temperature on the efficiency of Na_xWO_3 deposition (weight or deposit/theoretical weight from Faraday's law). Figure 8 shows his data replotted to show the temperature effect explicitly. The data which does not readily fit an analytical model, shows a definite trend toward decreased efficiency with increasing temperature. This is caused by the temperature induced disproportionation reaction[9]

$$6Na_xWO_3 \rightleftarrows x\,W + 3xNa_2WO_4 + (6 - 4x)\,WO_3$$

which follows deposition if the crystal remains in the melt.

To test the effect of temperature on ECT, a series of [111] oriented crystals were grown with large and small temperature perturbations of varying durations.

Small perturbations in temperature (± 10°C) have no visible effect on crystals growing at 750°C. Larger changes (+ 50°C) cause a visible decrease in deposition rate and grey, powdery tungsten deposits are observed. If the crystal is allowed to grow at elevated temperature for long periods of time (over 3 hours), the growth at the elevated temperature is quite porous and subsequent growth at lower temperatures is not necessarily oriented with respect to the original seed orientation. Shorter periods (< 2 hours) at elevated temperatures followed by a return to 750°C produces notches in the crystal, but subsequent growth is still oriented. This essentially confirms the results of Randin. It also implies that temperature can be used to control diameter through its influence on the cathode efficiency (ε), but this approach is much less desirable than the approach previously outlined.

The effect of temperature on the applied cell potential at constant current was studied concurrently with the above morphological investigation. The total applied potential (AP) ($I > 0$) is the sum of four separate potentials within the cell: (1) the decomposition potential (E_d) which is that potential below which deposition does not occur, (2) the resistive potential drop across the bath (IR

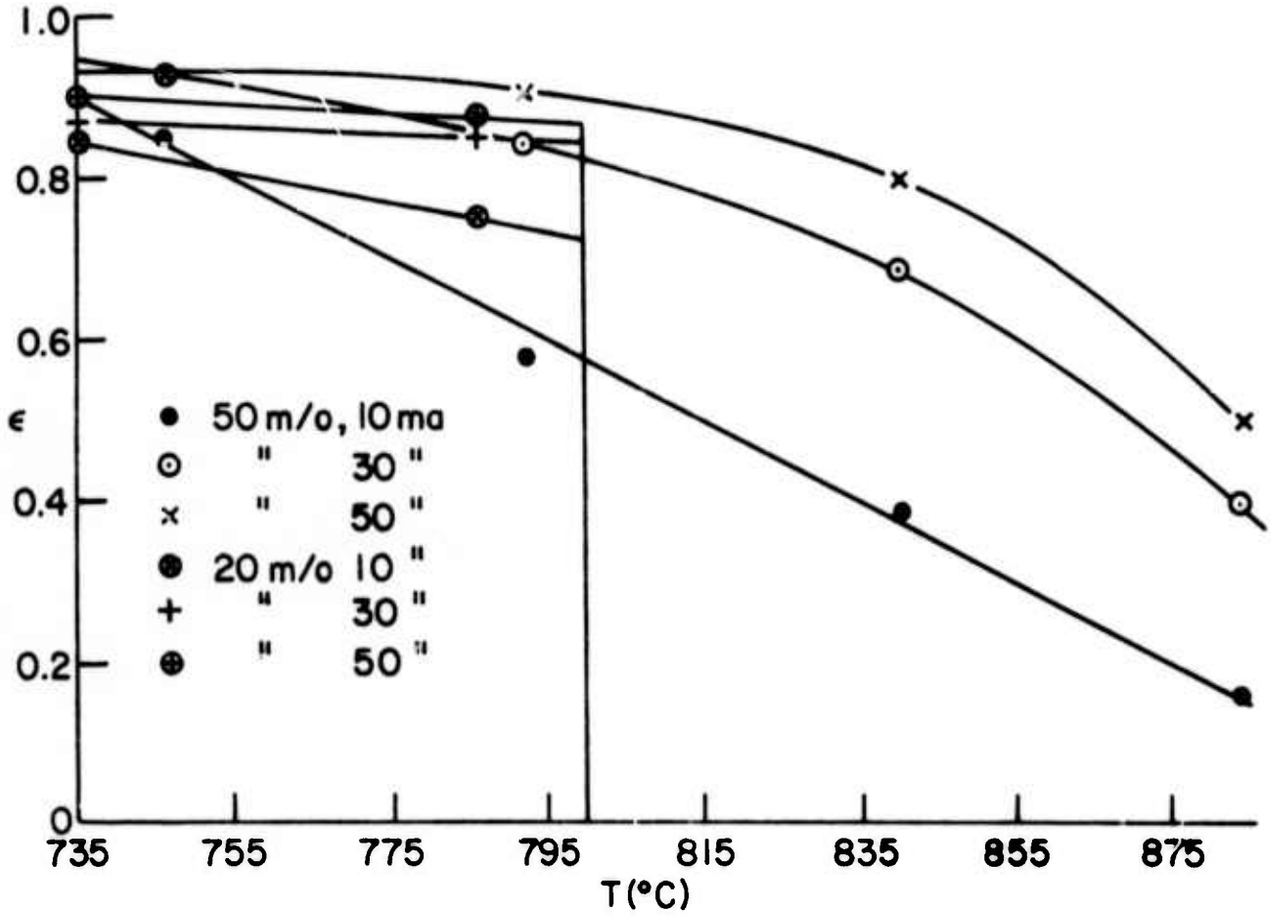

Figure 8. Cathode efficiency (ε) versus temperature.
(after Randin)

where R is the bath resistance), (3) the cathodic overpotential (η_C), and (4) the anodic overpotential (η_A)

$$AP = E_d + IR + \eta_C + \eta_A \tag{12}$$

The partial derivative of equation (12) with respect to temperature gives an estimate of the temperature effect

$$\frac{\partial(AP)}{\partial T} = \frac{\partial E_d}{\partial T} + \frac{\partial(IR)}{\partial T} + \frac{\partial \eta_C}{\partial T} + \frac{\partial \eta_A}{\partial T} \tag{13}$$

It remains to evaluate the terms on the right hand side of equation (13).

E_d is the Nernst potential

$$E_d = E^\circ - \frac{RT}{nF} \ln \frac{\text{Products}}{\text{Reactants}}$$

where R is the gas constant and Products refers to the product of the activities of the reaction products raised to the power of the stoichiometry number and Reactants is the same type of expression for the reactants. The partial of E_d with respect to temperature is

$$\frac{\partial E_d}{\partial T} = -\frac{R}{nF} \ln \frac{\text{Products}}{\text{Reactants}} = \frac{R}{xF} \ln \frac{[Na_xWO_3]\ [O_2]^{x/4}}{[Na_2WO_4]^{x/2}\ [WO_3]^{(1 - \frac{x}{2})}}$$

which has a value of 0.187 mv/°C for a 25 m/o WO_3-75 m/o Na_2WO_4 melt ($x = 0.82$).

Since the experiments are run with a constant current,

$$\frac{\partial(IR)}{\partial T} = I \frac{\partial R}{\partial T}$$

The change of R with temperature can be estimated using the conductivity data of Morris and Robinson[1] and estimating the cell constant from an independent experiment. The values IR versus T calculated from the data of Morris and Robinson are plotted in Figure 9. Using

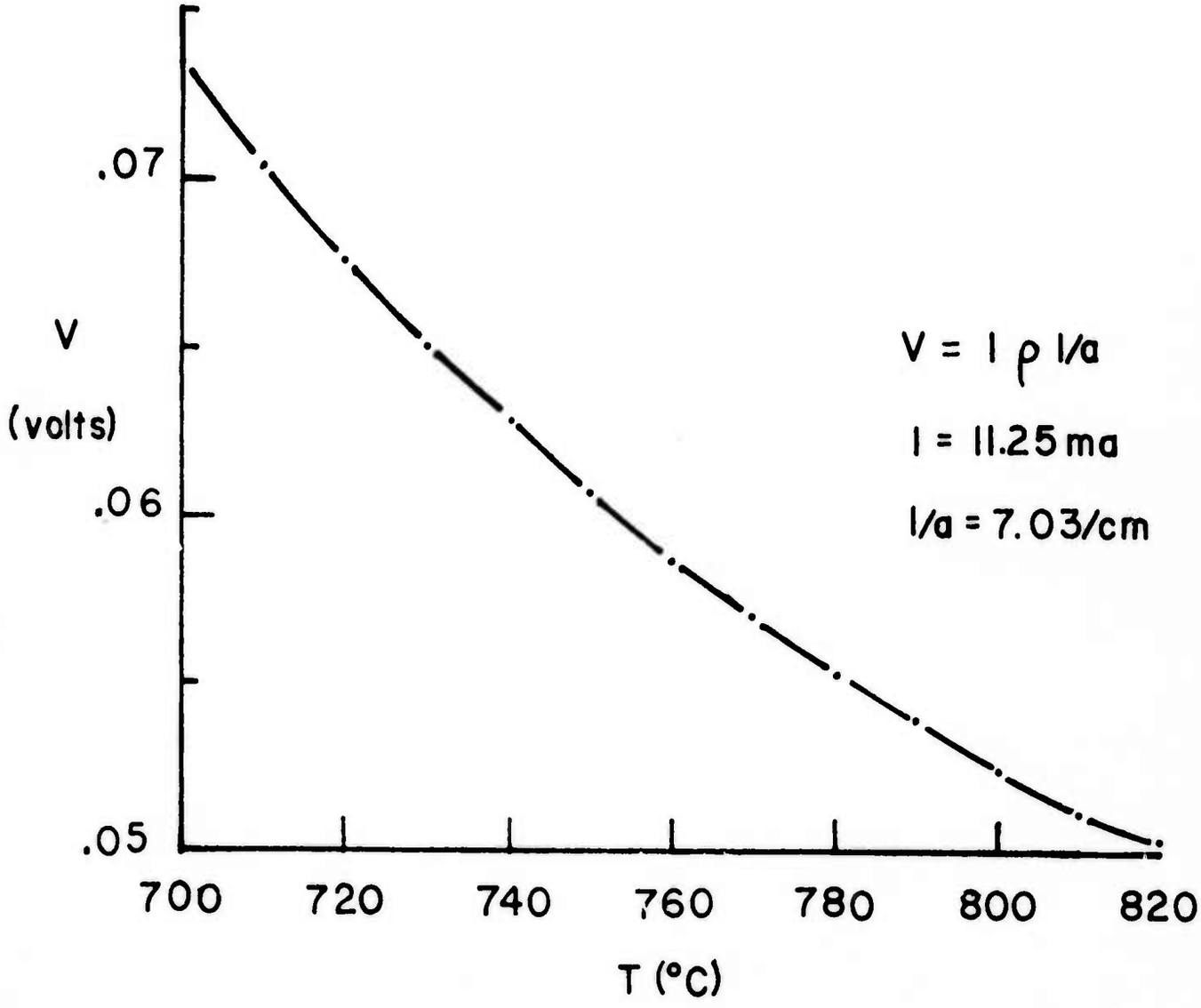

Figure 9. IR versus temperature for 25 m/o WO_3 - Na_2WO_4.

a linear approximation over a 30°C temperature range in the temperature region of interest (~ 750°C), the value of $\partial(IR)/\partial T$ is calculated to be -0.19 mv/°C.

Values for overpotential can be calculated from[17]

$$\eta = \frac{i}{i_o}\frac{RT}{nF} + \frac{i\,\delta\,RT}{DC_o n^2 F^2}$$

where i is the current density (ma/cm^2), i_o the exchange current density (i at $\eta = 0$), δ the boundary layer thickness, C_o the bulk concentration, and R, T, n, F, and D are as before, Thus

$$\frac{\partial\eta}{\partial T} = \frac{i}{i_o}\frac{R}{nF} + \frac{i\,\delta\,R}{DC_o N^2 F^2}$$

Using the exchange current density taken from Tafel plots of data gathered in this laboratory, $\partial\eta C/\partial T$ is calculated to be -0.4 mv/deg. The value for $\partial\eta_A/\partial T$ is not calculated since there are no values for i and i_o for the anode reaction, but the value is expected to be small.

The temperature experiments yield values for $\partial(AP)/\partial T$ and $\partial\eta C/\partial T$, combining these with the calculated values for $\partial E_d/dt$ and $\partial(IR)/dT$ result in

$$-0.269\ \frac{mv}{deg} = -0.253\ \frac{mv}{deg} + \frac{\partial\eta_A}{\partial T}$$

A comparison of the calculated values and the experimental values is shown in Table 2. Thus, it is possible to make an order of magnitude estimate of the effect of temperature on electrochemical parameters.

3. Comparison of the Normal Czochralski Technique (NCT) with the Electro-Czochralski Technique (ECT)

Normal Czochralski growth is a thermally controlled technique. Material is deposited at the interface as the result of maintaining

Table 2. Comparison of calculated and experimental values of temperature derivities of electrochemical parameters.

Parameter	Calculated	Experimental
$\partial E_d/\partial T$	.187 mv/deg	
$\partial(IR)/\partial T$	-.19 mv/deg	
$\partial \eta_C/\partial T$	-.4 mv/deg	-.250 mv/deg
$\partial \eta_A/\partial T$		
$\partial(AP)/\partial T$	-.403 mv/deg	-.269 mv/deg

it at or below the solidification temperature of the material. In order to sustain the growth of a crystal very careful control of the heat flow within the system must be maintained. The final shape of the crystal is to a large extent controlled by the temperature gradients in the melt. Diameter control in the normal Czochralski system is usually achieved by using some method of diameter sensing (weighing crucible, crystal or both, TV imaging, X-ray sensing, thermal profiling, etc.) which in turn is used to activate a preprogrammed feedback network which controls the temperature or pull rate in the system and thus the diameter. In principle, by proper manipulations of the temperature gradients, crystals can be grown in any orientation.

Electrochemical Czochralski growth is a faridaic process. Material is deposited at the interface due to the passage of current. Because of this, the system is relatively insensitive to thermal fluctuations and only slight attention need be paid to the heat flows within the system. Without the constraint of the freezing isotherm present in NCT, the ECT grown crystal is free to assume a shape dictated by crystal morphology. In theory automatic diameter control is inherent with ECT when operating in the constant current mode. But it was found with Na_xWO_3 that automatic diameter control could be achieved only when growing in the [111] since only in this orientation is the growth interface completely bounded by (100) facets. In order to achieve diameter control in other orientations a mechanical constraint must be used which is more easily accomplished with ECT since the thermal constrainst can be largely ignored. Growth in orientations close to the preferred growth direction (e.g. on the [112] in Na_xWO_3) is difficult with ECT since there are no gradients forcing the crystal to grow on axis.

The Electrochemical Czochralski technique will allow the growth of large crystals of electrically conducting materials with constant cross section and which can not be grown by NCT due to high melting point, thermal decomposition, or non-congruent melting systems. In these cases ECT can prove to be a very useful complement to NCT.

4. Future Plans

The past year's work has demonstrated that the Electrochemical Czochralski technique is viable. It should prove extremely useful when materials are needed in the form of rods, without the need of growing and sectioning a large crystal. Additional study is needed in the area of diameter control along the less favorable growth directions (e.g. the [100] and [110] in Na_xWO_3). The effect of compositional variation on the growth rate also needs to be investigated.

The development of an electrochemical, edge-defined, film-fed growth technique (EEFG) would employ much the same technology as ECT. This technique would have the potential of producing continuous lengths of complex shaped materials that would be extremely difficult to produce by other means.

Because of its ease of growth, the sodium tungsten bronze system can also be used in a future study of methods of effecting crystal perfection or of increasing growth rate while maintaining crystal quality. Among these would be deposition with an AC potential, rapid stirring, forced melt convection and deposition in an ultrasonic field. Such a program would be two pronged; one aimed at an understanding of the process, the other at equipment and technique development.

Another area of future interest is electrochemical epitaxial growth. Sodium tungsten bronze crystals could be used in such a program. They offer the advantage of being able to produce large substrates relatively quickly and the possibility of investigating heteroepitaxy with up to a 1.3% lattice mismatch within the bronze system itself.

5. References

(1) K. B. Morris and P. L. Robinson, J. Chem. Eng. Data. 9, 444 (1964).

(2) E. Banks and A. Wold, Prep. Inorg. React. 4, 237 (1968).

(3) P. G. Dickens and M. S. Whittingham, Quart. Rev. 22, 30 (1968).

(4) E. Banks, C. W. Fleischmann, and L. Meites, J. Solid State Chem. 1, 372 (1970).

(5) C. T. Hauck, A. Wold, and E. Banks, Inorg. Synth. 153 (1970).

(6) R. A. Fredlein and A. Damjanovic, J. Solid State Chem. 4, 94 (1972).

(7) M. S. Whittingham and R. A. Huggins, NES Special Publication, 364, 51 (1972).

(8) H. R. Shanks, J. Crystl. Growth 13/14, VIII-4 (1972).

(9) J.-P. Randin, J. Electrochem. Soc. 120, 1325 (1973).

(10) R. A. Huggins, private communication

(11) F. W. Perry, Crystal Growth, ed. H. S. Feiser, Pergammon Press, (1967) p. 483.

(12) H. J. Scheel and D. Elwell, J. Electrochem. Soc. 120, 818 (1973).

(13) B. Cockayne, M. Chesswas, and D. B. Gassen, J. Mater. Sci. 5, 837 (1969).

(14) J. R. Carruthers and K. Nassau, J. Appl. Phys. 39, 5205 (1968).

(15) V. C. Levich, Physiocochemical Hydrodynamics, Prentice-Hall (1962) 700 pp.

(16) A. A. Chernov, J. Cryst. Growth 24/25, I-3 (1974).

(17) J. L. Barton and J. O'M. Bockris, Proc. Roy. Soc. 268, 485 (1966).